DESIGN AND DEVELOPMENT OF A NOVEL TOROIDAL PNEUMATIC MOTOR

by

Braden A. Murphy

Submitted in partial fulfilment of the requirements
for the degree of Master of Applied Science

at

Dalhousie University
Halifax, Nova Scotia
December 2012

DALHOUSIE UNIVERSITY

DEPARTMENT OF MECHANICAL ENGINEERING

The undersigned hereby certify that they have read and recommend to the Faculty of Graduate Studies for acceptance a thesis entitled “DESIGN AND DEVELOPMENT OF A NOVEL TOROIDAL PNEUMATIC MOTOR” by Braden A. Murphy in partial fulfilment of the requirements for the degree of Master of Applied Science.

Dated: December 4, 2012

Supervisor: _____

Readers: _____

_____

DALHOUSIE UNIVERSITY

DATE: December 4, 2012

AUTHOR: Braden A. Murphy

TITLE: Design and Development of a Novel Toroidal Pneumatic Motor

DEPARTMENT OR SCHOOL: Department of Mechanical Engineering

DEGREE: M.A.Sc CONVOCATION: May YEAR: 2013

_____

Signature of Author

DEDICATION PAGE

I dedicate this work to my parents. Their support and encouragement has allowed me to pursue my dreams with hard work and determination. This is for you.

Table of Contents

List of Tables

List of Figures

Abstract

A novel toroidal pneumatic motor (rotary actuator or rotary engine) has been developed and tested. The motor is designed with a ring torus (or revolved circular cross-section) working chamber, which is formed by two rotors and sections of a casing (or stator). The rotors are designed with an equal number of pistons, an arrangement of one-way bearings (to transfer torque from the rotors to a common drive shaft), and an impact mechanism to operably control the positioning of the rotors relative to ports located within the stationary casing. This design is aimed at improving the power density (power per unit mass), efficiency and torque output at low shaft speeds, when compared to conventional vane motors. Dynamometer test results are presented, showing the torque output of the motor with compressed air supply pressures of 10 to 80 psi at 10 psi increments.

List of Abbreviations Used

FEM	Finite Element Method
Dyno	Dynamometer
DAQ	Data Acquisition System
IC	Internal Combustion
RIICE	Rotational Impact Internal Combustion Engine
kW	Kilowatt
hp	Horse Power
K	Kelvin
CFM	Cubic feet per minute
SCFM	Standardized cubic feet per minute
L/s	Liters per second
m	Meters
STP	Standard Temperature and Pressure
N	Newton
kN	Kilo Newton
CNC	Computer Numerically Controlled
θ_{min}	Minimum angle between pistons in a toroidal motor
θ_{max}	Maximum angle between pistons in a toroidal motor
n_{noz}	Number of compressed air nozzles connected to the working chamber of a toroidal motor.
n_p	Number of pistons in a toroidal motor
R_{st}	Stator radius in a toroidal motor
R_p	Piston Radius in a toroidal motor

R_c	Radius from the center to the piston to the center of the drive shaft in a toroidal motor
RPM	Revolutions per Minute
V	Volume
α	Shaft angle of a vane motor
L	Length of the stator cylinder in a vane motor
R_s	Radius of the stator cylinder in a vane motor
R_r	Radius of the rotor in a vane motor
$\beta(\alpha)$	Stator angle as a function of the shaft angle in a vane motor
e	Eccentricity of the rotor relative to the stator in a vane motor
V_{cell}	Cell volume of a in a pneumatic motor
γ	Angle between vanes in a vane motor
ε	Expansion ratio in a pneumatic motor.
V_{cell}^{max}	Maximum volume of a cell in a pneumatic motor
V_{cell}^{fill}	Minimum volume of a sealed chamber in a pneumatic motor
V_{disp}	Displacement (volume) of a pneumatic motor

Acknowledgements

I would like to thank my love and best friend, Robynne, for her unconditional support and encouragement.

I would also like to thank: my supervisor, Dr. Darrel Doman, for his belief in me, and his dedication to this project; Erica Fraser, for her time and effort towards this project; and my supervisory committee, Dr. Daniel Boyd and Dr. Clifton Johnston for their diligence of reviewing this dissertation.

CHAPTER 1 INTRODUCTION

Pneumatic motors convert high pressure gas (usually air) to rotational mechanical work. These motors have a wide array of applications, and are used mainly because of their high power density, usability in hazardous environments, and no-risk of overheating by overloading (as occurs with electric motors). Some examples are heavy-duty hand tools for mechanics and construction workers and starter motors for large engines and compressors. The most common type of pneumatic motor is the rotary vane motor, and other types of motors include rotary piston, axial piston, turbine, and gear motors. The performance of vane motors is limited by the geometrical limitations of the rotors and vanes, and the friction generated by the vanes. The performance of piston motors is limited by their speed of operation (due to the acceleration of the pistons), and axial pistons are limited by the complexity and cost of the components and radial pistons are limited by the bulkiness of the motor. Turbine motors tend to be the most efficient, but have very low torque output and require heavy gear-reducers for usable shaft speeds. Pneumatic gear motors are not very common, and are the least efficient of all the available motors.

A novel rotary pneumatic motor has been developed to solve many of the problems seen in current motor designs. The motor is specifically referred to as a toroidal motor, which means that the working chamber is in the shape of a ring torus, which is generated by revolving a circular cross-section around a central axis. The motor design is compact, has high torque output, and inherently reduces friction caused by sliding seals. The purpose of this thesis is to demonstrate the design and development of this toroidal rotary pneumatic motor. In particular, a detailed review of toroidal engines and motors, design and analysis of critical components, an experimental test setup, and testing results are presented. Power and torque versus motor speed curves are the industry standard of classifying pneumatic motors, and the results presented in this thesis are the first, to the author's knowledge, power and torque curves published for a toroidal pneumatic motor or toroidal internal combustion (IC) engine.

In the context of this thesis, the primary difference between an engine and a motor is the complexity of the thermodynamic process occurring in the device. In particular, an IC engine uses potential chemical energy stored in a fuel, combusts the fuel inside a closed chamber, and the high temperature and pressure combustion gasses create mechanical work. Whereas, a pneumatic motor uses high pressure air to create mechanical work without any major thermodynamic variances, relative to that seen with internal combustion engines.

The novel toroidal motor design was originally developed for use as an internal combustion engine. However, through development, it was realized that the engine could be used as a pneumatic motor. As will be seen in the detailed review of toroidal motors and engines, these devices have been under development for almost 100 years. However, these designs have achieved very limited commercial success, partly due to the focus on internal combustion engines. Through the development of the novel toroidal motor design, it became clear that developing the concept as a pneumatic motor greatly reduced the quantity and complexity of design problems that needed to be solved. Furthermore, many of the design problems that needed to be solved for a pneumatic application are parallel with the problems that have been seen with an IC application. Therefore, the systems created and knowledge gained for the pneumatic motor from this thesis can be applied to an IC application in the future.

CHAPTER 2 APPLICATION OF PNEUMATIC MOTORS

Pneumatic motors are widely used in various industrial and domestic applications. Examples of applications are for uses in hand tools (1), starter motors for large industrial equipment (2), firefighting and auxiliary equipment for ships (3), and dental tools (4). These motors are also widely used in hazardous areas, where electric motors require electrical shielding for safe operation (5). There are two types of pneumatic motors: displacement motors and dynamic motors. The difference in the two types is the configuration of the working chamber, which is the volume enclosed within the motor that converts a high-pressure working fluid to mechanical work. In particular, the working chamber in a displacement motor has a variable volume, and the working chamber in a dynamic motor has a fixed volume (6). Common displacement motors are rotary vane and piston motors, and an example of a dynamic motor is a turbine. Figure 1 illustrates schematics of the most common types of pneumatic motors, and below is a description of each of the types of motors.

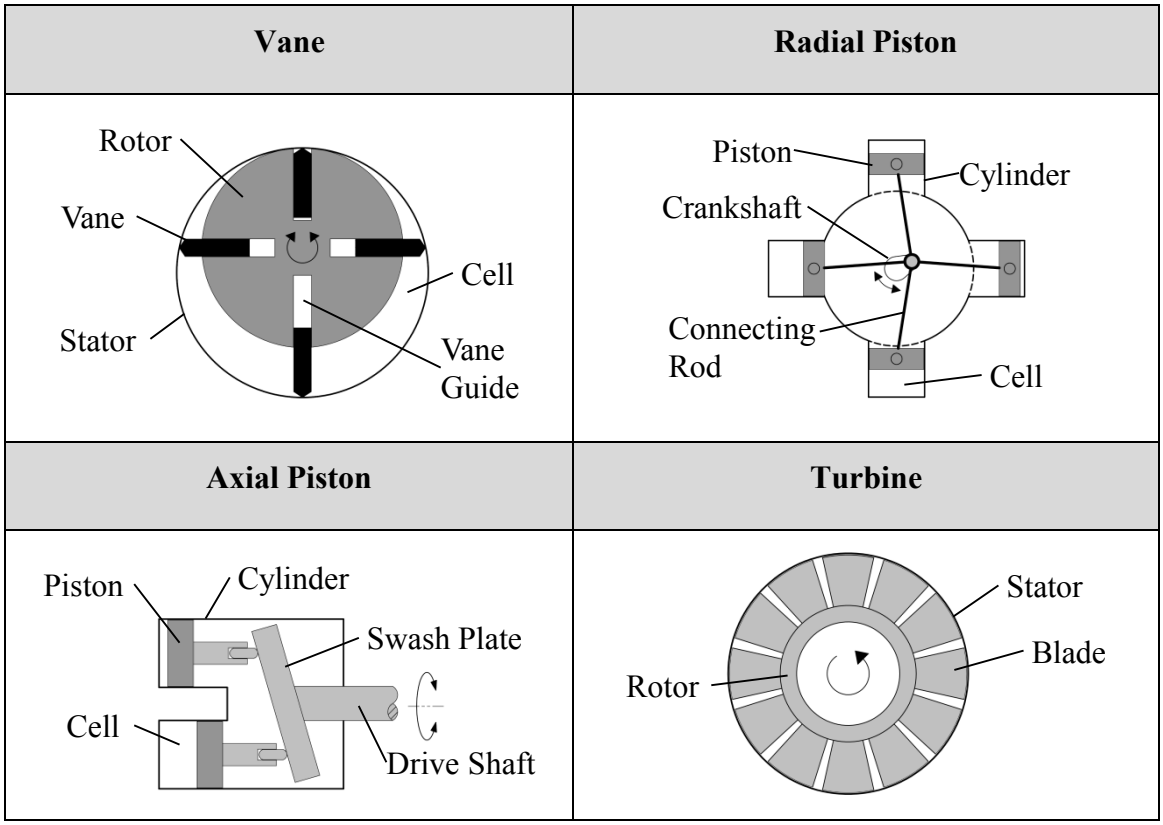

Figure 1 - Illustration of the primary mechanisms in common types of pneumatic motors.

Vane motors are constructed by housing a rotor eccentrically in a larger diameter stator. Vanes installed within slots (or vane guides) on the rotor maintain contact with the stator as the rotor rotates. A sealed cell is formed between each pair of vanes around the rotor, and ports installed around the stator allow each of the cells to be charged with a pressurized working fluid. The variance in the extended length of the vanes creates a differential in the force generated by the surrounding vanes of each cell, which generates a net torque on the rotor. The rotation of the rotor creates a varying cell volume, which expands the working fluid when the cell volume increases, and discharges the working fluid through ports in the stator when the cell volume decreases. The rotor is connected to an output shaft, and these motors can be operated bi-directionally by reversing the flow of the working fluid through the ports around the stator. This type of motor is discussed in more detail further in this chapter and detailed analysis can be found in Beater (7).

Radial piston motors are constructed by housing pistons within cylinders mounted radially (perpendicular) around a crankshaft. Sealed cells are formed between the pistons and the cylinders, and a valve system (not shown) controls the flow of a working fluid through ports in the cylinders. Each cell is intermittently charged with a pressurized working fluid, and a force is generated on the pistons. Connecting rods couple the pistons to the crankshaft at a point offset from the center of rotation of the crankshaft. Therefore, a force on the piston will generate a torque on the crankshaft. The rotation of the crankshaft causes the pistons to reciprocate and creates varying cell volumes, which expands the working fluid when each cell volume increases and discharges the working fluid when each cell volume decreases. The rotor shaft is connected to an output shaft, and the valve system is operated by the rotation of the shaft. These motors can operate in either direction by reversing the flow of the working fluid through the ports of the valve system. Literature on these types of motors specifically for pneumatic use is currently limited to manufactures publications, such as Apex Tool Group (8), and further information can be found in the aviation industry for radial piston internal combustion engines, as shown in Basshuysen and Schafer (9).

Axial piston motors are functionally similar to radial piston motors. The differentiation is the orientation of the pistons and cylinders with respect to the drive shaft, and as a result, the primary difference is the connecting mechanism between the pistons and the drive

shaft. Axial piston motors are constructed by housing pistons within cylinders mounted axially (parallel) around a drive shaft. A sealed cell is formed between the pistons and the cylinders, and a valve system (not shown) controls the flow of a working fluid through ports in the cylinders. Each cell is intermittently charged with a pressurized working fluid, and a force is generated on the pistons. The pistons are connected to an angled swash plate, and the angle of the plate generates a torque on the shaft from the force on the pistons. The rotation of the swash plate allows the pistons to reciprocate, and creates a varying volume in the cylinder chambers. These motors can operate in either direction by reversing the flow of the working fluid through the ports of the valve system. Similarly to radial piston motors, literature on these types of motors specifically for pneumatic applications is limited to manufactures publications, such as Apex Tool Group (8), and further literature for these motors can be specifically found in Akers *et al*. (10).

Turbine motors are constructed by housing a rotor with angled blades (or fins) mounted radially between the outer surface of the rotor and inner surface of the stator (or housing). A working fluid moves across the angled turbine blades and generates a pressure differential across the blades. This generates torque on the rotor, which is connected to an output shaft. Turbine motors are generally limited to operate only in one direction, and more detailed analysis of these motors can be found in Beater (11) and detailed analysis and theory of turbines can be found in Dixon (12).

2.1 General Performance of Pneumatic Motors

Generally, pneumatic motors are used because they have very high power density, or power output per kilogram of engine mass, with power output ranging from 0.10 to 30 kW (0.13 to 40 hp) (6). Figure 2 demonstrates the power densities of a sample of various types of pneumatic motors currently available.

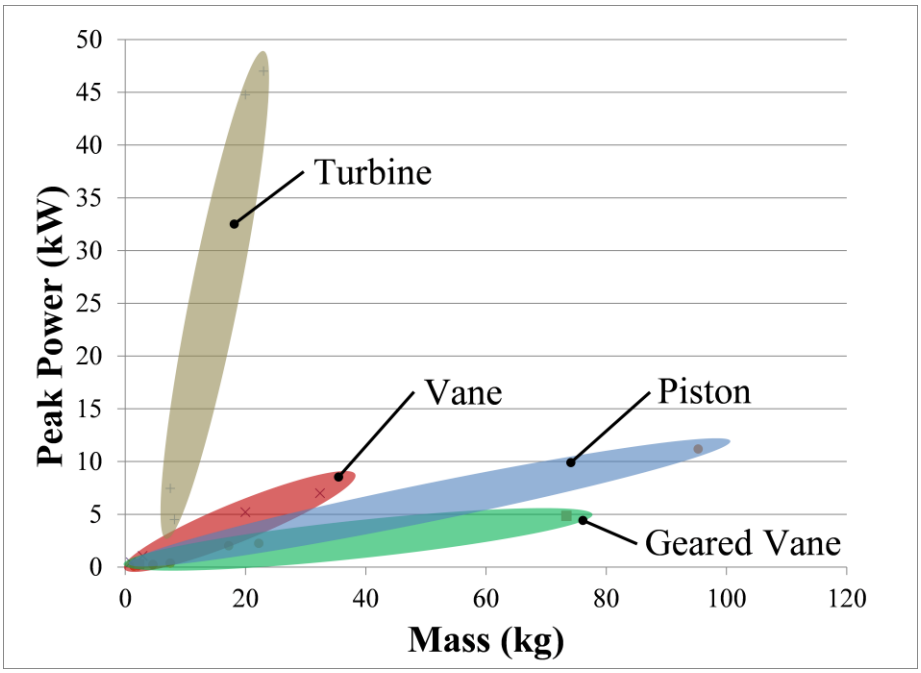

Figure 2 - Illustration of motor power output vs. motor mass of a selection of commercially available pneumatic motors. Refer to Appendix B for methodology and references of this figure.

It is seen that turbine motors have the largest range of power output and highest power density. These motors have very low torque output and achieve their high power output with high rotational speeds (over 10,000 rpm), and require heavy-duty gear reduces for applications with lower shaft speeds (under 10 000 rpm) (11). However, vane motors are the most common type of motor because of their simple design (6; 7; 13).

The air power, or rate of energy delivered to the motor, can be calculated based on the measured pressure and volumetric flow rate. For pneumatic applications, power can be calculated with the measured volumetric flow rate and pressure. The influence of temperature on the power calculation can be neglected. This is because temperature differential between the compressed air supply and the surrounding is negligible. Furthermore, when the temperature differential reaches 100 K, the temperature component of power is only 15% of the total, so when the temperature differential is 5 K to 10 K, the effect on the power calculation is negligible (14). Therefore, the power P can be calculated as seen in Eq. 1.

$$P = pQ \ln\left(\frac{p}{p_a}\right) \qquad \textit{Eq. 1 (14)}$$

Where P is power, p is measured pressure, p_a is atmospheric pressure, and Q is measured volumetric flow rate. Furthermore, for the calculation of power given the free air (or standardized) volumetric flow rate, Eq. 2 can be used, where Q_a is the standardized volumetric flow rate. The standardized volumetric flow rate is the equivalent volume of a compressed (or vacuum) gas at standard temperature and pressure (STP), and are usually given units of standardized cubic feet per minute (SCFM) or normalized (equivalent at STP) liters per second (L/s).

$$P = p_a Q_a \ln\left(\frac{p}{p_a}\right) \qquad \textit{Eq. 2 (14)}$$

The power output of the motors presented in Figure 2 is shown as a function of the air flow through the motor in Figure 3.

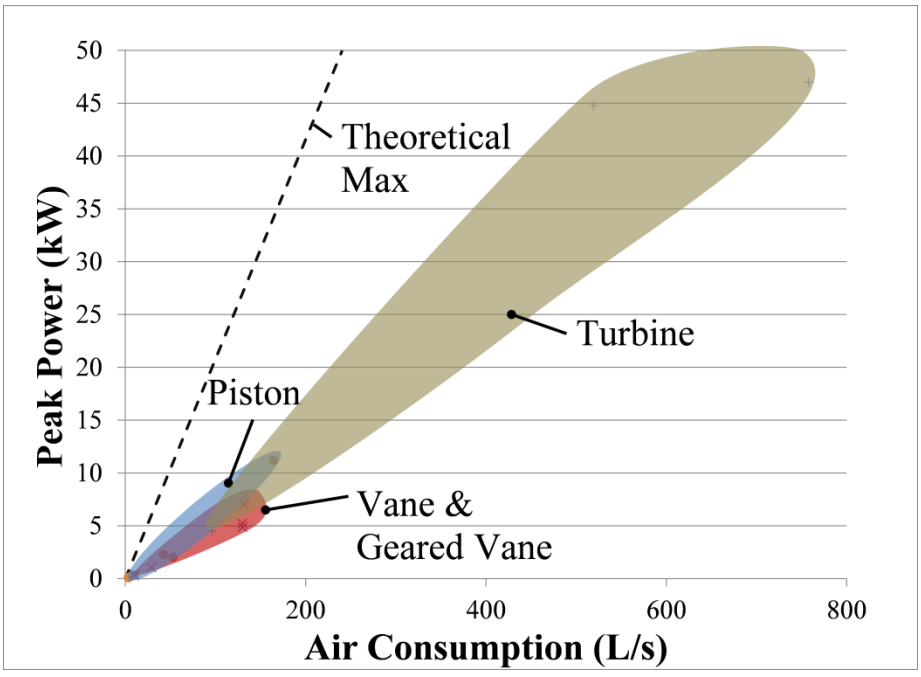

Figure 3 - Illustration of peak power vs air consumption for current pnumatic motors. Refer to Appendix B for methodology and references of this figure.

It is seen in Figure 3 that the piston and turbine motors achieve higher power output per air consumption. However, the differences are not as distinct as that seen with the power

densities, for the various types of motors. As described above, the power input into the motor can be calculated from the air consumption and supply pressure. Figure 4 illustrates the power output of the motors, as a function of the efficiency, which is calculated as the ratio of the peak output power of the motor to the input power of compressed air supplied to the motor.

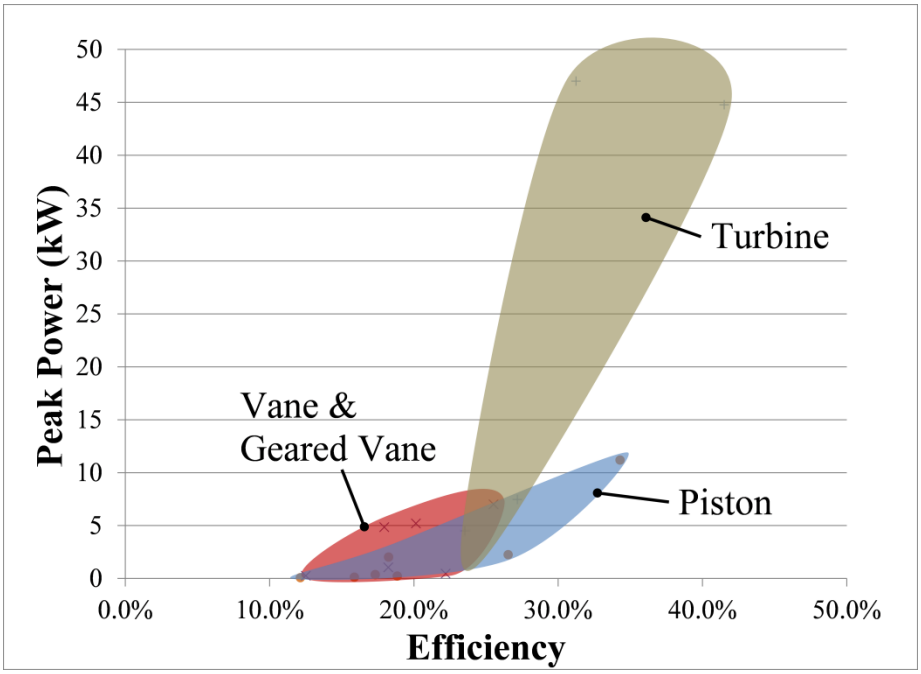

Figure 4 - Illustration of peak power vs efficiency for current pnumatic motors. Refer to Appendix B for methodology and references of this figure.

It is seen that vane motors are the least efficient, and piston and turbine motors can achieve the highest efficiencies. The corresponding efficiencies of the motors calculated from Figure 3 are within the range of 10% to 40%.

The power output characteristics of pneumatic motors are seen to be similar independent of the motor type. Figure 5 illustrates a schematic of the general performance characteristics of pneumatic motors.

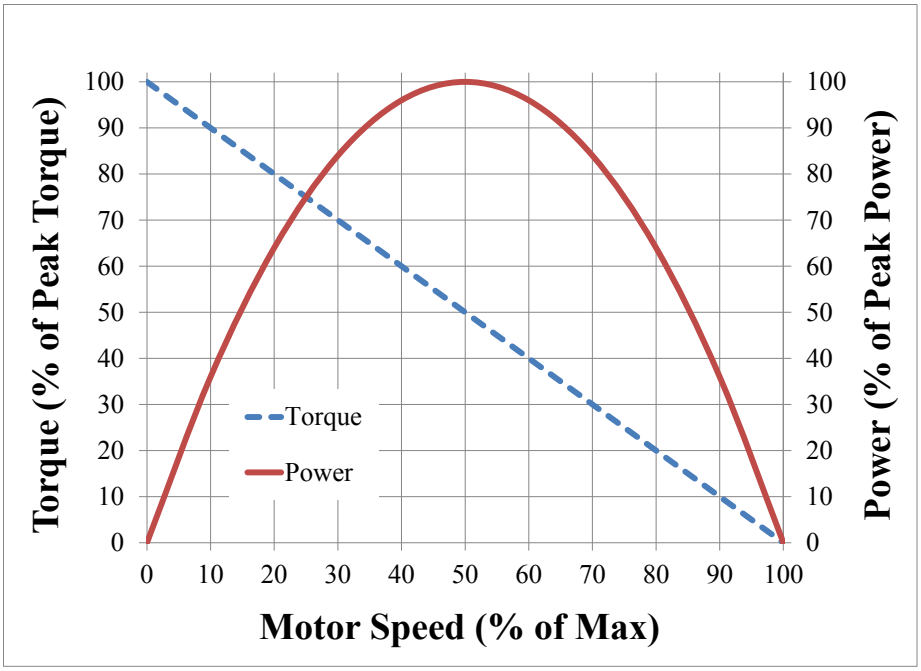

Figure 5 - Pneumatic motor general performance schematic (6; 11).

Generally, the torque output of the motor is highest at low speed, and decreases linearly as the motor speed increases, as shown in Figure 5. Further, the peak power generally occurs at 50% of the peak torque output. It has been found that these performance characteristics are due to a combination of the frictional forces and losses through the ports in the motor (15; 16; 17). Furthermore, the air consumption generally increases with motor speed, and the peak efficiency occurs around the peak power output. However, air flow of a vane motor is much less dependent on shaft speed, when compared to piston motors, because of high leakage at lower speeds with the vane motors (17).

2.2 Vane Motors

Pneumatic vane motors use a single rotor with fixed vanes to seal separate chambers (or cell volumes) of the motor (18). An example of this type of motor is illustrated in Figure 6, and a schematic of the main components is shown in in Figure 7.

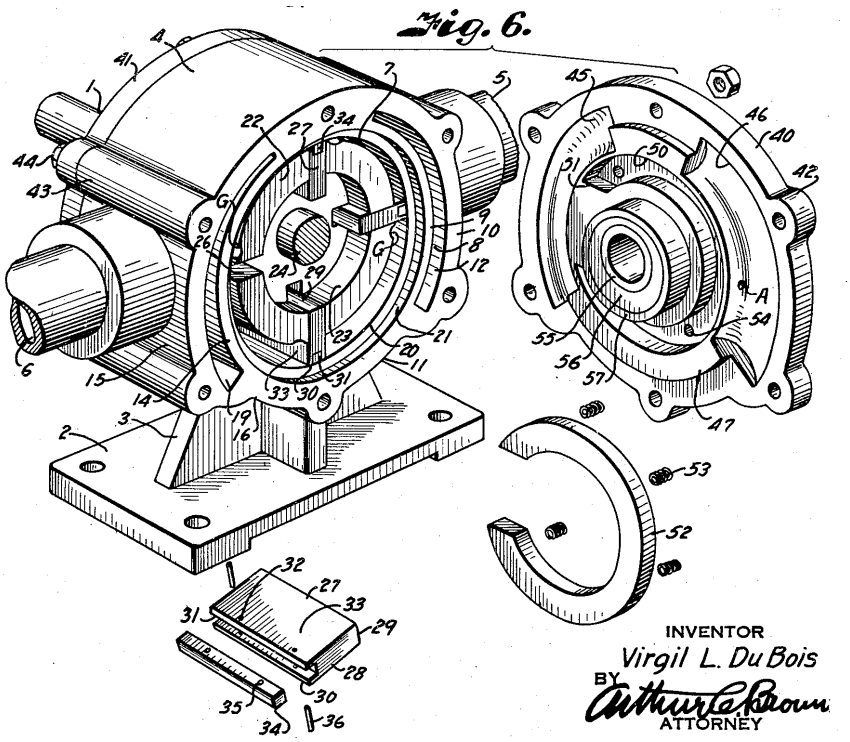

Figure 6 - Illustration of a vane motor with the end plate (40) removed, vane seals (27), stator (7), and rotor (22) (19).

The rotor is mounted eccentrically within a stator cylinder, and the vane seals are designed to maintain contact with the stator (housing) as the rotor rotates. This is achieved by either the inertial force of the vanes due to the rotational motion (and mass of the vane), or by pneumatic or spring forcing, depending on the configuration of the motor (20). As a result, the vane slides against the vane guide (sealing face of the rotor) as the vane moves between the most eccentric position and the least eccentric position. This sliding action creates a differential area between the vanes sealing each cell volume formed between the vanes of the motor (21). A pressurized working fluid creates forces on the vanes sealing each cell, and because of the differential area, a larger force acts on the most extended vane in each cell. Therefore, as each cell is charged with a pressurized working fluid through the inlet port, a torque is created on the rotor and the rotor rotates. As the rotor rotates, the volume of each cell expands to a maximum volume and then contracts and reduces in volume, as illustrated in Figure 10. Ports are located around the stator to allow the working fluid to exhaust while the cell volume is contracting, thus allowing the working fluid to expand between the inlet and outlet of the motor. This is

the mechanism that converts the energy stored in the compressed working fluid to rotational work.

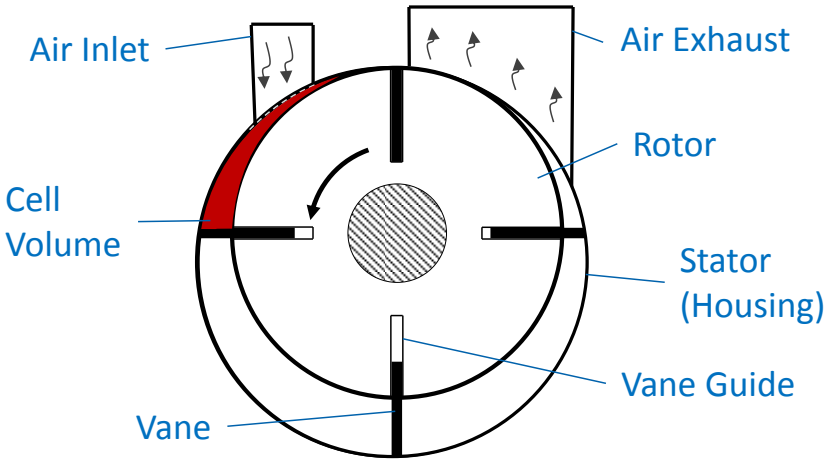

Figure 7 - Schematic of a vane motor outlining the main components and cell volume formed between vanes.

The advantages of the vane motor are in the simplicity of the design: with only a few moving parts, reversible operation, and cost-effective manufacturing, these motors have been proven widely effective in many applications (5). Significant work has led to optimizing the design of these motors for improved performance, which has been more recently focused on specific application improvements (16; 18; 20; 22). However, it is thought that there are limitations of the vane motor, which are inherent to the fundamental geometry and operation of the motor. Specifically, since each vane seals between two cells, the force acting on one side of the vanes positively affects the net torque output of the motor, while the force acting on the other side of the vane negatively affects the net torque output of the motor. Therefore, the net torque generated by any vane (neglecting friction) is the difference of the perpendicular forces (relative to the center of the rotor) acting on the vane, multiplied by the distance of the forces from the center of the rotor (22). Or in other words, the net torque produced by each cell is the difference of the torques created by the sealing vanes of the cell. This is illustrated in Figure 8, where the net force acting on the leading face creates a positive torque, and the net force acting on the trailing faces creates a negative torque.

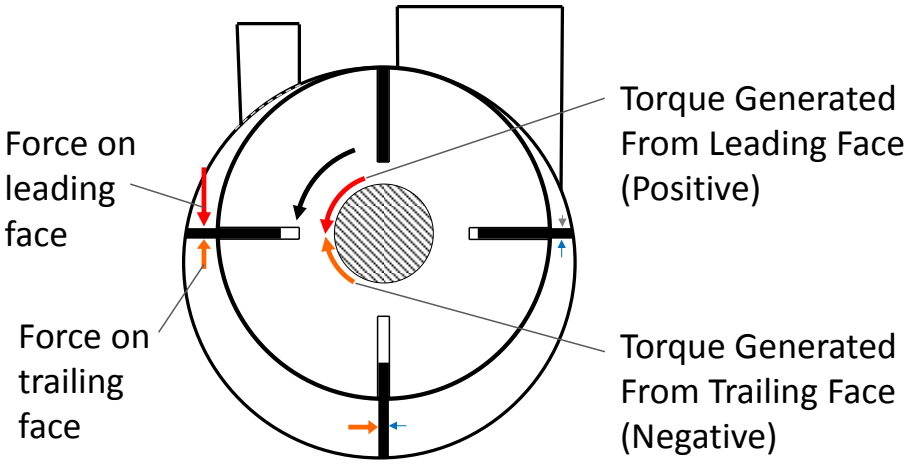

Figure 8 - Schematic of the forces generated from the cells in a vane motor acting on the vanes of the motor, and the resulting positive and negative torques that are applied to the rotor.

Figure 9 illustrates the geometric dimensions (or variables) of a basic (circular stator) pneumatic vane motor. Non-circular (or non-cylindrical) stators have been developed to optimize the geometry of the motor, but these improvements are still subject to the geometric limitations of the motor (23). Principally, the ideal power output of the motor (circular or non-circular) is a function of the displaced volume (displacement), which is the total volume of working fluid induced into the cells of the motor with one full rotation (17). The displacement of the motor is a function of the rotor radius, stator radius, and length of the motor, and the rotor radius and stator radius is limited by the maximum allowable vane travel (17). The maximum allowable vane travel is limited by the strength and size of the vane, as the vane is essentially a cantilevered beam extended from the vane guide, and is subject to high stresses from frictional and pressure forces (16). Specifically, it has been found that the ratio of the rotor radius to the maximum stator radius is between 0.75 to 0.95, the ratio of the maximum vane travel to the vane height is between 0.5 to 0.6, and the ratio of the height of the vane to the rotor radius is 0.5 to 0.6 (23).

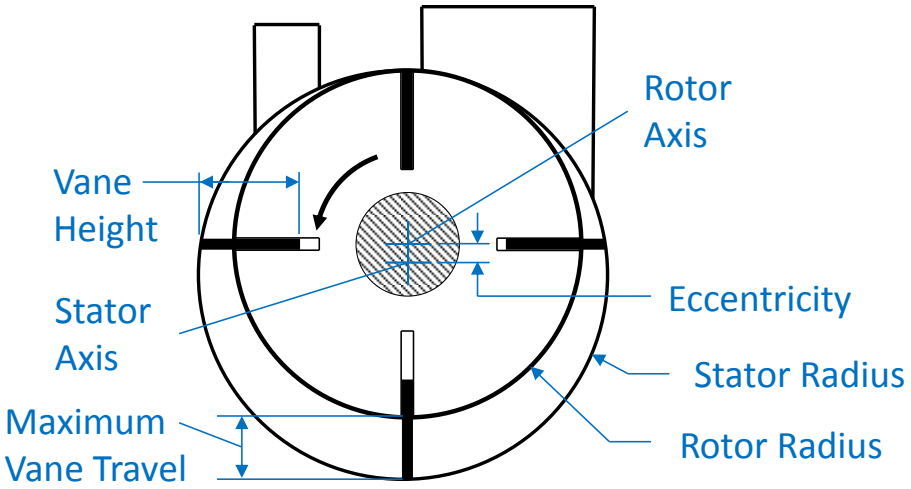

Figure 9 - Geometry of a basic pneumatic vane motor.

A further limitation is that rectangular (or apex) shaped seals need to be used. This shape is used because the seal has to slide along the faces of the vanes of the rotor to compensate for the gap between the rotor and the stator (due to the eccentricity of the rotor). This shape is disadvantageous because the seals tend to wear unevenly due to the uneven pressure distribution from the corners on the seals (24; 25). Additionally, the seals tend to chatter at lower speeds, which will cause excessive internal leakage (22). A solution to this is to apply additional spring or pneumatic forcing to maintain contact with the stator wall, which prevents leakage. However, this leads to increased frictional losses in the motor (20).

Figure 10 illustrates the displaced cell area (sectional area of the cell volume illustrated in Figure 7), which is the volume per unit length of the motor of a circular four-vane pneumatic motor. The cell area is presented in this manner as the length of the motor will vary depending on the application, and the displaced volume is directly proportional to the length of the motor. This figure demonstrates how the cell volume is derived from the difference of the swept volume of the leading and trailing vanes surrounding the cell. Additionally, the maximum cell volume is highlighted. The maximum cell volume can be used to assess the geometric characteristics of a broader range of vane motors, as discussed below. Note that effect of the volume occupied by the vanes of the motor are neglected (assumed to have zero thickness), as this has been demonstrated to have negligible effects on the volume calculations of the motor (20).

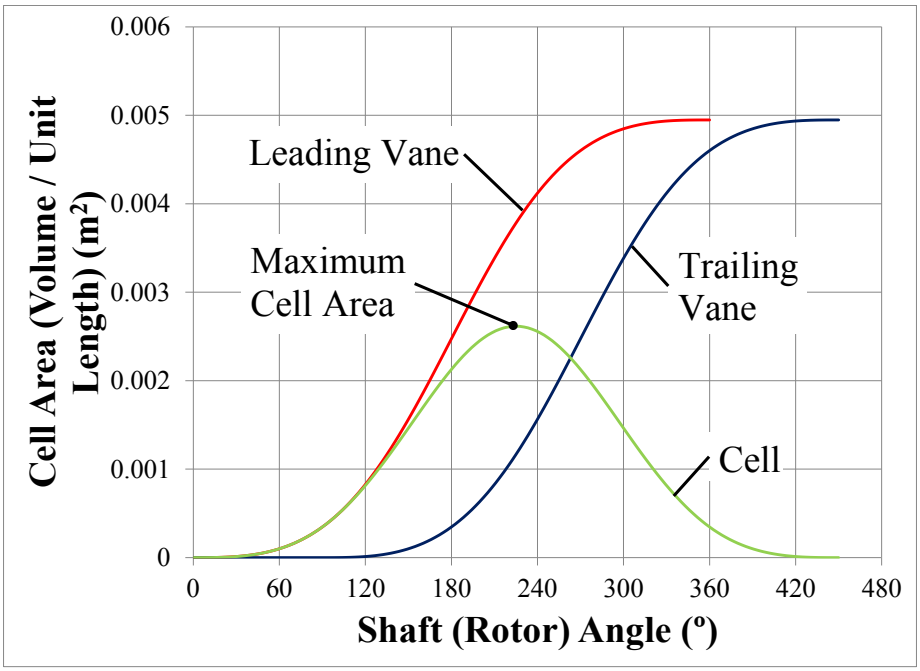

Figure 10 - Displaced area (cell volume per unit length) of a circular four vane pneumatic motor with a rotor radius of 45mm, stator radius of 60mm, stator eccentricity of 15mm, and 4 vanes. The cell area (volume per unit length) is presented, which is the difference between the displaced area of the leading vane and the trailing vane (17).

The volume V swept by a vane, as a function of the shaft (or rotor) angle α, is given by:

$$V(\alpha) = \frac{L}{2}\left({R_s}^2\beta(\alpha) - {R_r}^2\alpha - eR_s\sin\beta(\alpha)\right) \qquad \textit{Eq. 3 (17)}$$

Where, L is the motor length, R_s is the stator radius, R_r is the rotor radius, e is the eccentricity, and

$$\beta(\alpha) = \alpha - \sin^{-1}\left(\frac{e\sin\alpha}{R_s}\right) \qquad \textit{Eq. 4 (17)}$$

Further, the volume in a cell V_{cell} as a function of the shaft angle is given by:

$$V_{cell} = \begin{cases} V(\alpha) & 0 < \alpha \leq \gamma \\ V(\alpha) - V(\alpha - \gamma) & \text{for} \quad \gamma < \alpha \leq 2\pi \\ V(2\pi) - V(\alpha - \gamma) & 2\pi < \alpha \leq 2\pi + \gamma \end{cases} \qquad \textit{Eq. 5 (17)}$$

Where, the angle between vanes γ is a function of the number of vanes n_v, which is given by:

$$\gamma = \frac{2\pi}{n_v} \qquad \textit{Eq. 6}$$

The maximum cell area (or volume per unit length), as highlighted in Figure 10, is a critical characteristic of these motors. Specifically, this characteristic is a driving constraint for the size and locations of the inlet and outlet ports, number of vanes, and selection of rotor and stator size, and expansion ratio (17). The expansion ratio ϵ is the maximum cell volume ${V_{cell}}^{max}$ divided by the cell volume when the cell is sealed off from the inlet port ${V_{cell}}^{fill}$, or the maximum sealed volume of the working fluid divided by the minimum sealed volume of the working fluid in the motor. The expansion ratio is calculated as:

$$\epsilon = \frac{{V_{cell}}^{max}}{{V_{cell}}^{fill}} \qquad \textit{Eq. 7}$$

The maximum expansion ratio depends on the application, and is limited by the minimum temperature and pressure of the working fluid leaving the motor (23). For example, it is recommended that compressed air motors limit the expansion ratio to below 1.2 to prevent freezing of water vapor within the working fluid from freezing in the exhaust ports or ducts (26). Further, with a generally fixed expansion ratio (or expansion ratio independent of other constraints of the motor), it is advantageous to maximize the cell area of the motor, to allow for increased port size, increased displacement, and minimize overall motor size and mass. Therefore, the maximum cell area of a motor can be used as an indicator to assess the versatility for the motor to be designed for certain constraints; i.e. a higher maximum cell area for a given stator diameter, provides more design flexibility for optimizing port location and area, number of vanes, and rotor size.

Figure 11 illustrates the maximum cell volumes for vane motors with the rotor-to-stator ratios recommended by Badr (23), and the most common number of vanes as described by Beater (5).

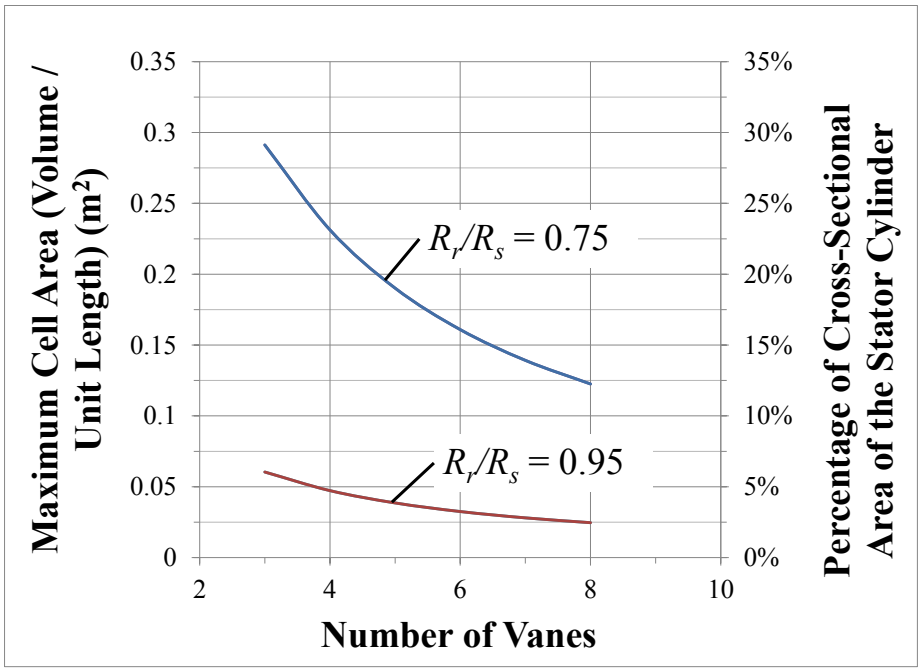

Figure 11 - Maximum cell area (Volume per unit length) of vane motors with 3 to 8 vanes, a rotor radius of $\sqrt{\frac{1}{\pi}}$ *m, and an upper and lower rotor to stator (R_r / R_s) ratio of 0.75 and 0.95, as recommended by Badr (23). The cell area is also presented as a percentage of the cross-sectional area of the stator cylinder, which is 1 m².*

It is seen in Figure 11 that the maximum cell area with the most aggressive rotor-to-stator ratio is limited to approximately 12.5 to 30% of the stator cylinder cross-sectional area, of which the variance in the cell area is dependent on the number of vanes in the motor. Further, in order to directly compare this characteristic to other motor designs, the displacement of this type of motor can be evaluated. The displacement V_{disp} of the motor is the volume of working fluid displaced with one full shaft rotation (9), and is calculated by:

$$V_{disp} = n_v {V_{cell}}^{fill} = n_v \frac{{V_{cell}}^{max}}{\epsilon} \qquad \textit{Eq. 8 (17)}$$

Figure 11 illustrates the displacement of vane motors with expansion ratios of 1.0 and 1.2. These expansion ratios were selected because an expansion ratio of 1.0 will provide the maximum displacement, and an expansion ratio of 1.2 is the recommended expansion ratio for conventional pneumatic (compressed air) systems. Additionally, the most

aggressive (0.75) rotor-to-stator ratio was used because this will also provide the maximum displacement.

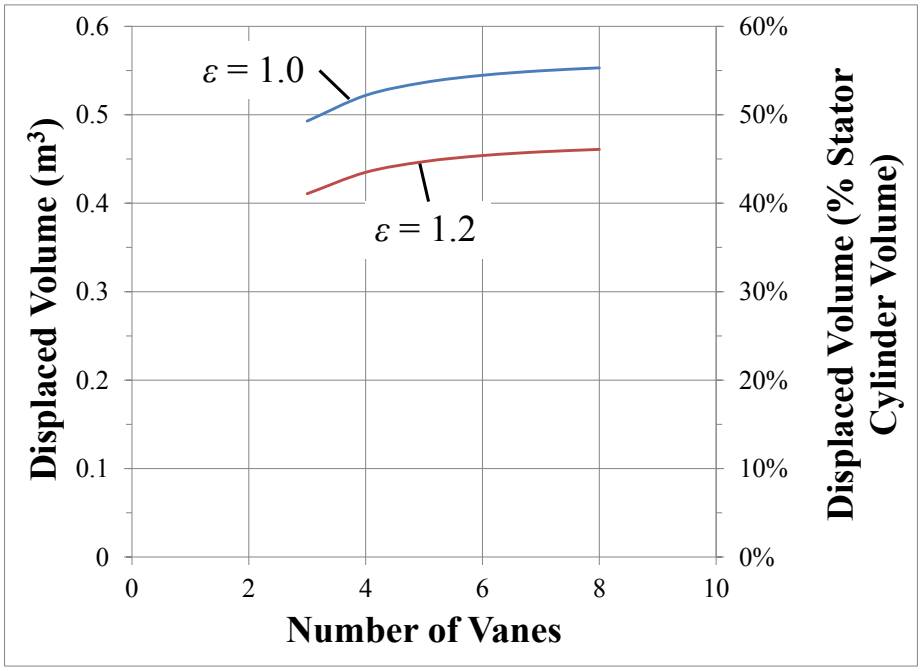

Figure 12 - Displaced volume of vane motors with selected expansion ratios and number of vanes, with a stator radius of $\sqrt{\frac{1}{\pi}}$ *m, rotor-to-stator ratio of 0.75, and stator cylinder length of 1m. The displaced volume is also presented as a percentage of the stator cylinder volume, which is* $1m^3$.

It is seen in Figure 11 that the maximum displacement of vane motors is approximately 50 to 55% of the stator cylinder volume, with the geometric constraints described above. Additionally, it is seen that the number of vanes in the motor increases the displacement of the motor, but the overall difference for the number of vanes shown is an increase of approximately 5%.

In summary, it has been demonstrated that vane motors have inherent geometric limitations such as rectangular shaped seals, negative torque effects of trailing vanes, and displacement limited to 50 to 55% of the stator cylinder volume. Therefore, improved designs or concepts should be focused on improving these characteristics.

CHAPTER 3 TOROIDAL MOTORS

An alternative design to conventional pneumatic motors is a toroidal motor (27; 28). The fundamental difference of these motors is the geometry of the working chamber of the motor, where the working chamber is volume enclosed by the motor to process a working fluid (12). In particular, the working chamber of a toroidal motor is formed by revolving a circular cross-section around a central axis to form a geometric volume commonly referred to as a toroid (29; 30), and more specifically a ring torus (31). An illustration of this geometry is shown in Figure 13 below.

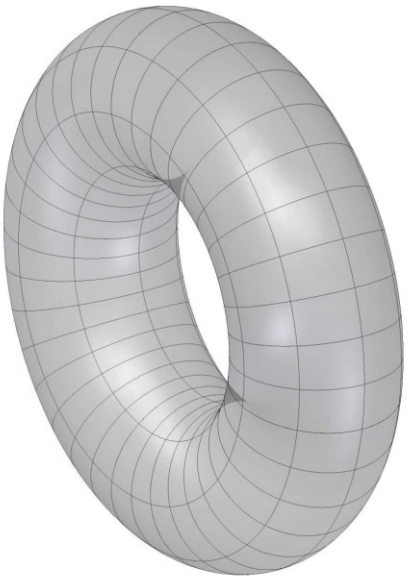

Figure 13 - Illustration of a toroidal volume, or ring torus.

The most common configuration of this shape of motor uses two rotors and an equal number of vanes (or pistons) on each rotor, which have primarily been developed for use as an internal combustion engine (27; 30). An illustration of a toroidal motor with two rotors is shown in Figure 14. Furthermore, a detailed review of toroidal motor (or engine) designs is included in Chapter 4, and this chapter focuses on the general design principles of the novel pneumatic motor developed and tested in this thesis.

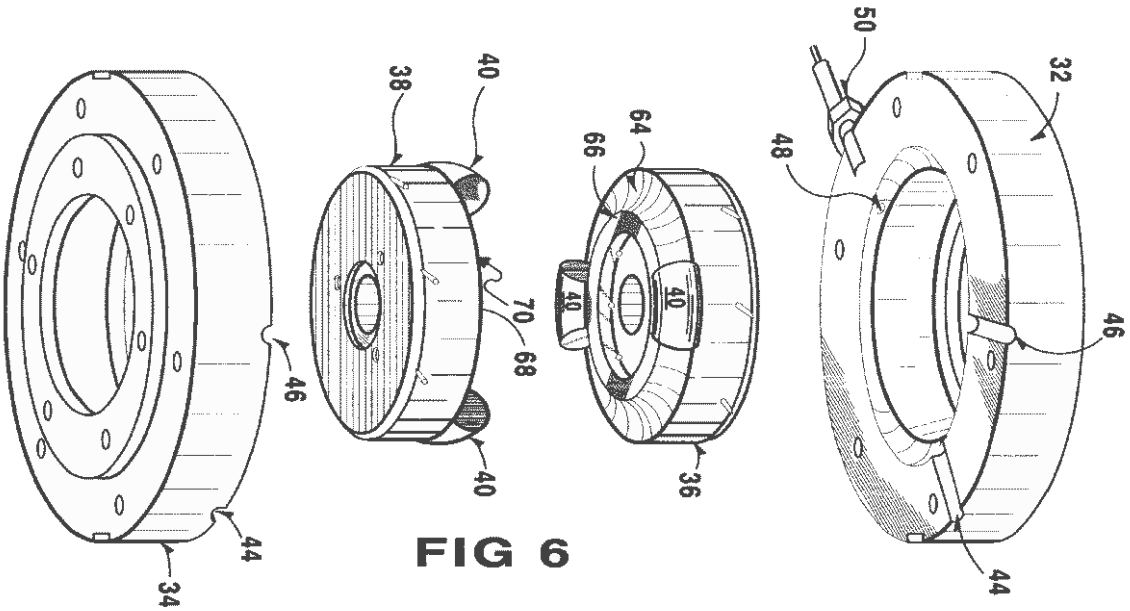

FIG 6

Figure 14 - Illustration of a toroidal motor, showing the sections of the toroidal working chamber (48 & 64), two rotors (36 and 38), two pistons on each rotor (40), two sections of the stator (32 and 34), and inlet and outlet ports (44 and 46) (27).

It is seen in Figure 14 that the pistons are spaced equally on each rotor, and when the motor is assembled, the two rotors and the two sections of the stator (also called chamber or housing) form the toroidal working chamber, and the pistons separate sealed cells within the working chamber (32). A schematic of these components and the working cells formed in the motor is illustrated in Figure 15.

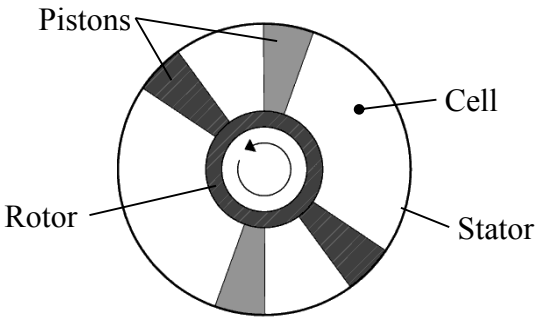

Figure 15 - Schematic of the components forming the cell volumes in a toroidal motor.

This configuration allows the rotors to rotate independently, which varies the volume of cells formed between the pistons. This is a common characteristic of all of these types of motors. However, all the toroidal motor designs vary in the method of power transmission from the rotors to a common drive shaft, and vary in the method of timing

the motion of the rotors with respect to ports in the stator or casing. These commonalities and variance are described in detail in Chapter 4.

3.1 Principles of the Novel Toroidal Motor

The novel toroidal pneumatic motor designed, developed, and tested in this thesis is operated based on the following principles:

- Two rotors and a stator form the toroidal chamber of the motor;
- An equal number of pistons on each rotor seal cells of variable volume within the chamber;
- Ports are located on the stator to allow the flow of a working fluid through the motor;
- An impact mechanism operably positions the rotors with respect to the stationary ports, and in combination with the flow of a pressurized working fluid, controls the intermittent rotation of the rotors to expand and contract the volume of the cells formed within the motor; and
- An arrangement of one-way locking bearings transfer torque from the rotors to a common drive shaft in a forward direction, prevent the rotors from rotating in a backward direction (opposite of the drive shaft), and allow the rotors to rotate independently.

It is thought that the combination of these design principles could provide a pneumatic motor with improved sealing, improved torque output, and improved displacement characteristics, while potentially maintaining the advantage of having few parts and commercially viable manufacturing requirements, as seen with vane motors. However, prospectively from the conception of these principles, it was widely unknown weather this combination would even operate as pneumatic motor, let alone provide the desired improvements as a pneumatic motor. Therefore, it is the focus of this work to develop these design principles, while maintaining a minimal number of parts with minimal custom features. These metrics were chosen to provide a design process that would demonstrate if this novel motor would operate with these design principles, and provide a

contribution of work that would allow further analysis of the potential of targeted performance advantages and commercial viability of this type of motor.

3.2 Detailed Overview of the Novel Toroidal Motor

The toroidal geometry provides a circular cross section of the chamber, which allows the use of conventional compression rings to seal between the various chambers in the motor, as was demonstrated by Bradshaw and described in (33). Compression ring seals are widely used in linear piston applications because they are able to compensate for radial wear and provide an effective seal with minimal friction (34).

The combination of the use of two rotors, the arrangement of one-way bearings, and the impact mechanism allows the rotors to rotate independently between a maximum and minimum angle relative to one-another. This is possible because the rotors are not physically linked, and protrusions on the impact mechanism interfere with one another to prevent the rotors from rotating past a set angle relative to one another. Illustrations and design of the impact mechanism are detailed in Chapter 6, and overview of the independent rotation of the rotors, impact mechanism and one-way bearing arrangement are discussed further below.

The arrangement of one-way bearings transfers torque from each of the rotors when the rotor moves forwards, and prevents each of the rotors from moving backwards. Other toroidal motor designs use a series of gears and linkages to achieve this torque transfer from the rotors to a common drive shaft, as described in Section 4.3.2.3. This provides a ratcheting action between the rotors, where one rotor will temporarily be stationary and the other will be rotating (and rotating the drive shaft). The conventions for these actions are referred to as backstopping and indexing for the stationary and moving rotors respectively. This arrangement fundamentally changes the torque characteristics of the motor, when compared to vane motors. In particular, each cell in the motor is sealed by two pistons, which are attached to opposite rotors. Therefore, the pistons are able to move independently as the cell volume changes, and only the torque acting on the moving piston is transferred to the drive shaft. This is illustrated in Figure 16, where the indexing torque, or torque transferred to the drive shaft from the rotating rotor, and the

backstopping torque, or torque held by the stator from the stationary rotor, are highlighted.

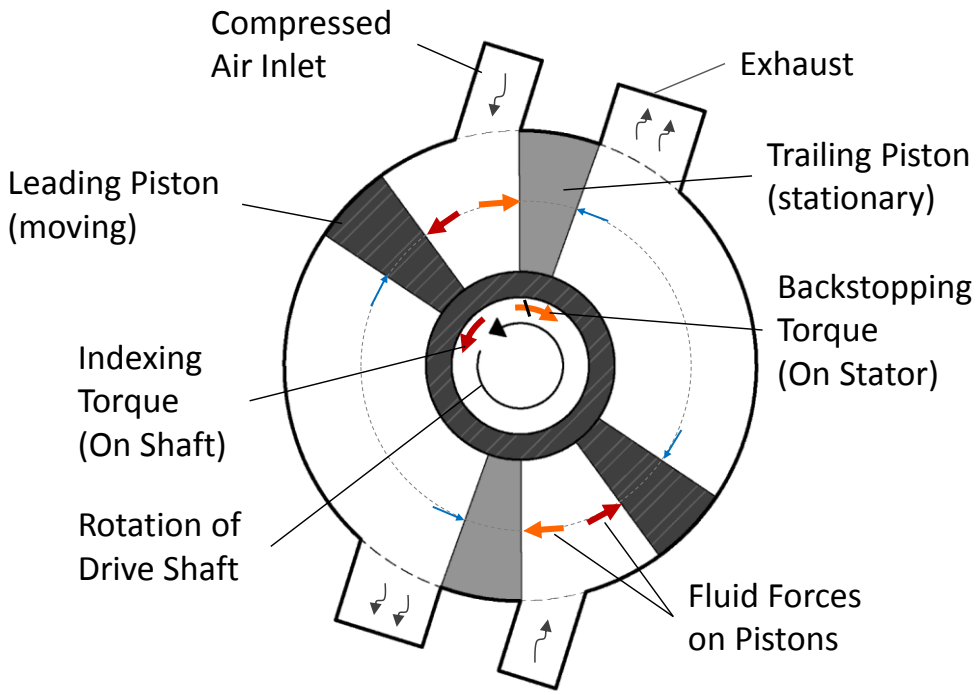

Figure 16 - Schematic of a toroidal motor showing the indexing torque acting on the drive shaft, and the backstopping torque acting on the stator (or housing).

The volume formed by revolving a circular area, with a radius of R_p around a central axis at a constant radius R_c as a function of the revolved (or shaft) angle θ is given by:

$$V(\theta) = \pi R_c {R_p}^2 \theta \qquad \textit{Eq. 9 (35)}$$

Where the piston radius R_p and rotor radius R_c (central axis radius to the center of the piston) are illustrated in Figure 17, and the stator radius R_{st} is equal to:

$$R_c = R_{st} - R_p \qquad \textit{Eq. 10}$$

The stator radius can be compared as the equivalent stator radius of the motor when comparing to the stator radius of a vane motor. Additionally, the geometry of the toroidal chamber can be characterized by the ratio of the piston radius to the stator radius (piston-to-stator ratio), which has the following physical limits:

$$0 < \frac{R_p}{R_{st}} < 0.5 \qquad \textit{Eq. 11}$$

This physical limit is because the diameter of the piston, or twice the radius, cannot exceed the stator diameter. Further, there are additional components such as the drive shaft, rotors, etc. that are required in the annulus formed in the center of the toroidal chamber. Therefore, this ratio must be below the upper limit; however, the limitations of this are currently unknown.

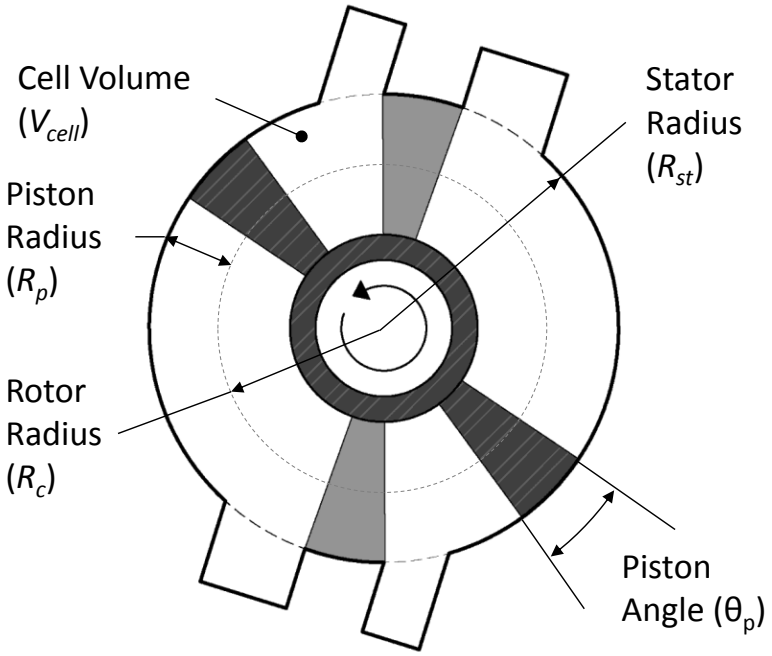

Figure 17 - Illustration of the geometry of a toroidal motor.

The displaced volume of the motor per revolution is a function of the cell volume and the number of cell displacements per shaft revolution. The volume of the cell is a function of the revolved area (piston area), and the angle it is revolved, as shown in Eq. 12, which is derived from Eq. 8, by substituting the minimum and maximum angles between the pistons for the swept angle of the piston area.

$$V_{cell} = \pi R_c {R_p}^2 \theta_{max} + V_{min} \qquad \textit{Eq. 12}$$

Where, V_{min} is the minimum volume of the cell, and θ_{max} is the maximum angle between the pistons, which is a function of the piston angle θ_p and number of pistons n_p as shown below:

$$\theta_{max} = 2\left(\frac{2\pi}{n_p} - \theta_p\right) \qquad \textit{Eq. 13}$$

The minimum volume of the cell is the volume in the cell when the pistons are at the minimum angle. For the analysis below, the minimum volume is neglected (assumed to be zero), because the variance of this is dependent on many factors, and the effects of this volume are currently widely unknown. However, it should be noted, that neglecting this volume does not affect the displacement of the motor, as the maximum displacement of each cell is calculated by:

$$V_{disp}|^{cell} = \pi R_c {R_p}^2 \theta_{max} \qquad \textit{Eq. 14}$$

The displaced volume of the leading piston and trailing piston are shown as a function of shaft angle in Figure 18. Additionally, the cell volume formed between the leading and trailing pistons is shown, and the maximum cell volume is highlighted.

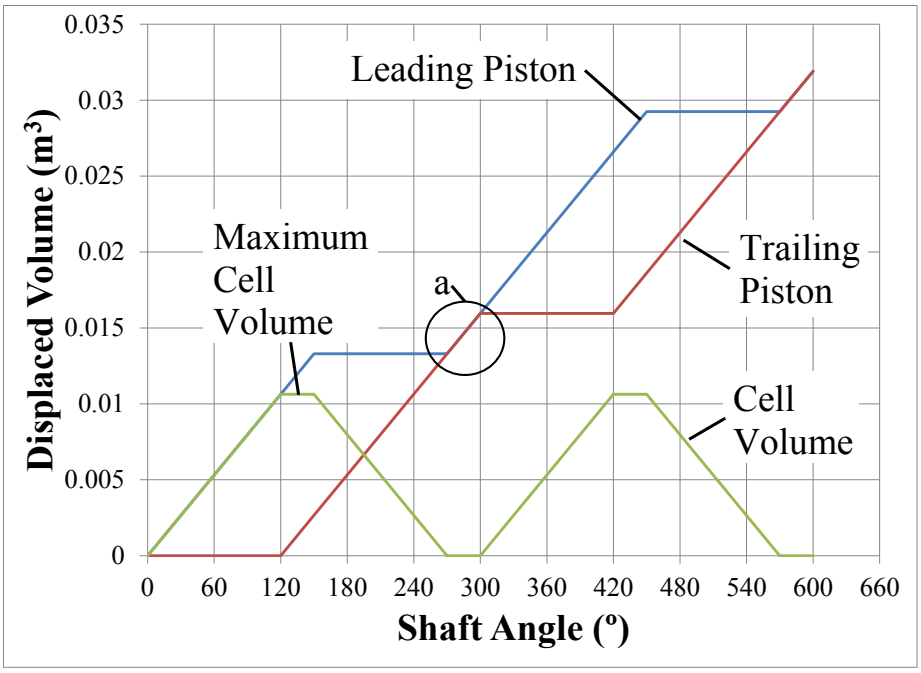

Figure 18 - Displaced volume of a dual rotor toroidal pneumatic motor with a stator radius of $\sqrt{\frac{1}{\pi}}$ m, piston radius-to-stator radius ratio 0.1, piston angle of 30°, and 4 pistons; showing the displaced volume of the leading vane, displaced volume of the trailing vane, and the cell volume between the leading and trailing vane.

It is seen that the shape of the displacement curve is fundamentally different, in that there are times when the leading vane (or piston) and trailing vane are not moving together. In addition, the rate of increase or decrease of the cell volume is a non-continuous linear function of the shaft angle, which is characteristically different than that seen with vane motors. Further, as highlighted by the area labeled "a", it is seen that the leading piston and the trailing piston move together, and no change in the cell volume occurs over this period. This period can be referred to as a "transition" zone, where the impact mechanism transitions the stationary rotor to the moving rotor, and vise-versa. It should be noted that this mechanism is widely unknown, and for the figure shown above, it is assumed that the rotors rotate together throughout the entire transition period.

A further characteristics of this toroidal motor design, is that it is not possible to seal the working cell from the inlet port of the working fluid. This implies that the motor is limited to only displacing the working fluid, and not expanding it. This will have significant efficiency losses, when compressible fluids are used as the working fluid (5; 23).

In order to calculate the number of cell displacements per shaft revolution, it is assumed that the drive shaft does not rotate faster than the fastest rotating rotor at any given time. This is assumption implies that the drive shaft rotates at a constant speed, and the rotors rotate at that speed when in rotation. Any divergence of the actual operation of the motor from this assumption will imply that there are fewer cell displacements per revolution of the motor, because the drive shaft would be rotating faster (although minimally) than the rotors during the transition phase of the rotors. Therefore, with this assumption, the calculated displacement of the motor is ideal, and is calculated as follows.

The cell displacement occurs over a shaft displacement equal to θ_{max}, and the transition phase occurs over a further displaced angle equal to θ_p. Therefore, the displaced shaft angle is equal to the difference between the maximum and minimum angles, plus the minimum angle. Therefore, the shaft displacement is equal to the maximum displacement angle, θ_{max}. The number of cell displacements occurring at any given time is equal to the number of compressed air nozzles connected to the working chamber (n_{noz}), which can be up to half of the number of pistons in the motor (n_p). Therefore, the displacement of the motor, as a function of one full shaft rotation is calculated, as shown in Eq. 15,

$$V_{disp} = n_{noz} V_{disp}|^{cell} \frac{2\pi}{\pi - \theta_p} \qquad \textit{Eq. 15}$$

And substituting Eq. 14 into Eq. 15 gives:

$$V_{disp} = n_{noz} \pi R_c {R_p}^2 \theta_{max} \frac{2\pi}{\pi - \theta_p} \qquad \textit{Eq. 16}$$

And substituting Eq. 13 into Eq. 16 gives:

$$V_{disp} = 4\pi^2 n_{noz} R_c {R_p}^2 \left(\frac{2\pi}{n_p} - \theta_p\right)\left(\frac{1}{\pi - \theta_p}\right) \qquad \textit{Eq. 17}$$

Figure 19 illustrates the displaced volume of a toroidal motor over the range of possible number of pistons, and with various selected piston angles. The range of possible number of pistons has a minimum of two, and a maximum equal to one full revolution (2π) divided by the piston angle.

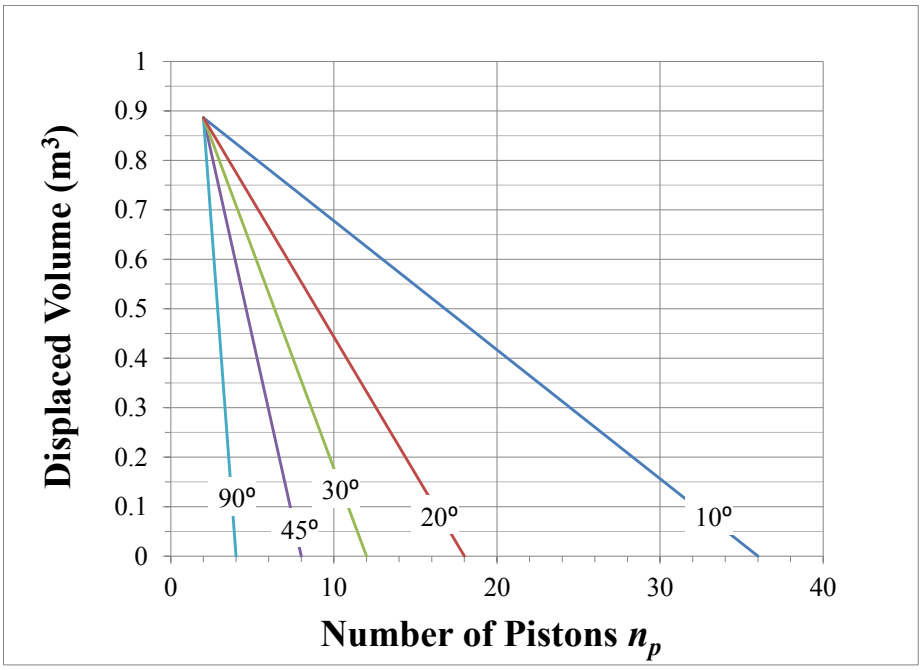

Figure 19 – Displaced volume as a function of the number of pistons for piston angles of 10°, 20°, 30°, 45°, and 90°, with a stator radius of $\sqrt{\frac{1}{\pi}}$ *m, and a rotor-to-stator radius ratio of 0.5.*

It is seen that the upper limit of the range of possible piston angles is 90° with two pistons. However, the lower limit is not known, but it is seen that a lower piston angle is more desirable to increase the displaced volume for a motor with a certain number of pistons. It is also seen that for a motor with two pistons, the displacement is independent of the piston angle. This is useful for evaluating the effect of the piston-to-stator ratio on the displacement of the motor. Figure 20 illustrates the displacement over the theoretical range of piston-to-stator radius ratios with a motor with two pistons, so that the illustrated displaced volume is independent of the illustrated displaced volume.

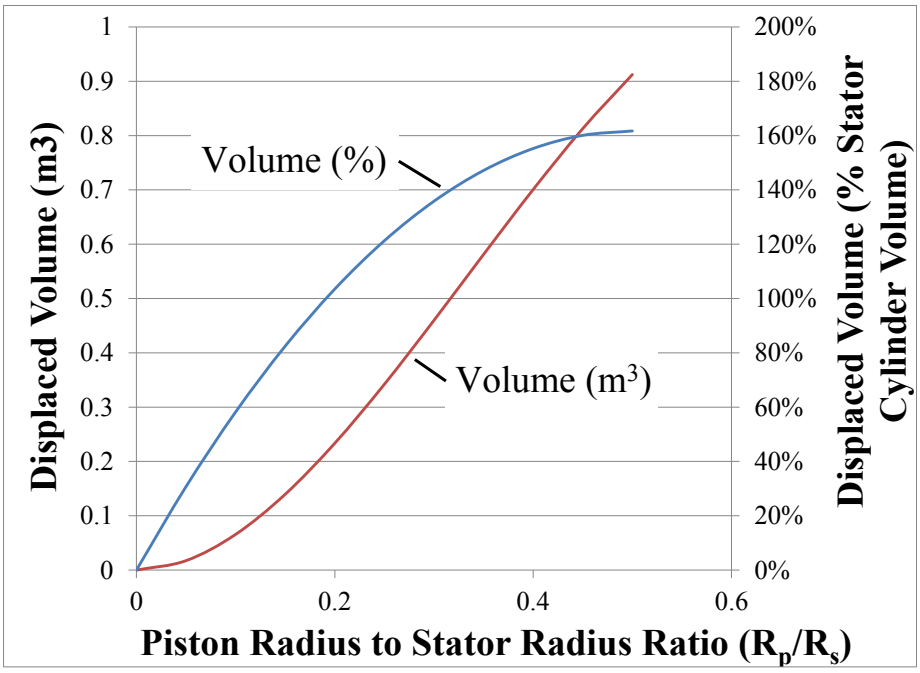

Figure 20 – Displaced volume (m^3) of a toroidal motor with two pistons, a stator radius equal to $\sqrt{\frac{1}{\pi}}$ m, one nozzle, as a function of the piston-to-stator radius ratio (between 0 to 0.5); and displaced volume as a percentage of the volume of a cylinder with the equivilent stator radius, and length equal to the piston diameter (or twice the piston radius R_p).

It is seen that the displacement of the motor increases by increasing piston-to-stator ratio. Therefore, in order to maximize the displacement of a motor with a given stator radius, the piston-to-stator radius ratio should be maximized.

Further, Figure 20 illustrates the displacement as a percentage of the volume of a cylinder with an equal stator radius, and length equal to the piston diameter. This percentage is used to compare the displacement of the toroidal motor to a vane motor. It is seen that the toroidal motor can have a displacement of up to 160% of the cylinder volume, where as a vane motor can have a displacement of up to 55% of the cylinder volume. This comparison to evaluate the advantage of a toroidal shaped working chamber over a vane motor, and does not account for the components surrounding the working chamber, such as the bearings for a toroidal motor, which will affect the overall motor size. However, it demonstrates that there are fundamental displacement advantages of the toroidal motor, which increases the amount of working fluid that can flow through a motor of a given size, and increases the potential power density of the motor.

CHAPTER 4 REVIEW OF TOROIDAL MOTORS AND ENGINES

A common theme seen with the reasoning, or goals of the inventions, with toroidal motors in the patents presented in this chapter is that the rotary motion of the pistons are to provide an engine with minimal vibrations, and a more direct energy transfer from the pistons to the drive shaft. In other words, the general goal of toroidal engines, as seen from reviewing the patents presented in this section, is to convert rotary piston motion directly to rotary shaft motion, rather than linear piston motion to rotary shaft motion as seen in conventional engines. In addition, many toroidal engines can be designed with ports in lieu of valves depending on the transmission mechanism, thus potentially providing a mechanically simpler device.

Toroidal engines generally use two rotors, which have an equal number of pistons attached. The two rotors form a portion of the toroidal chamber, and a casing forms the remaining section of the chamber. The casing can be fixed or rotating. However, simpler designs include a fixed casing, which contains the intake ports, exhaust ports, and ignition ports. Engine designs with a rotating casing require rotating valves, ports and spark plugs, which generally leads to sub-optimal designs.

Toroidal engines allow the use of conventional compression rings to seal between the combustion chambers. In addition, the angle between the face of the seal and the chamber is constantly perpendicular. This provides a more uniform force interaction between the seals and the engine casing, when compared to apex seals seen in the Wankel rotary engine.

4.1 Toroidal Engine Background

It is commonly known that there are three main modes of operation that define the category of an internal combustion (IC) engine: the architecture of the working volume, the method of power transmission, and the integration of timing (36). From this there are many derived systems, which have significant influence on the engine's final

performance. Examples of these are cooling, lubrication, fuel delivery and sealing. The most common type of engine is a conventional reciprocating piston engine. These engines have a cylindrical chamber, a piston-rotor power transmission, and mechanical valve timing. It is commonly known that these engines have inherent inertial limitations due to the reciprocating motion of the pistons (37; 38; 39). An alternative to reciprocating IC engines are rotary engines, where many rotary engine designs have been proposed in the past. However, currently, the only widely commercialized rotary engine is the Wankel (40). This engine is a rotary vane-type engine, which has triangular rotor oscillating within a trochoidal housing. Mazda Motor Company has demonstrated that, if enough resources and expertise are invested into the technology, a rotary engine can be successfully mass-produced and used in a commercial market (36). However, the main problem with this type of rotary engine is the sealing and fuel economy (41). The engine architecture requires rectangular cross-section apex seals to seal between the combustion chambers; refer to Figure 35 in Section 5.1 for illustrations of a apex seal from a Wankel motor. In addition, angle between the face of the seal and the chamber wall varies between acute and obtuse angles as the engine rotates. This causes an uneven force interaction between the seal and the engine housing, which causes uneven wear of the seals, produces chatter zones, and prevents a tight seal (25; 24). Attempts have been made to commercialize the Wankel in non-transportation markets. DGI Industries of Farmingdale, NY worked with Wankel R&D of Lindau, Germany on a 5-10 horsepower natural gas-fuelled rotary engine for heat pump applications from 1985 to 1986. Findings from the project were overheating of the rotor and rotor bearing assembly, limited life of the side and corner seals due to exposure of combustion temperatures, and carbon deposits on the rotor flanks (42).

A solution to using apex seals in rotary engines is to use round pistons, which rotate around a common axis. These engines require an engine chamber which forms the shape of a ring torus, generally referred to as toroidal engine architecture (33). This section focuses on reviewing toroidal engine development to identify the current state of the technology.

The concept of toroidal engines has been around for almost 100 years (43). However, literature on this technology is generally only presented in patents. Given the number of

patents presented in this section, it is seen that multiple attempts have been made to commercialize (or at least protect inventions of) toroidal engines. However, limited information is available about the individual projects or companies involved in the development of these engines. Some Information was found on early projects developed by Granville Bradshaw and Traugott Tschudi (40; 33). Both projects seemed to have successful prototyping, but faced issues with funding further stages of development. More recent developments are seen by inventors Raphial Morgado (Angel Labs LLC) and Monti Farrell (Rotoblock Corp.) (32; 44). Both of the recent companies have demonstrated working prototypes, and seem to be continuing development as of 2012.

4.2 Classification

Generally the commercial limitations have been due to problems with manufacturing, sealing, and timing. Some of these problems may be due to the inherent design of these engines. However, by studying and categorizing past designs, conclusions may be drawn and recommendations made as to the direction for future innovations in this area. Various toroidal engine designs are discussed in this section; they are grouped into the methods of power transmission and of timing the engine cycles. The majority of toroidal engine designs require a mechanism to transmit the motion between two oscillating rotors to a common drive shaft. This is generally the primary differentiation between various toroidal engines. The second differentiation is timing, which in this work is a general term for how the engine cycles between the stages of an internal combustion process.

4.2.1 Power Transmission

The primary differentiation of toroidal rotary engines is based on the method of transferring rotation from the rotor(s) to the driveshaft (*i.e.* power transmission). Two general rotor arrangements have been identified: single rotor, and dual rotor. Single rotor engines transfer power directly to the shaft, and have a mechanical timing/sealing device to create expanding and compressing chambers. Dual rotor engines have two rotors, which create expanding and contracting chambers. An additional mechanism is used to transfer power from each of the rotors to a common drive shaft.

In this review, single rotor engines are briefly described and listed in one category. Fundamentally, this type of toroidal engine has a single rotor, and a valve mechanism to control the timing of the engine cycles. Therefore, the design and operation of these toroidal engines tends to converge and are discussed briefly. The focus of the discussion is on dual rotor engines and the variances in their design. Dual rotor engines can be categorized into three methods of power transmission: geared linkages, cammed linkages, and unidirectional. Geared and cammed linkages are generally similar, as the rotors are connected to a linkage, which dictates the location of the rotors, casing and drive shaft with respect to one another. However, since all the power is transmitted through the linkage, variations in the design can produce dramatically different results. A third method is unidirectional power transmission, which uses one-way bearings (also referred to as clutch bearings or clutch mechanisms) to transfer power to a common drive shaft from each of the rotors. Dual rotor engines with one-way bearings allow each rotor to transfer power to the drive shaft in an indexing manner to create continuous shaft motion with two rotors. One-way bearings transfer power from the rotors to the drive shaft in one direction, but rotate freely in the other direction. This means that the rotors are not directly linked; a fundamental difference in the operation of these types of engines. One-way bearing arrangements typically transfer power more directly and efficiently while geared linkages are often quite complex and large. However, since the one-way bearings do not directly connect the rotors at all times, an additional timing method is required for engines with unidirectional power transmission.

4.2.2 Timing

The next level of differentiating a toroidal rotary engine with a one-way bearing arrangement (unidirectional power transmission) is its engine timing mechanism. Engine timing is critical to engine performance as it controls the fuel ignition, and dictates air flow through the engine (intake and exhaust) thus controlling the engine power output. Three main methods of timing are seen in engines with unidirectional power transmission. These methods are reciprocating, electrical and mechanical timing. A reciprocating timing system requires the rotors to reciprocate, and a valve system controls the airflow to the chambers. One-way bearings are used to transfer the oscillating,

reciprocating rotor motion to a continuous shaft output. A purely electrical timing mechanism will, at its core, track the position of the various pistons using electrical sensors. Mechanical timing systems are generally simpler and rely on a physical switch or pulse of some kind to trigger ignition.

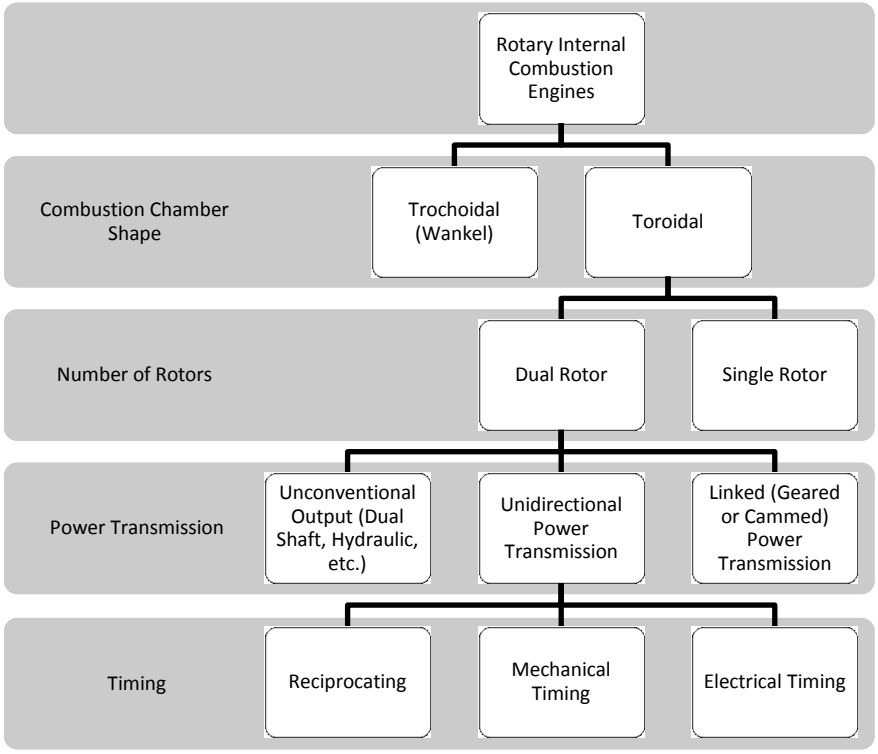

Figure 21 - Rotary engine classification system.

4.3 Detailed Review of Toroidal Engines

The rotary engine classification is summarized in Figure 21 below. The figure outlines how the toroidal engine designs described in Section 4.3 are classified. As mentioned above, the focus of this section is to discuss the variances power transmission and timing methods in dual rotor engines. Therefore, single rotor designs are categorized separately and discussed briefly.

4.3.1 Single Rotor

Single rotor engine designs use a bypass chamber to store the compressed air of the compression stroke. An actuated or passive valve system is used to allow the compression gases back into the toroidal chamber on the other side of a disk valve. This

forms an expandable chamber with compressed air and fuel, to which a spark can be introduced (45; 46; 47). A variation of this type of engine separates the compression and combustion cycles into two separate toroidal chambers, and injects the compressed air into the combustion chamber as needed (48; 49; 50). The primary differences between the two methods are that there are two toroidal engine chambers required for the latter designs, but each chamber could be temperature controlled as desired. However, this method of engine operation is referred to as a split-cycle engine, and is currently under development in reciprocating engines (51). Furthermore, it is not necessary that the engine be a toroidal shape for this process to work. Therefore, focusing development on this technology with toroidal engines has not been intensively pursued. In order to achieve expandable and compressible chambers with these engine designs, a complex gate valve is required in the chamber. Figure 22 illustrates a gate valve that is used to create an expandable chamber, while being controlled to allow the piston to pass. It is seen that this arrangement requires complex cams and linkages to achieve the desired sealing.

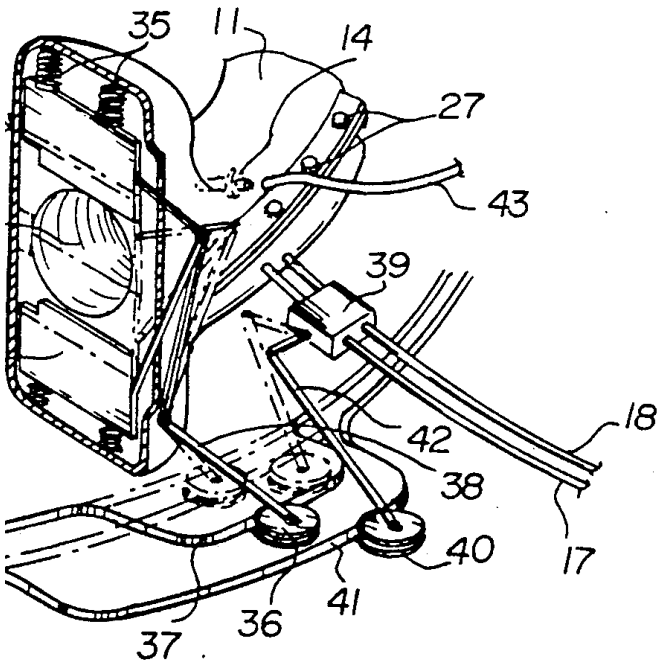

Figure 22 - Illustration of gate valve used to create a closed chamber with a single rotor toroidal engine (49).

Variations of this valve configuration are seen (48; 49; 50; 52), however, all designs have the inherent issue of assembling a seal within the toroidal chamber. This proves to be

difficult as there are static seals between various parts of the casing, combined with dynamic seals between the valve and the casing, and further dynamic seals between the pistons and casing. Therefore, these designs have not been favored because they provide additional sealing challenges to that seen in other toroidal engine configurations.

Another single rotor design has a stationary housing, but no valves or split-cycle configuration (53). Rather, two sets of pistons are mechanically controlled to intermittently connect to either the rotor or the casing. This provides similar operation to that seen with the dual rotor engine designs, but requires a more complicated mechanism for power transmission and piston control. Therefore this configuration is less desirable, as the mechanism to control the pistons adds another degree of complication to the engine design.

4.3.2 Dual Rotor

Single rotor designs are characterized by one rotor which is directly attached to the output driveshaft. In order to have expanding and compressing chambers, complex valve systems or linkage mechanisms are required. Therefore, an objective of dual rotor toroidal engines is to achieve the advantages of toroidal engines without the requirement of complex mechanisms. In the following sections various dual rotor designs are discussed, classified by their method of power transmission.

4.3.2.1 Unconventional Power Output

This section reviews toroidal engines with unconventional power output. An unconventional power output is anything that isn't a single constant speed shaft output. Table 1 lists the toroidal engine designs of this type with a brief description of the timing means used.

Table 1 - Timing methods of unconventional power output toroidal engines.

Inventor(s)	Year	Reference	Timing Method
Barrera, R. M.; Barrera, R. A.	2002	(54)	Spring-loaded pins act as positional guides for rotors on dual-shaft output (one for each rotor).
Hoose, K. V.	2005	(55)	Actuated valves control the timing of the rotors on dual shaft output (one for each rotor).

Inventor(s)	Year	Reference	Timing Method
Hoyt, S. W.	2002	(56)	Hydraulic chambers directly connected to the combustion chambers produce hydraulic pump output.
McMaster, H. A.	1971	(57)	A closed hydraulic circuit within the engine controls the timing and transfers power from the rotors to a common drive shaft.

4.3.2.1.1. Dual Shaft Output

Several engine designs were found with dual shaft output (54; 55). This provides a simple design, but a further mechanism is required to transfer the intermittent motion from the two output shafts to one constant motion drive shaft. One engine uses a set of spring-loaded pins, to prevent the rotors from rotating backwards, and to prevent the rotors from moving past a desired position, relative to the other rotor and a stationary housing (54). Therefore both of the shafts rotate in the same direction intermittently.

Another design consists of an inner and outer rotor, as shown in Figure 23. The inner and outer rotors form the toroidal chamber, and an equal number of pistons are mounted to each of the inner and outer rotors. An intake or exhaust valve is located within each piston, depending on which rotor the piston is attached to; all of the intake pistons are on one rotor, and all of the exhaust pistons are on the other rotor. Furthermore, the rotors act as an intake or exhaust manifold, with ducts directing air to or from the pistons.

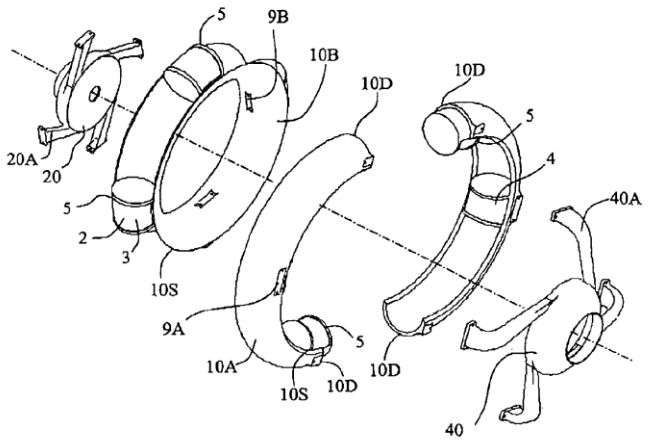

Figure 23 - Example of reciprocating toroidal engine (55).

The valves are controlled electromechanically, pneumatically, or hydraulically. Combustion in the chambers will force the two rotors apart, and the rotors will rotate in

opposite directions. The inner and outer rotors are connected by a circular rack and pinion gear train that ensures equal rotation of the rotors (55). The mechanism for power take off of the rotors is not detailed, but it is suggested that a mechanical transmission or electric alternator be used.

4.3.2.1.2. Hydraulic Output

An alternative to shaft output is hydraulic output, which directly transmits intermittent rotor motion directly to hydraulic pump work (56). The engine has a set of stator pistons, which are fixed to the engine housing, and a set of free pistons, which are connected to the working hydraulic vanes. The free pistons reciprocate between the stator pistons, creating expandable and compressible chambers. The chambers are mechanically timed by rotary ball valves or similar means. Figure 24 illustrates an engine with square shaped pistons, but the concept could be applied to a toroidal shaped chamber.

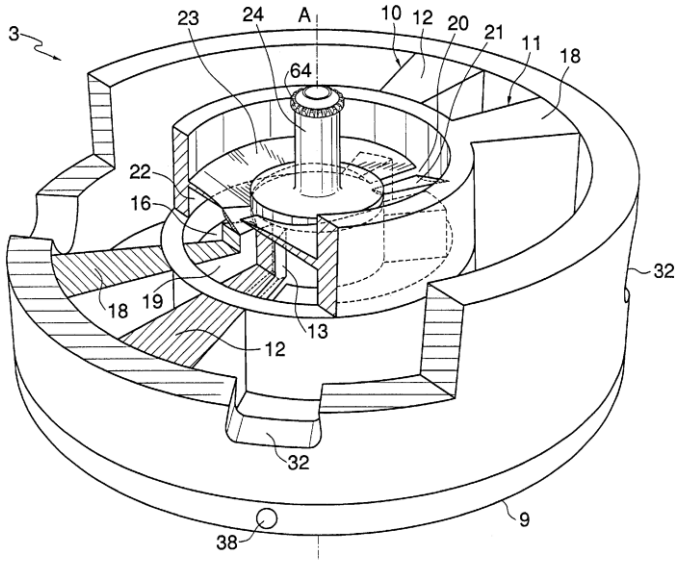

Figure 24 - Rotary engine converting intermittent rotor motion directly to hydraulic pump work (56).

An earlier engine used hydraulic timing similar to the aforementioned design (57) but used a closed hydraulic circuit, which rotates with the drive shaft. The circuit is divided into equally spaced hydraulic pistons, which are radially mounted and actuated about the drive shaft. A stationary cam determines the volume of each cylinder as a function of the position of the drive shaft. The number of pistons is equal to the number of gas chambers

formed by the toroidal cylinders in the engine. Each toroidal gas chamber has an adjacent hydraulic chamber. The vanes of the hydraulic chambers are fixed to the corresponding pistons, therefore providing hydraulic chambers that are in sync with the gas chambers. The hydraulic chambers communicate with the hydraulic pistons to create oscillating motion between the rotors.

4.3.2.2 Unidirectional Power Output

A more unique method of integrated power transmission uses one-way bearings or clutch mechanisms. The clutch mechanisms transfer power from each rotor to the drive shaft in one direction, and prevent each rotor from rotating in the other direction. This configuration provides a constant shaft output from the intermittent motion of the rotors. However, some method of timing is required to control and integrate the piston motion with the spark timing which is discussed in detail below.

Table 2 summarizes the timing methods of toroidal engines with one-way bearing power transfer. These engines are discussed in detail further in the section. The reader should note that the term "one-way bearing" is also known as a "one-way clutch".

Table 2 - Summary of timing methods of engines with clutch mechanisms.

Inventor(s)	Year	Reference	Timing Method
Krikorian, M.A.	1917	(43)	Timing mechanism mechanically fixes rotors to driveshaft to position in correct ignition location.
Nutku, A.	1975	(58)	Pistons reciprocate in toroidal chamber.
Rigternick, D.L.	1980	(59)	Piston and chamber counter-rotate and brake mechanisms couple the chamber and piston to either the shaft or stationary housing, depending on the stage of the engine cycle.
Farb, N.E.	1966	(60)	Mechanical timing operated by sliding valves.
Chevalllier, M.; Poulain, G.	1931	(61)	Mechanical timing (operated by timing disk geared to each rotor) actuates sliding valves.
Potter, M.C.	1965	(62)	Rotating housing uses multiple one-way bearings between rotors, fixed grounding, driveshaft, and housing.
Rubinshtein, B	1982	(63)	Valves within the pistons operate independent of the rotors positions relative to the housing. Valves are actuated mechanically or electromechanically.
Kovalenko, G.E.	1993	(64)	Hydraulic valves within the pistons are controlled to actuate from a central control manifold.

4.3.2.2.1. Reciprocating

An application of reciprocating rotary motion is used in an engine with a partial toroidal chamber of circular cross section, but less than 180° swept angle. The piston extends into the chamber, and is rotatable around the center axis of the toroid. Combustion forces the chamber and the piston apart, and a series of brake mechanisms hold the stationary members in place, and fix the working members to the drive shaft. The chamber housing and the piston are able to either couple to the shaft or to the stationary housing, depending on the stage of the two or four-stroke process (59).

Another application of reciprocating rotary motion is used in an engine with a full toroidal chamber, with two rotors illustrated in Figure 25. The rotors are permitted to oscillate, and through a transmissions system, including one-way clutch mechanisms, transmits the oscillating motion to a common drive shaft (58).

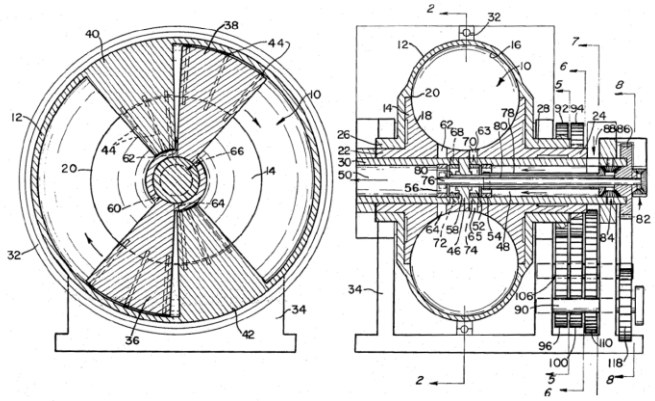

Figure 25 - Example of reciprocating toroidal engine with a transmission incorporating one-way clutch mechanisms to a common shaft (58).

4.3.2.2.2. Mechanical Timing

Early engine designs with clutch mechanisms include two rotors with an equal number of pistons attached to each rotor. The engine is timed with two rotating slide valves, which are driven by the intermittent motion of the rotors (60). A variation of this design uses two pistons attached to each rotor, and five intake, exhaust, and spark plug ports located around the annulus of the toroidal chamber (43). An additional timing disc is geared to each rotor, with the disc rotating at 1/3 of the speed and in the opposite direction of the corresponding rotor. Each timing disc has an elongated intake and exhaust port, and acts

as a slide valve against the ports opening to the toroidal chamber. This provides a valve timing system, which depends on the position of each rotor.

A variation of a design with a clutch mechanism uses a rotating housing and a single rotor (62). The rotating housing has at least two toroidal chambers or a single chamber divided with barriers. A piston is positioned within each chamber, and all the pistons are attached to the rotor. The rotor and body have a clutch as a means of preventing backwards rotation as well as transferring motion from the bodies to the drive shaft in the forward direction. The engine has fuel induction and exhaust means, which intake fuel/air into the expanding chambers, and exhaust from the compressing chambers. However, the method of timing the exhaust, fuel induction, and ignition is not specified in the patent document (62).

A similar engine design uses valves to control the timing of the engine cycles (63). The valves are contained within the rotors for each independent chamber, and each set of particular fluid flows is connected to a stationary manifold, through a rotary seal. The valves are controlled by a mechanical or electromechanical system, as a function of the rotors with respect to one another, independent of the rotor's position to the stationary housing (63).

An additional engine uses two rotors with an equal number of pistons attached to each. The rotors have clutch means for preventing backwards rotation, and additional clutch means for transferring motion from the rotors to the drive shaft in the forward direction. However, the engine has fixed port locations and uses a mechanism, which temporarily attaches the rotors to the drive shaft to reposition the pistons at the correct firing positions (43).

4.3.2.2.3. Electrical Timing

An engine design with a planetary gear train coupled with one-way bearings (64) is seen in Figure 26. The mechanism is configured such that the rotors are constrained from rotating slower than the drive shaft, and the rotors drive the drive shaft through a planetary gear train. This implies that during the power stroke in the engine, the driving rotor is rotating at a fixed ratio relative to the following rotor. Also, hydraulic valves are

contained within the rotating piston heads and are electrically controlled based on the positions of the pistons.

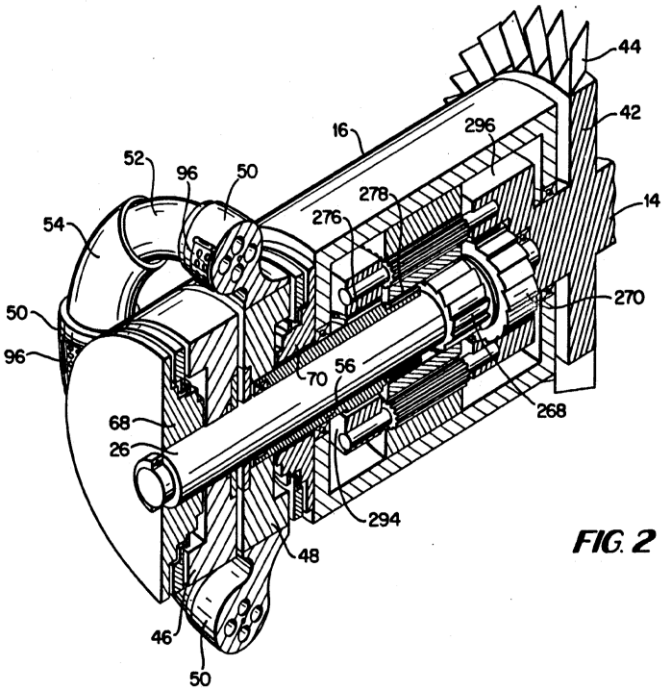

Figure 26 –Example of toroidal engine with clutch mechanisms transferring power through a planetary gear train (64).

4.3.2.3 Linked Power Transmission

The most common method of integrated power transmission for toroidal engines with dual rotors is with geared or cammed linkages. These linkages generally connect both rotors to a common drive shaft such that the rotors will be in a predetermined position, depending on the position of the drive shaft. In other words, all of the mechanisms presented in this section are to control the motion of the rotors (in a dual rotor toroidal engine). It will be seen in the section below that this method of power transmission can be achieved with a wide range of mechanisms. These mechanisms are grouped into geared linkages only, cammed linkages only, and a combination of geared and cammed linkages.

Table 3 - Summary of timing methods of engines with linked power transmission.

Inventor(s)	Year	Reference	Timing Method
Free, P.D.	2001	(36)	Fixed port and spark plug locations. Spark timing not disclosed.

Inventor(s)	Year	Reference	Timing Method
Sakita, M.	1995, 2002, 2010	(65; 66; 67)	Fixed port locations. Spark plugs located within rotating pistons and connected to an ignition source. Spark timing method not disclosed.
Arov, A.	2009	(68)	Fixed port locations with rotary valve to time exhaust and intake. Spark timed by rotation of shaft.
Ball, W.; Rõnnberg, P.	1998	(69)	Fixed port and spark plug locations. Spark timing not disclosed.
Kovalenko, V. I.	2007	(70)	Fixed port and spark plug locations. Spark timing not disclosed.
Morgado, R. G.	2004	(32)	Fixed port and spark plug locations. Spark timing not disclosed.
Silvoza, E.P.	1988	(71)	Fixed valve and spark plug locations. Valves and ignition operated by cams connected to drive shaft.
Cronen, P.J.	1977	(30)	Slide valves and spark plugs fixed on housing. Valves and ignition operated by cams connected to drive shaft.
Stoughton, D.R.	2005	(72)	Fixed port and spark plug locations. Spark timing not disclosed.
Kurisu, M.	2002	(73)	Fixed port and spark plug locations. Spark timing not disclosed.
Richards, R.L.	2002	(74)	Fixed port and spark plug locations. Spark timing not disclosed.
Larrea, C.A.	1977	(75)	Fixed port and spark plug locations. Spark timing not disclosed.
Bergen, H.	1976	(29)	Fixed port and spark plug locations. Spark timed by gear connected to drive shaft.
Stromberg, O.E.E.	1929	(76)	Fixed port and spark plug locations. Spark timed by rotation of shaft.

4.3.2.3.1. Geared Linkages

All of the engines in this section have rotor control with geared linkages. All of the configurations, with the exception of the Wildhaber-Sakita (65; 66) arrangement, have a planetary gear train with some sort of linkage between each of the rotors and the planet gears. An example of this arrangement is seen in Figure 27. Planet gears are equally spaced around a stationary sun gear. Each rotor is connected to the circumference of a planet gear by a connecting rod. The rotors turn the planet gears by pushing the connecting rod. This action forces the planet gears to orbit about the sun gear, which causes the ring gear to rotate the drive shaft (69; 70; 32). These engines are designed such

that each rotor will re-position in the same place every revolution. This allows the use of fixed port locations for intake, exhaust, spark, and injection.

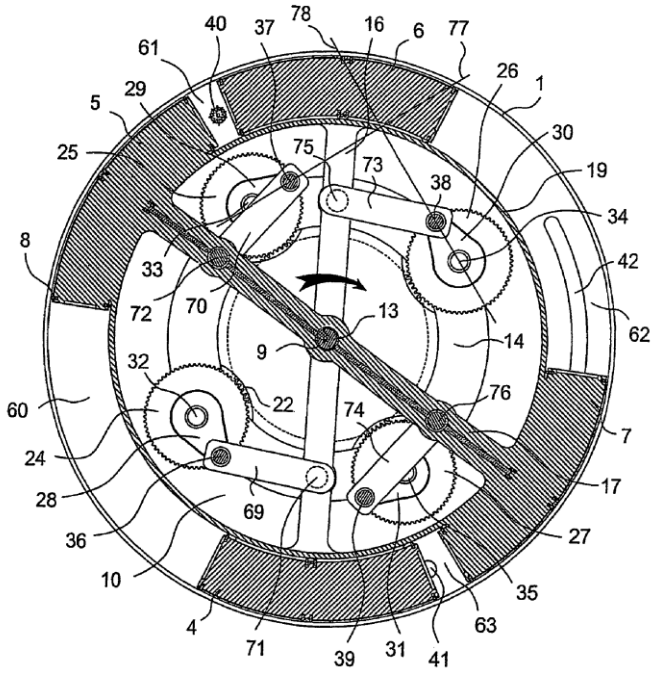

Figure 27 - Example of a toroidal engine with planetary gear train and connecting rods (70).

An alternative to using a planetary gear mechanism with connecting rods is to use non-circular gear meshes. These gear meshes are called Wildhaber-Sakita gears after their inventors (66). Two rotors are connected to two separate concentric shafts. Each shaft drives a gear train which includes a set of Wildhaber-Sakita type 1 and 2 gears. A Wildhaber-Sakita gear set is constructed of a tear shaped (type 1) gear meshed with a heart shaped (type 2) gear as seen in Figure 28. The gears are noncircular, and when meshed, produce a constant output from a non-constant input, or vice-versa. This mechanism is used to transmit the oscillating motion of the rotors to a constant speed drive shaft (66).

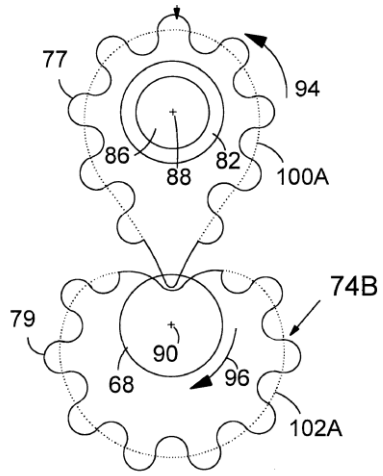

Figure 28 – Wildhaber-Sakita gear mesh (66).

Figure 29 illustrates an application of the use of this type of gear for a toroidal engine. The engine has a shaft connected to each rotor. Each output is connected to a type 1 gear. The gears are offset by half a rotation on each rotor to produce the oscillating motion between the rotors. The type 1 gears mesh with the type two gears, which are mounted on a common shaft. The type 2 gears rotate at a constant speed with the drive shaft. Also included in the gear train, is a differential with the arm connected to the output shaft, and the sun and ring gears independently attached to the output of the rotors. This differential ensures that the sum of the rotational speed of the rotors is equal to the rotational speed of the output shaft. Variances in this design include differences in the specific teeth architecture of the non-circular gears, gear ratios of the differential, and mechanisms to prevent backwards motion of the rotors (65; 66; 67).

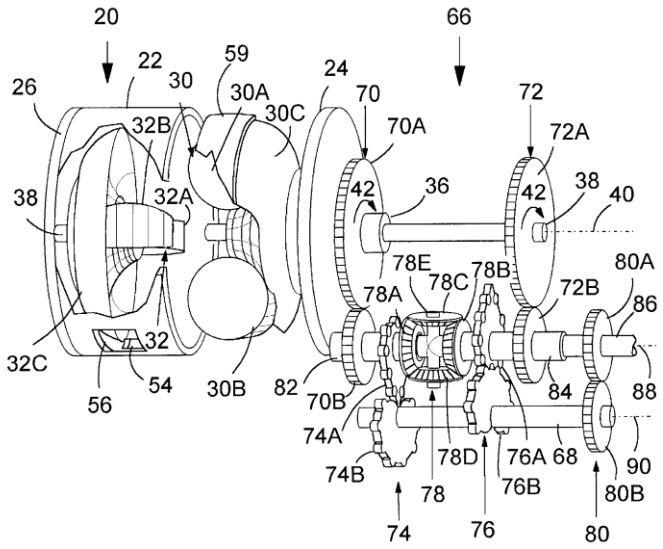

Figure 29 – Application of noncircular gears to transmit power from rotors to a common drive shaft (66).

A recent variation of this design uses a similar gear mechanism to create oscillating motion between the rotors (68). However, the gears are circular, and mounted eccentrically on parallel shafts.

4.3.2.3.2. Cammed Linkages

An alternative to using geared linkages is to use cammed linkages. These mechanisms use linkages with pins that follow a prescribed path by interference with a machined surface (cam). An example of this is seen in Figure 30, where two rotors are rotatable on a common drive shaft, each having two, equally spaced rotor pins protruding from the rotor face, away from the adjacent rotor. Adjacent to each rotor are two additional drive pins positioned in interference with the rotor pins, and fixed to the drive shaft. A bar is connected to each pin such that the center of the bar is rotatable on each pin. The ends of the four bars are linked with revolute joints to form a four-bar mechanism. Rollers are positioned on the corners of the linkage, and the rollers are guided by an external cam ring, as illustrated in Figure 30. The design also incorporates a method for adjusting the angle of each ring cam relative to the engine housing to vary the compression ratio and displacement of the engine (36). Similar designs have been used in earlier engines (71; 30).

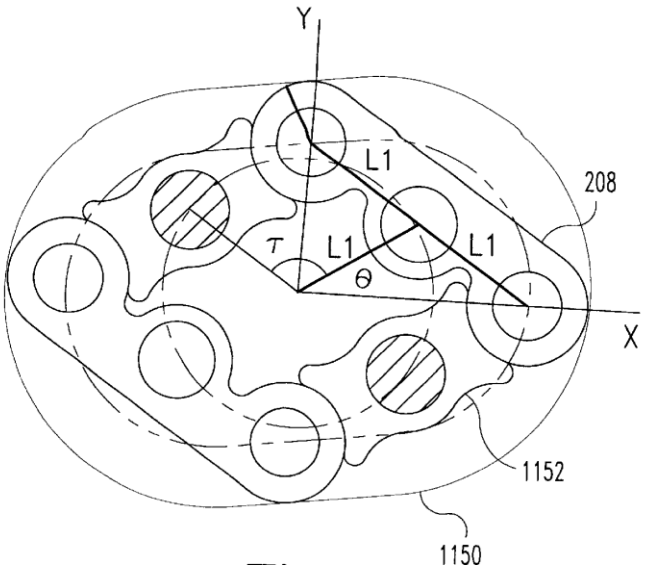

Figure 30 – Example of a four-bar linkage used to control the motion of oscillating rotors (36).

4.3.2.3.3. Combination Cammed and Geared Linkages

The engines shown previous in this section have controlled the rotor motion with either geared or cammed linkages. The engines in this section use a combination of gears and cams to control the motion of the rotors. An example of this is an engine design with a main piston assembly and a following piston assembly Figure 31. The main piston set is coupled to the shaft and the following piston set is free to rotate with respect to the shaft. Two arms are fixed to the shaft and rotate with the main piston assembly. Planet gears are housed on the ends of the arms, which mesh with a stationary ring gear. The ring gears are positioned axially on either side of the rods connecting the following pistons. A pin connects each set of adjacent ring gears, and creates an interference with rods connected to the following piston set. Therefore, the rotational movement of the following pistons is constricted by the pins, which creates an oscillating motion between the main pistons and the following pistons.

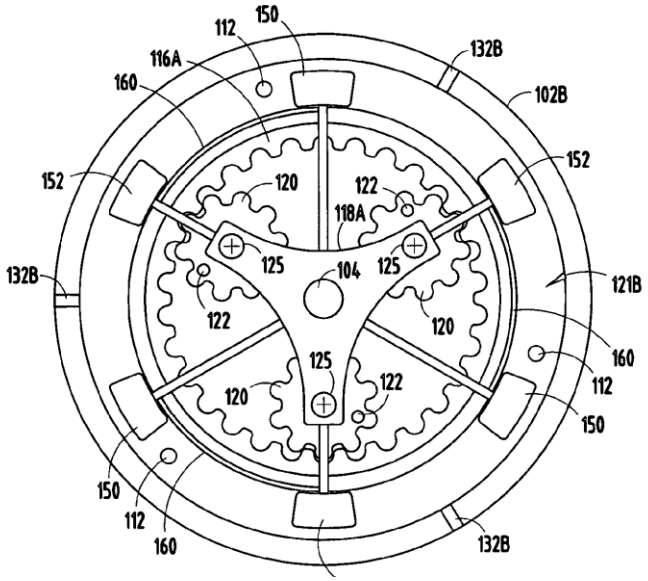

Figure 31 – Example of a toroidal engine with planetary gear train and interference pins (72).

A variation of this type of engine uses a planetary gear system similar to that of (72). The engine uses a slot on the rotor, and pin on the planet gear to control the motion of the rotor with respect to the stationary sun gear, as seen in Figure 32. The engine shown uses square shaped pistons, but the slot mechanism can be applied to a toroidal shaped chamber (73).

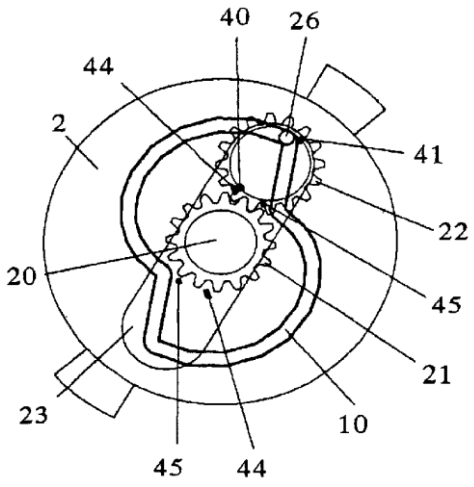

Figure 32 - Example of a toroidal engine with planetary gear train and slot guide (73).

Another variation of this type of engine is an engine with two rotors, and a planetary rotor guide, as shown in Figure 33. The main rotor is coupled to the drive shaft (constant speed), and the following rotor is able to rotate freely about the drive shaft. Each rotor

has a cantilevered pin, which slides in a groove in the planetary rotor guide. The groove is straight, and is centered about axis of the planetary rotor guide. The rotor guide is coupled to a planetary gear, which is rotatable on an arm attached to the drive shaft, and meshes with a stationary ring gear (74). This planetary gear configuration causes the rotor guide to rotate eccentrically about the drive shaft, which varies the arc length between the pins connected to the main and following rotors. Therefore, the following rotor is forced to oscillate with respect to the constant speed main rotor. The gear ratios of the particular design shown are configured such that the pistons will reposition at the same locations every revolution.

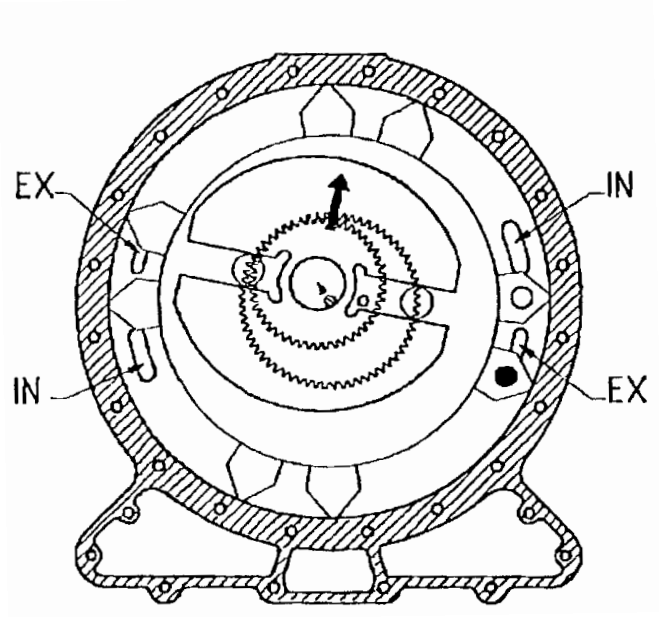

Figure 33 – Example of a variation of a toroidal engine with planetary gear train and slot guide (74).

Earlier versions of this design incorporate linear slots into each of the rotors. An example of this can be seen in Figure 34. Planet gears rotate about an arm connected to the drive shaft, and the planet gears mesh with a stationary sun or ring gear. Pins connected to the circumference of the planetary gears slide within slots located on each rotor. The rotation of the planetary gears around the stationary sun or ring gear creates oscillating motion between the two rotors (77; 78; 79).

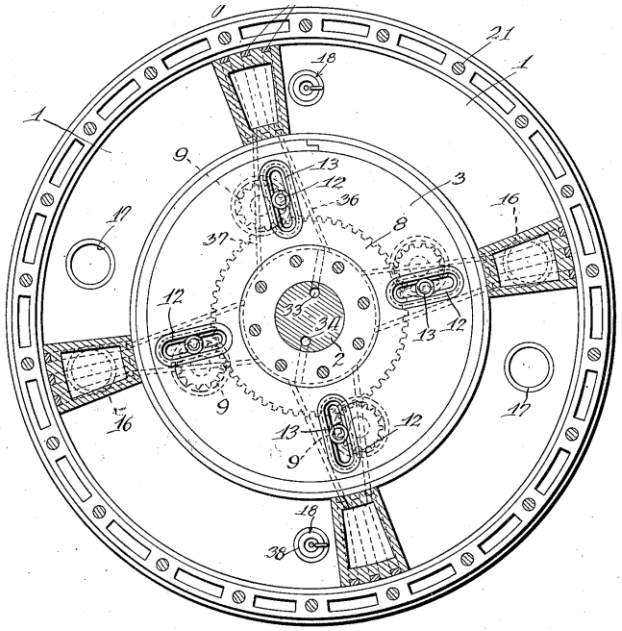

Figure 34 – Example of an early toroidal engine with planetary gear train and slot guide (79).

CHAPTER 5 DEVELOPMENT OF THE NOVEL TOROIDAL MOTOR

The following chapters are focused on the many design pathways and concepts that were considered, developed, and abandoned throughout the motor development process. One of the goals of these chapters, and of this thesis, is to show that this was not a straightforward process.

As described in Chapter 3, the goals of the toroidal motor are to have low-friction sealing, high torque output, and high displacement-to-size and weight ratio. Additionally, component designs were to maintain commercially viable manufacturing requirements. However, the specific metrics of these goals are difficult to realistically define in the early stages of the development of the motor concept, as there are many constraints and design tradeoffs which are widely unknown. Therefore, the primary goal for the development work of this thesis was a proof-of-concept of the toroidal motor. Further goals were to present test results of the motor, and design components with minimal features. Designing components with minimal features provides context for retrospective analysis of the commercial viability of further development of the toroidal motor, which such analysis is not a focus of this thesis.

There are many aspects of the working prototype that are derived from the knowledge obtained from abandoned concepts and design features. Therefore, it is essential to understand the design process in order to understand how to develop and advance the design further. Previous work had demonstrated the desired motion of the rotors with an open-casing prototype, but not with a closed casing (80). Therefore, in the early stages of this project, development was focused on discovering why the closed casing prototype was unable to operate. The hypotheses of the cause of this was hard to define, and it was thought that it could be due to many factors such as the seals between the rotors and the casing, the piston seals, the bearing alignment, port size location and shape, impact mechanism design, or timing of the working fluid. Early work was focused on the design of the rotor seals, and this resulted in no significant progress or improvements, and it was decided to remove these seals from the prototype to determine whether they were critical

to the operation or not. Further, since previous work had demonstrated the operation of the rotors with an open casing, it was thought that the best place to start was to re-create this prototype, and build-on other components to test the effect of including these components on the prototype. Some of the components that were focused on were the timing, bearing arrangement, piston design, and nozzle angles. This allowed the systems such as the bearing arrangement and timing to be developed independently of the other integral components with a closed casing. It was through this process that critical design features such as the piston sealing and casing design were developed. These design features allowed the prototype to operate with a closed casing. Once a closed casing prototype was operable, wear on critical components such as the pistons and impact rings could be observed. Observations such as piston failure or loosening fixtures between components allowed the improvement of components of the prototype to the point where reliable tests could be made, which was a goal of the experimental development.

5.1 Sealing

One of the main advantages of toroidal over traditional Wankel rotary engines is the use of round piston seals. Round seals have an improved pressure and wear distribution, when comparing it to apex seals used in the Wankel. Figure 35 illustrates the geometry of a Wankel engine, and highlights the accelerations experienced by the seal assembly in View A. It can be seen that as the shaft rotates, the angle (lean angle) between the seal and the housing wall varies. Testing on apex seals in traditional rotary engines has shown that chattering and vibration forces occur between the seal and housing at well-defined angular positions of the rotor (24). This force interaction occurs when the angle of the apex seal is at its maximum lean angle (or acute angle), shown in Figure 36, and causes leakage between the chambers of the engine or motor.

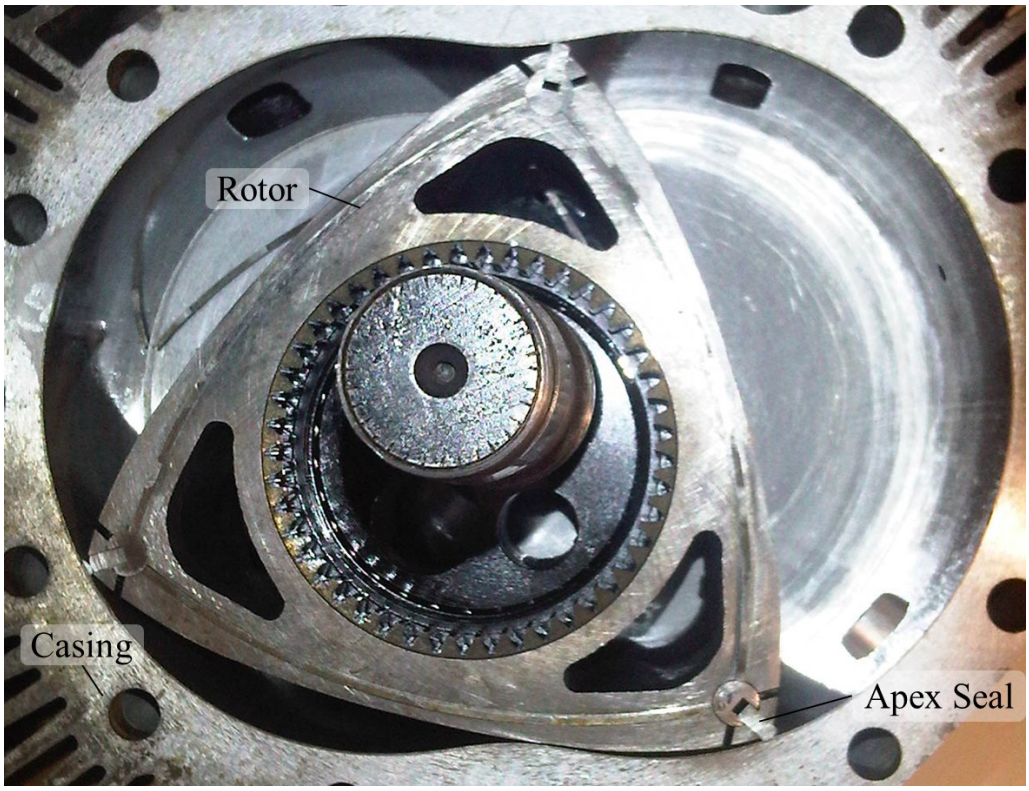

Figure 35 - Wankel engine, illustrating the rotor, casing and apex seals.

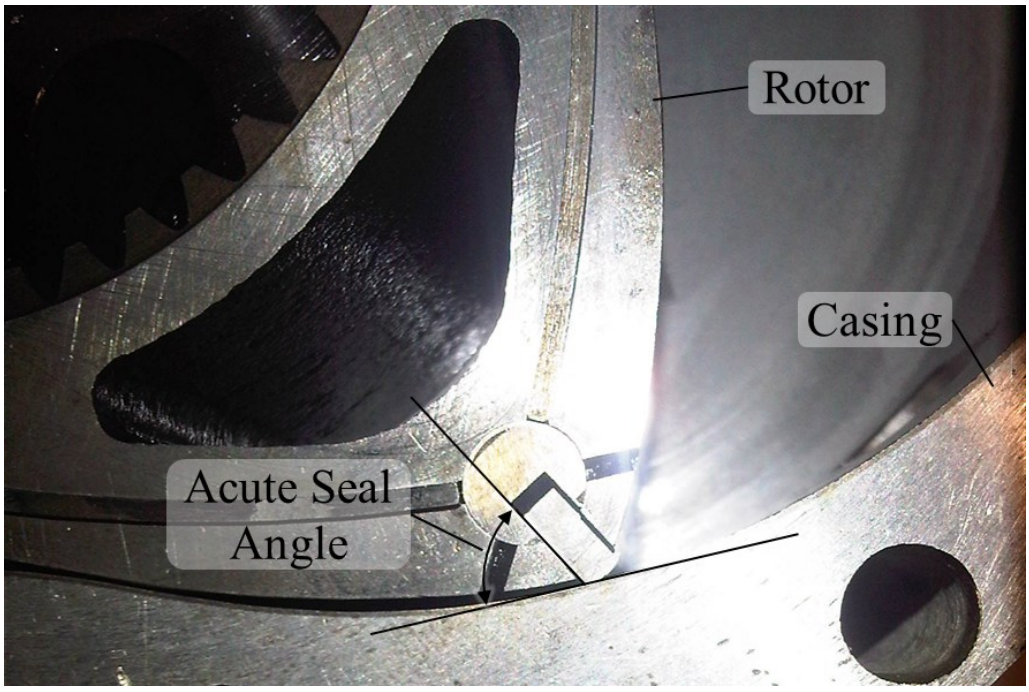

Figure 36 - Wankel engine, illustrating the acute angle between the apex seal and casing.

Round piston seals, or compression rings, are used in conventional reciprocating engines. These seals have proven to be accepted industry wide, and are able to compensate for

radial wear of the piston chamber. Since the cross sectional shape of the toroidal chamber is round, toroidal engines are able to use conventional compression rings. However, toroidal engines have inherent sealing drawbacks. The general engine architecture requires part of the chamber casing to move with each of the piston sets, and part to remain stationary to house intake, exhaust, and injection or ignition ports. Toroidal engine designs have different configurations of this, but all have seams between the stationary and rotating parts. Figure 37 illustrates an example of a toroidal engine with the locations of these seams circled.

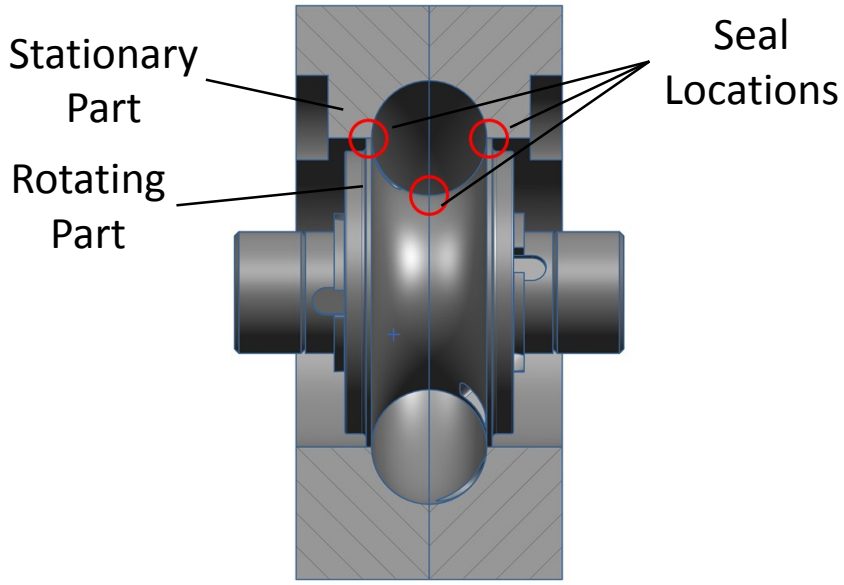

Figure 37 – Cross section identifying areas requiring sealing between rotating and stationary parts.

Sealing these seams prevents air from leaking between the chambers separated by pistons and prevents air from leaking out of the sides of the rotors to the atmosphere. Therefore, for the efficiency of the motor, these seals are very important. However, for the general operation of the motor, it was found that these seals did not play a critical role in the motor being able to operate or not, as early testing demonstrated that theses seals generated too much friction and caused the motor to stall. Further, since a goal of the thesis was to test the motor with minimal components, it was decided to eliminate these seals, and focus on the other components and mechanisms in the motor. Once these components are further developed, the seals can then be developed independent of any of

the other components in the motor. Further, it is expected that the efficiency of the motor will be low without the seals, as there is a considerable amount of leakage around these sealing locations.

5.2 Open Casing Development

An open casing prototype was developed to repeat the open casing testing that had previously been done. Figure 38 illustrates the open casing setup, consisting of two rotors with two pistons attached to each. Two nozzle attachments were located on the periphery of the rotors to control the location and trajectory of the compressed air that was applied to the rotors.

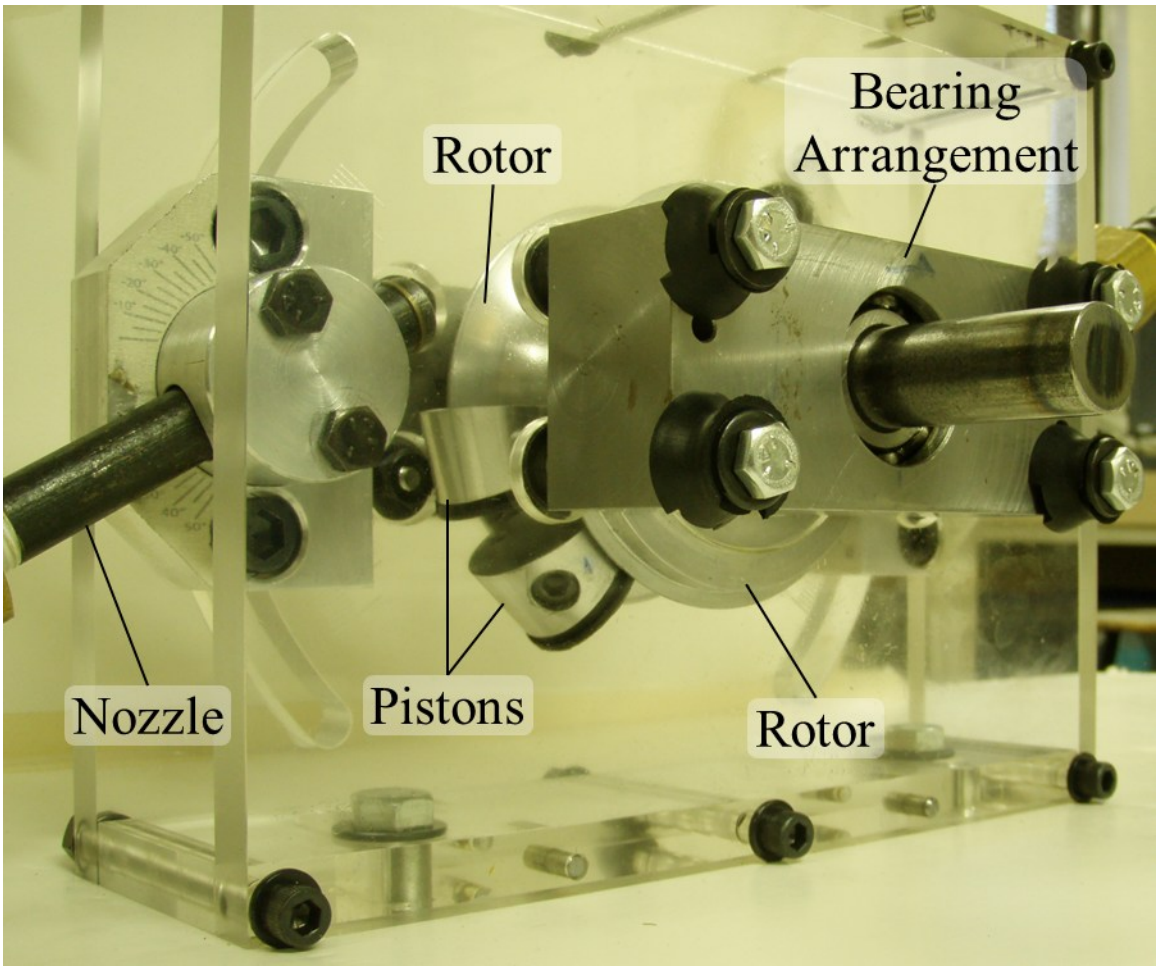

Figure 38 - Open casing test setup.

It was found from early testing that the rotors would not rotate intermittently (or ratchet) as had been previously demonstrated. Rather, the rotors would turn together as a turbine

at constant speed. Also, it was observed that the trajectory (or angle) of the nozzle didn't have influence on the ratcheting; rather only the maximum speed of the rotors. From further development of this setup, it was discovered that a roller mechanism, shown in Figure 39, will cause ratcheting of the rotors without any linkages or gears.

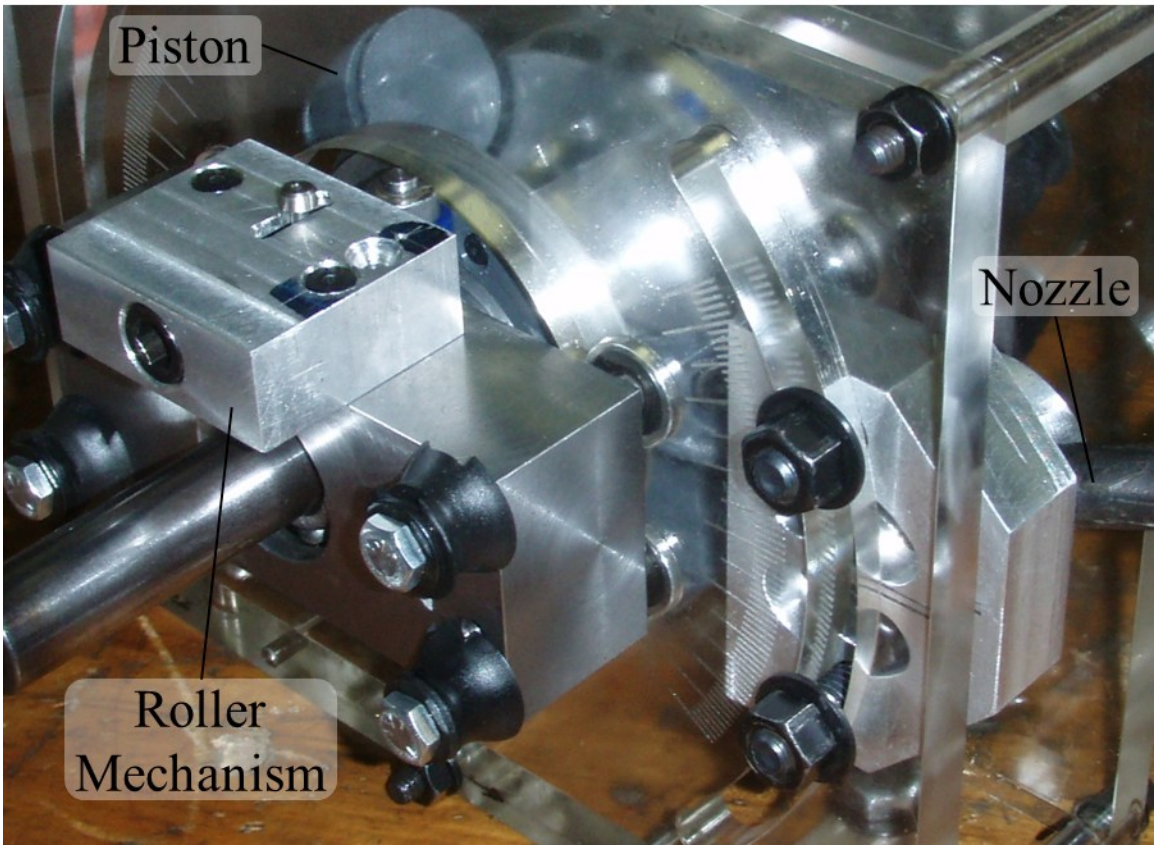

Figure 39 - Open casing test setup with roller mechanism installed.

A roller mechanism is installed adjacent to each of the two rotors. A roller on the mechanism maintains contact with a roller land on each of the respective rotors. A protruding surface on each of the roller lands contacts the roller to temporarily stop each of the rotors at the desired backstopping (stationary) position. Once the first rotor (moving) impacts the second rotor (stationary), the first rotor is forced to stop by the roller mechanism, and the second rotor is forced passed the backstopping position, and begins rotating through the power stroke. Therefore, at any given time, there is one rotor indexing and one rotor backstopping, or the two rotors are in contact and in transition between the two states.

It was found from testing that the roller mechanism successfully controlled the motion of the rotors as desired. This enabled observation of the motion of the rotors with an open casing, and tested the strength of the impact components throughout the transition stage. These two observations were crucial to the development of the motor, and the impact mechanism enabled these observations to be made. However, it was found that there are inherent disadvantages of the roller mechanism to the overall motor performance. In particular, fine adjustment of the springs was required, the rollers created considerable drag on the rotors, the mechanism added vibrations to the motor, and the mechanism increased the overall complexity of the motor. In particular, the springs were adjusted by starting with a soft spring, and increasing the spring stiffness and pre-tensioning incrementally. Experiments were conducted at each stage to observe the effect of the spring adjustments on the operation of the motor. A high speed camera was used to count the number of cycles that the motor ratcheted (rotors alternatively rotating) before either stalling or the rotors rotating together (not alternating). This observation was used to determine the effects of the spring adjustments until eventually the motor ratcheted continuously. This operation allowed experimental testing of the casing and piston seals, and led to the conclusion of the importance of the design of the impact mechanism between the rotors, which development was focused on, as described in Chapter 6.

CHAPTER 6 IMPACT RING DESIGN & FEM MODELING

6.1 Introduction

The toroidal motor design consists of two intermittently rotating bodies (rotors), which are not mechanically linked. The bodies transmit rotational energy between one-another during the transition between the engine cycles through an impact mechanism. Each of the bodies is constructed with a rotor, pistons, and impact ring. The rotor and pistons are the bulk of the mass and are currently mostly constructed of Aluminum 6061-T6, as this was the material chosen by previous work (80), due to the high strength-to-weight ratio, and good corrosion resistance when exposed to moisture, when compared to low-carbon steel. Further, since one of the goals of the experimental work is to improve the power density of the motor, lighter weight materials were chosen. The impact ring is fastened to the rotor with a set of screws, and the two impact rings (one attached to each of the rotors) are the contacting components during impact.

Currently, the mechanics occurring between the two bodies are widely unknown. In particular, the stresses in the impact ring and the energy transfer between the two bodies are unknown. The objective of this chapter is to develop a finite element (FE) model to study the stresses and energy transfer associated with the collision of two rotationally impacting bodies. The model was built progressively to allow comparison of results between incremental steps. Further, this model was built to determine if improvements of the geometry would reduce the stresses experienced by the impact rings, and evaluate if common materials could be selected to withstand the predicted stresses.

6.2 Model Setup

As introduced above, an objective of this study is to build the model in piecewise steps. This allows the results to be compared and conclusions to be drawn as the model progresses to a more advanced state. This section discusses the geometrical simplifications to mesh the parts, and the process used to advance from a simple static

model, to a higher-level dynamic model. The model was set up using the LS-DYNA Hydracode and the details of the code (model input parameters) for the dynamic model is included in Appendix C.

6.2.1 Modeling Process

A flow chart illustrating the process used for this study can be seen in Figure 40. A simplified static model was used for the convergence study. The results of this gave a starting point for the mesh to use in the dynamic model. However, this did not necessarily ensure that the dynamic model had numerically converged with this element size. Therefore, it is necessary to compare the mesh used for the dynamic model, to a finer mesh once a stable model had been completed. It is advantageous to use a coarse mesh to develop the model in order to minimize computational time for iterations in the process. The results are then tested with a finer mesh that takes longer to compute to ensure the model has consistent results.

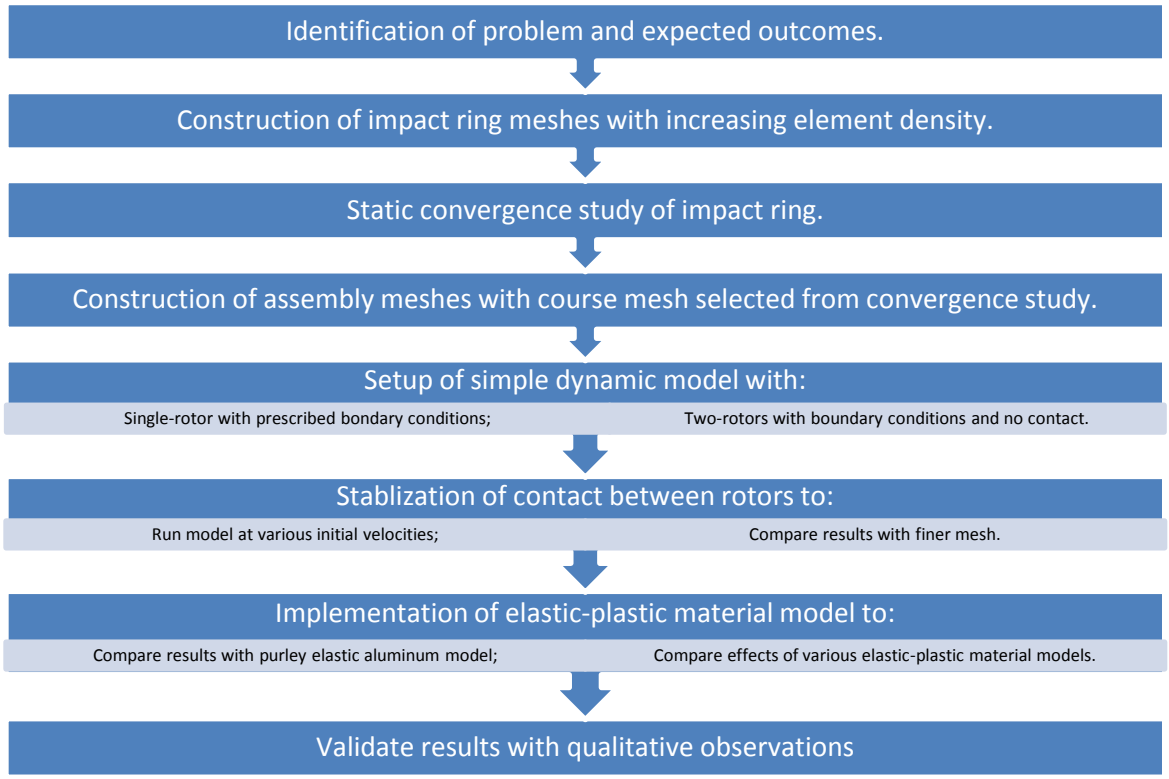

Figure 40 - Illustration of piecewise modeling process.

6.2.2 Geometric Simplifications and Physical Properties

List and describe the implications of geometrical simplifications and compare the modeled volume, mass, and mass moment of inertia to actual values in the parts.

In order to mesh the parts of the model consistently, some geometrical simplifications were made. The parts being studied are constructed in imperial (inch) units, and contain detailed features such as fillets, countersunk screw holes, and keyways. All of these parts are converted to metric (m) units for continuity in modeling, and detail features are removed for simpler meshing. The following sections illustrate the geometrical changes made for each part, and discuss the implications of these changes to the model.

6.2.2.1 Impact Ring

The figures below illustrate the geometrical simplifications made to the impact ring. The fillets on the pad of the ring are removed, and the swept angle of the ring is reduced by 9% (see Appendix A for supplementary calculations). The calculated stress in the model will be more than in reality because of sharper geometry, and smaller areas. Therefore, these are conservative simplifications.

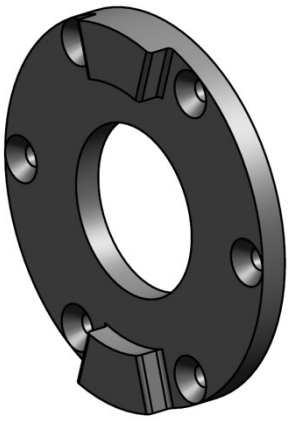

Figure 41 - Illustration of actual geometry of impact ring.

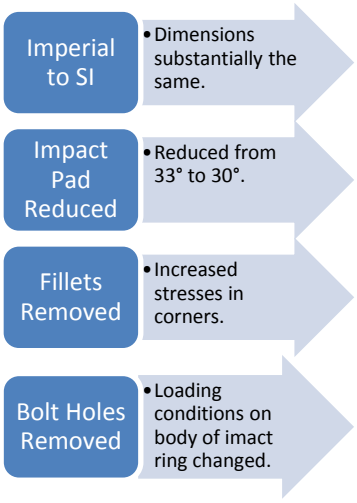

Figure 42 - List of geometric simplifications, and implications to the model.

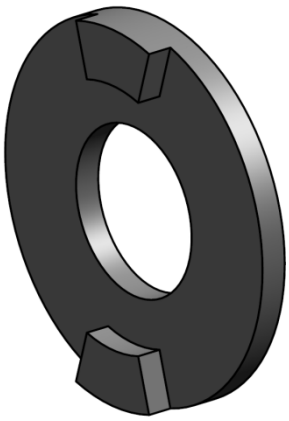

Figure 43 - Illustration of impact ring geometry used in the model.

It is seen that the bolts between the impact ring and the rotors have been removed from the model. This causes differences between the loading simulated in the model, and those actually experienced by the impact ring. The tensioned bolts will cause slight deformation and stresses in the body of the impact ring. However, the effect of bolt tension on the impact ring is not the focus of this study. Additionally, it is assumed that the bolt system is designed such that the majority of the shear-stress between the rotor and impact ring is transferred through the static friction between the two parts, which is caused by the tension in the bolts. Therefore, it is estimated that the removal of the bolt system does not significantly change the calculated stresses in the pad of the impact ring, or affect the simulated energy transfer between the impact ring and rotor.

6.2.2.2 Rotor

The figures below illustrate the geometrical simplifications made to the rotor. It is important to note that the functions of the rotor and impact ring in the model are not the same. The impact ring is required to evaluate stresses and energy transfer with a reasonable degree of accuracy during impact in the dynamic simulation. Conversely, the rotor is only required to simulate the inertia in the system. Therefore, the rotor's geometric simplifications are to reduce the number of elements, in order to minimize computational time.

Figure 44 – Illustration of

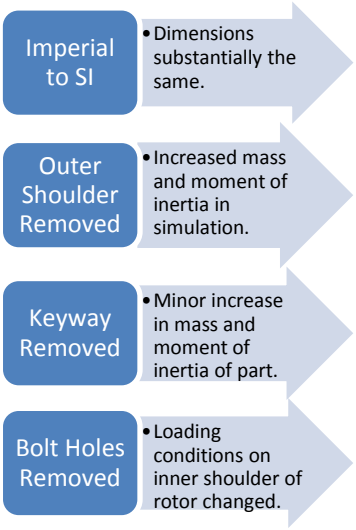

Figure 45 - List of geometric simplifications, and

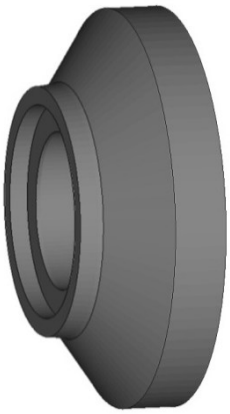

Figure 46 – Illustration of rotor geometry used in the

actual geometry of the rotor. implications to the model. model.

The features removed to reduce the number of elements required to mesh the rotor are the outer shoulders and keyways. Removal of these features has no direct effect to the stress transferred between the rotor and impact ring. However, removing these features increases the volume, mass, and inertia of the rotor. The volume was increased by 30% and the radius of gyration was increased by 6%. The focus of this model is to evaluate the stress distribution in the impact ring, and observe the dynamics of the collision between the two assemblies. Since the rotors are symmetric, the inertial effects are equal for each body. Therefore, variation from the actual volume of the rotor should have minimal effects on the qualitative results desired. However, this limits the possibility of verifying the dynamics of the collision experimentally. In order for this to be done, among other things, more accurate rotor geometry would be required. Furthermore, although not included in this study, it may be desirable to evaluate the effects of modifying the distribution of mass (inertia) of the rotor on the dynamics of the collision between the two assemblies.

6.3 Static Convergence Study

As described above, a static convergence study was conducted to establish an element size to use with dynamic modeling. This section describes the finite element model studied, and the results gained from it.

6.3.1 Discretization

The impact ring was discretized to contain an equal number of elements around the radius of the ring throughout the part. This gives an even distribution of elements throughout the part. However, the size of the elements varies depending on the radius from the center of the part. Generally, the meshes are formed such that the elements on the inner and outer surfaces of the ring are cubic, and the elements in between are generally cubic. An example of this can be seen in Figure 47 below.

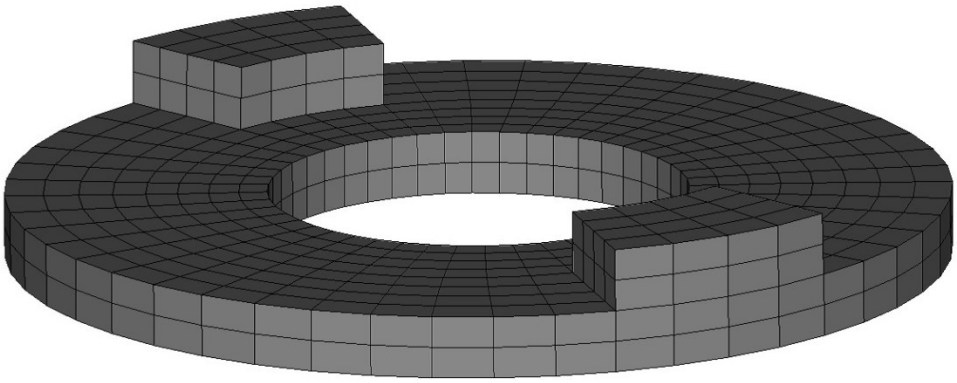

Figure 47 - Example of impact ring element distribution.

A total of six (6) meshes were used in the static convergence study. Table 4 lists the angle between elements (i.e. angle displaced by each element) and total number of elements in each mesh. It can be seen that as the mesh number increases, the element density increases. Generally, each mesh is a derivative of the previous mesh by dividing each element into 8 elements. However, mesh number three (3) was adjusted in order to keep the element biasing consistent throughout each mesh, as described above.

Table 4 - List of impact ring meshes used in convergence study.

Mesh No.	Angle between Elements	No. of Elements
1	15°	104
2	7.5°	832
3	3.75°	4,992
4	1.875°	39,936
5	0.9375°	319,488
6	0.46875°	2,555,904

6.3.2 Boundary Conditions

A simple loading scenario was applied to the impact ring for the static convergence study. Figure 48 illustrates the loads and boundary conditions applied in each of the models. In the each of the models, a 20 kN force is applied to each of the pads of the impact ring, as seen in the figure. The loads are applied perpendicular to the face of the impact ring, and are distributed evenly across all the nodes on the face. In addition, all the nodes on the back face of the rotor were constrained in all directions.

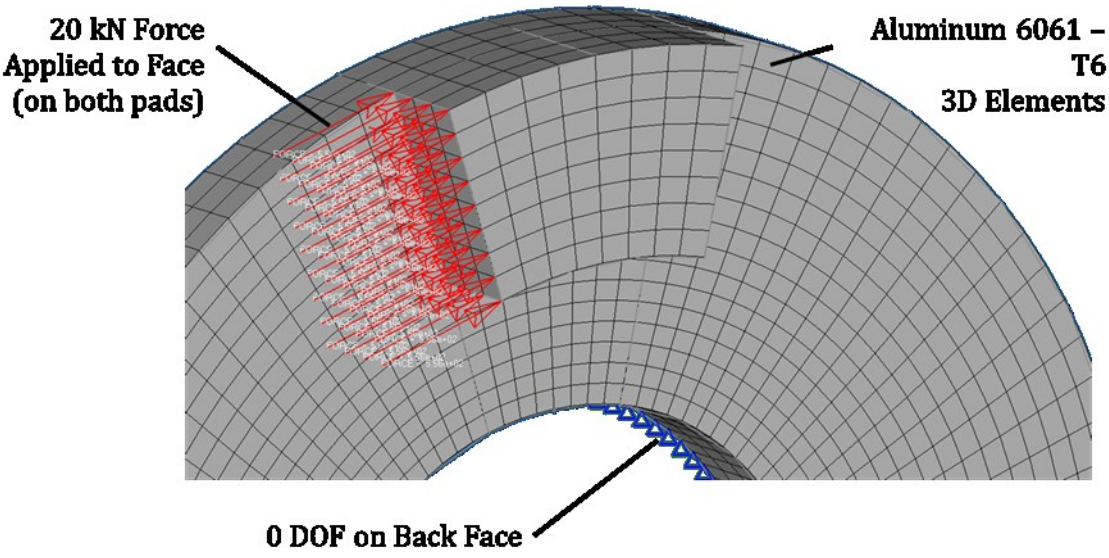

Figure 48 - Illustration of boundary conditions imposed in static model.

The material used in the model was Aluminum 6061-T6. The parameters for this material can be seen in Appendix A2.

6.3.3 Results

In order to provide a consistent comparison for the convergence study, the location must remain consistent for each mesh. This study evaluates the convergence of the displacement of the node at the center of interface between the body and the pad of the impact ring, and the stress in the element adjacent to this node. Figure 49 illustrates an example of the location of this node and element in one of the meshes used for the convergence study.

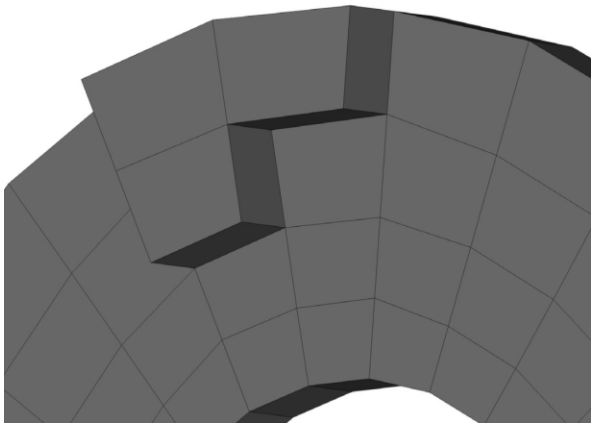

Figure 49 - Illustration of node and element chosen for convergence study.

Figure 50 and Figure 51 below show the element stress and node displacements of the meshes modeled. It is seen that the stress and displacement converge with reasonable tolerance after mesh number two (2). It should be noted that since a considerable force was applied to the model, the element stresses are beyond the maximum yield strength of the material. However, since the goal of this study is to gain understanding of the numerical convergence of the model and element sizes, the magnitude of the stresses are not pertinent.

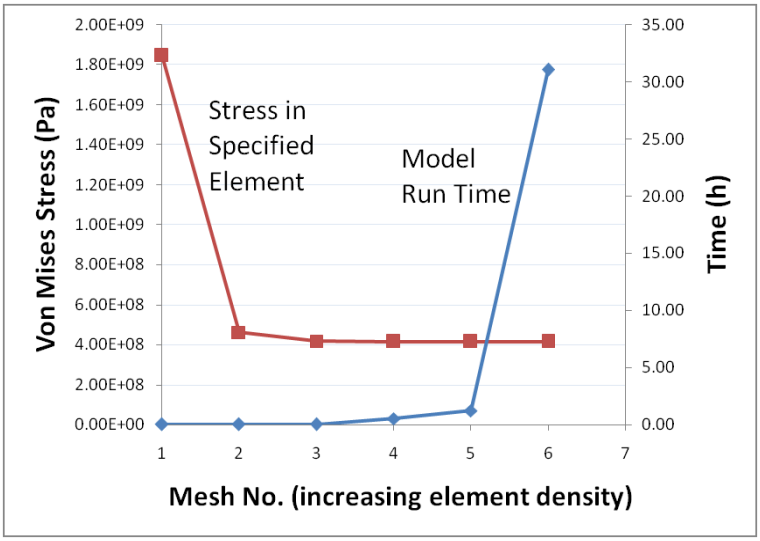

Figure 50 - Stress convergence data.

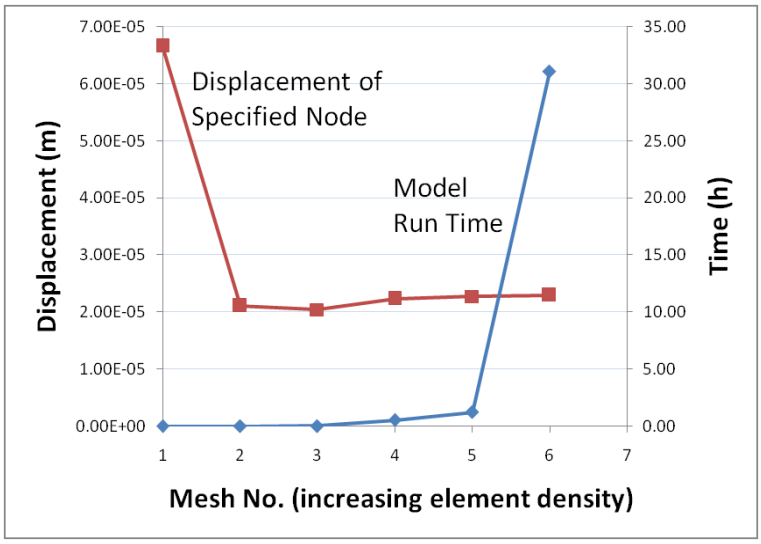

Figure 51 - Displacement convergence data.

It is also seen that the computational time of the models increases considerably with the finer meshes (Numbers 5 and 6). Since the chosen mesh is to be used in a dynamic model with larger parts, the computational time is considered an important factor when selecting the mesh to use in further models.

6.3.4 Conclusion

From the results presented in the previous section, it is seen that the impact ring static loading converges within reasonable tolerances from mesh number two (2) onwards. However, since the convergence study is not in a dynamic model, a conservative selection should be made. Therefore, mesh number three (3) is chosen to use in the dynamic model. Also, in order to verify that changing from a static model to a dynamic model does not have unforeseen effects on the numerical calculations of the model, the results of a simple dynamic model with mesh number four (3) shall be compared to the results of the same model with mesh number four (4).

6.4 Dynamic Modeling Setup

An outline of the modeling process used can be seen in Figure 40, in Section 6.2.1. In general, the mesh selected for the impact ring is used to build the mesh of the rotor. This mesh is then brought into LS-Dyna, and the boundary conditions and initial velocity of the body are imposed. This model forms the master rotor in the following models, as has

the driving conditions and energy of the model. A second mesh is then formed by positioning an additional rotor and impact ring into the assembly. These parts form the slave rotor, as this body is driven by motion of the master rotor. Contact conditions are then imposed between the two bodies, and the initial velocity in the system is reduced until the contact interference is stabilized.

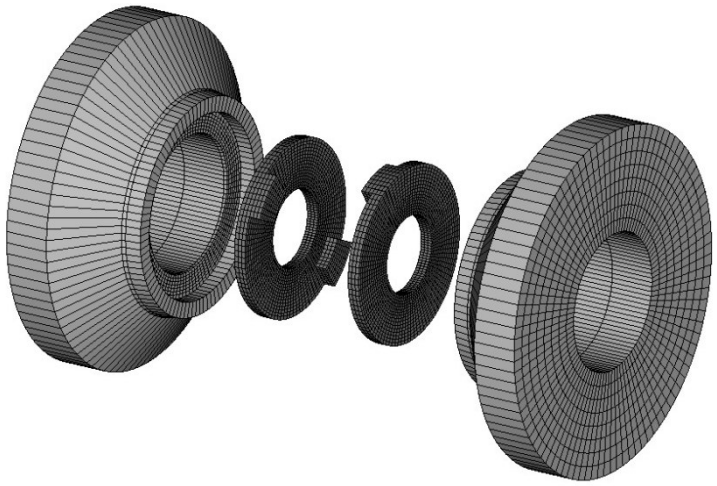

Figure 52 - Exploded view of assembly used for dynamic modeling.

6.4.1 Boundary Conditions

The front and back faces of the rotor are constrained to have no translational movement in the y-axis (along the rotation axis). This is to simulate the constraints imposed by the thrust bearings used in the assembly. Note that it is sufficient to constrain only the back face of the rotor, but the front face of the rotor is constrained to prevent undesired contact between the two front faces of the rotors.

The initial velocity of the master rotor is set by specifying a boundary prescribed motion in the x-z plane. This specifies the rotational velocity of the desired nodes in radians per second (rad/s). This velocity was applied to all the nodes of the master rotor and impact ring.

To ensure that the units are specified correctly and the initial kinetic energy of the system is simulated correctly, an elementary validation is required. This was done by comparing the calculated energy from the geometry used to mesh the rotor, to the energy calculated in the system. It is seen that the kinetic energy of the aluminum model at 250 rad/s is 8.33

Joules. This compares to a calculated value of 7.76 Joules, which is a 7.5% error. Although the values are not exact, they are within a reasonable degree of accuracy. The primary source of the error is likely due to how the toroidal fillet is meshed. The volume used for the energy calculation included the toroidal fillet (round), and because the fillet was meshed with a single element, there is extra volume added to the rotor in the model. Therefore, it can be said that the units used in the model, and the resulting initial energy conforms to what is expected analytically.

6.4.2 Contact Conditions

The dynamic model results are based on the contact conditions between the two bodies. Therefore, at the early stages of development it is important to verify that the contact between the two bodies is stable throughout the simulation. The contact conditions were stabilized by observing the model results, and making appropriate changes to the model to eliminate errors. It was seen in the early stages of the dynamic model that the contact was not operating correctly. The contacting faces of the impact rings were deforming in obscure patters (i.e. not as a solid surface), and the model would eventually drop the surface contact condition. Figure 53 illustrates an example of incorrect contact conditions between the two bodies.

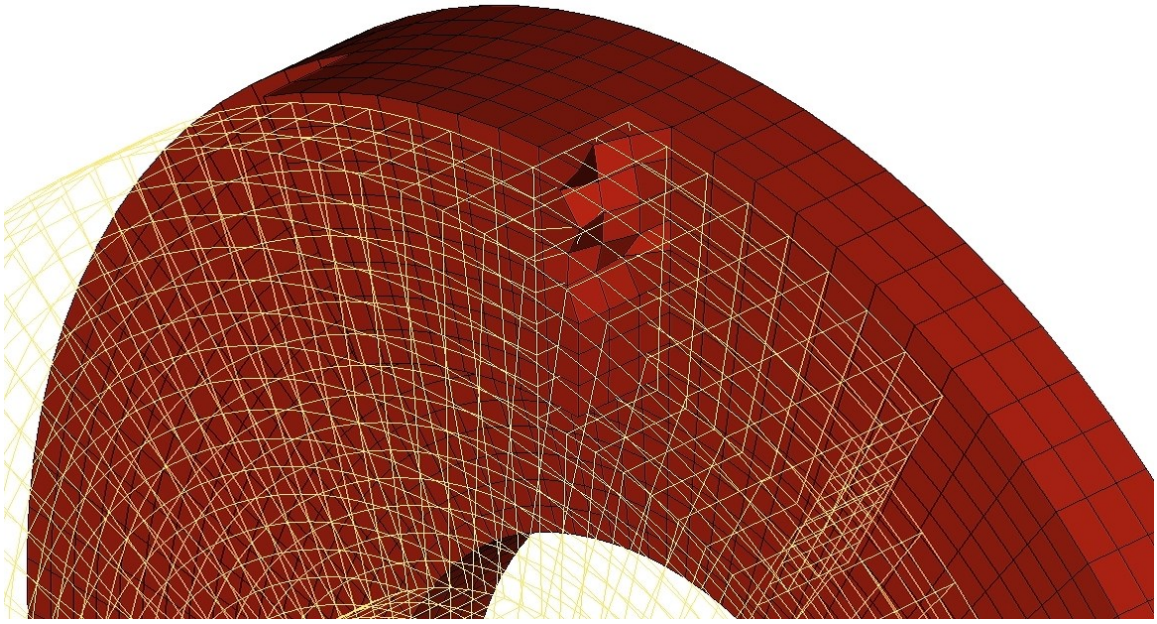

Figure 53 - Illustration of instable contact in the dynamic model.

It is seen that the contacting surface of the master impact ring (shown as solid) implodes, and breaks through the surface of the opposite impact ring (shown as wireframe). This is a clear illustration of unstable contact conditions, as the surfaces are deforming irregularly. The first modification is that the nodes between the contacting surfaces were offset by ¼ of an element depth along the rotational axis. This caused the nodes to align with a surface, rather than an opposing node. The second modification is that the initial speed of the master rotor was reduced. The dynamics of the model are evaluated at incremental time steps, and the time step is based on the speed of sound through the elements, which is based on the size and material stiffness (81). If the initial velocity of the master rotor is too high relative to the time step, the surface of the impact ring will move past the point of contact before the model can calculate the resulting deformation in the impact rings. Therefore, the surface contact condition will be lost by the model, and serious errors occur. It was found that reducing the initial rotational velocity to 250 rad/s stabilized the contact condition in the model, and an example of this can be seen in Figure 54.

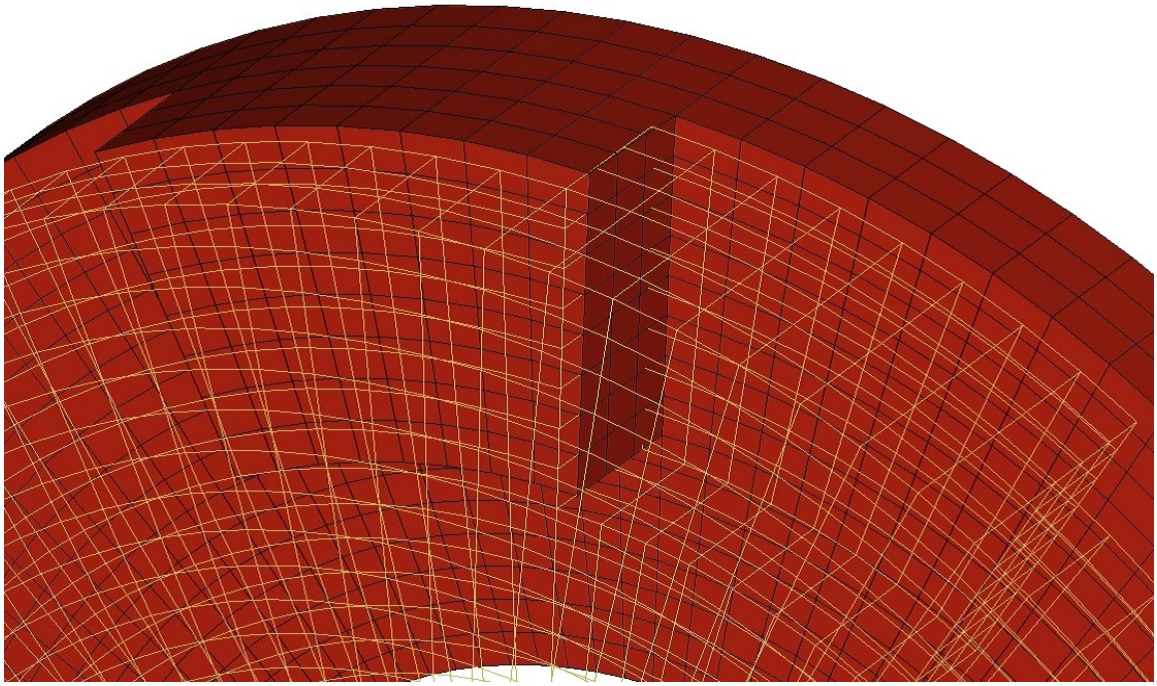

Figure 54 - Illustration of stable contact in the dynamic model.

6.4.3 Material Models

Two material models are used in this study. The first is a simple purely elastic aluminum model. This was used to verify that the model is operating correctly, in that all the initial kinetic energy in the system should result in a distribution of kinetic energy after the collision between the two bodies.

The second material model used in this study is an elastic-plastic model presented by Johnson and Cook (82). The model is established for high-velocity impact computational material models. The model uses a strain-rate relationship which gives more accurate material properties for high-velocity impact computations. It is noted in the paper that other material models may give more accurate material characteristics. However, since this study is a high-velocity impact model, it was seen that this is an adequate material model to compare the results of a purely elastic model. Four materials are used in the study: 2024-T351 Aluminum, 7039 Aluminum, 1006 Steel, 4340 Steel, and S-7 Tool Steel. A list of the exact properties of these materials can be seen in Appendix A3.

6.5 Dynamic Modeling Results

6.5.1 Elastic Material Model

As discussed in Section 6.4, the goal of this model is to test the stability of the boundary conditions, materials, and contact conditions in order to evaluate more advanced material models. The following section discusses the results of the dynamic model with the elastic material model applied.

6.5.1.1 Model Energy

The primary observation and validation of this model is from the energies in the system throughout the collision of the two rotors. By analyzing the relative kinetic energy of the rotors and internal energy of the impact rings, conclusions can be drawn from the model. Figure 55 shows the energies in the system as the collision occurs.

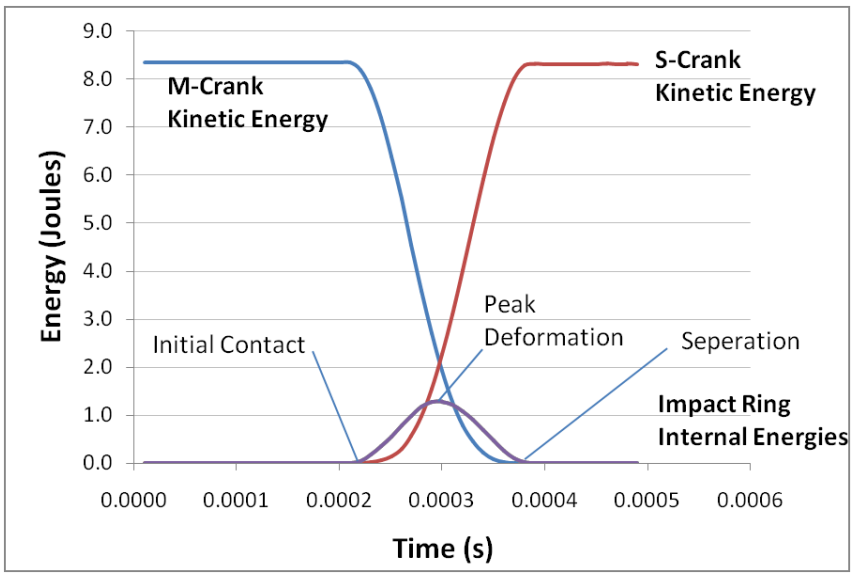

Figure 55 - Elastic dynamic model system energies.

It can be seen that the master rotor (M-Crank) contains all the energy in the system before contact. The initial contact occurs after 0.0002 s, and it can be seen that the kinetic energy in the master rotor begins to decline, the internal energies in the impact rings begins to increase, and the kinetic energy in the slave rotor (S-Crank) begins to increase. At approximately 0.0003 seconds, the impact ring reaches the peak internal energy (deformation), and springs back to the original shape.

In general, it is seen that all the energy is transferred from the master rotor to the slave rotor through the impact ring. However, it should be noted that not all the energy is transferred through deformation of the impact ring; rather, the deformation of the impact ring absorbs some of the shock loading between the rotors. Therefore, in order for these results to be considered an accurate representation of the actual mechanics, higher level material models are required.

6.5.1.2 Course and Fine Mesh Comparison

As discussed in Section 6.3, there are uncertainties in the accuracy of the static convergence study, when applied to a dynamic model. The object of this comparison is to compare the results of the chosen mesh for dynamic modeling to a finer mesh with the dynamic model. A comparison of the model energies, as seen in the previous section, can

be seen in Figure 56. The results from the fine mesh are shifted on the graph in order to view the two results separately.

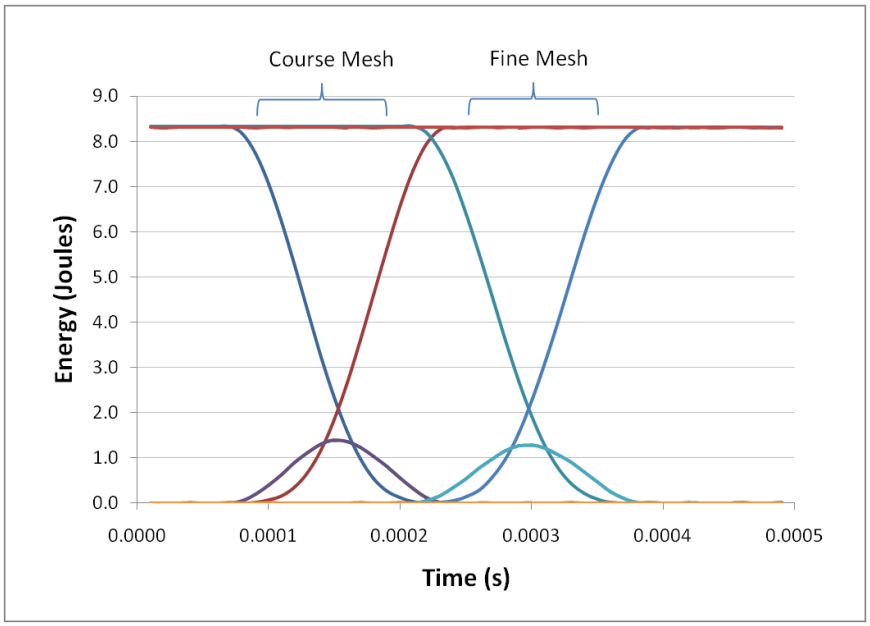

Figure 56 - Comparison of model system energies between course and fine mesh in elastic model.

It can be seen that there are no major differences in the dynamics of the two meshes with this model. There is a slight reduction of the peak impact ring internal energy, but the values are within reasonable accuracy. Therefore, it can be said that any uncertainties of applying the static convergence study to the dynamic model have been eliminated, and the dynamic model is numerically stable with the current mesh (mesh number 3).

6.5.1.3 Varying Speeds

In order to gain some elementary understanding of the relationship between the initial speed of the master rotor and the dynamics of the impact, the elastic model was tested at incremental speeds decreasing from 250 rad/s. In particular, the peak internal energy of the impact ring and the duration were plotted. Figure 57 illustrates the results of these tests.

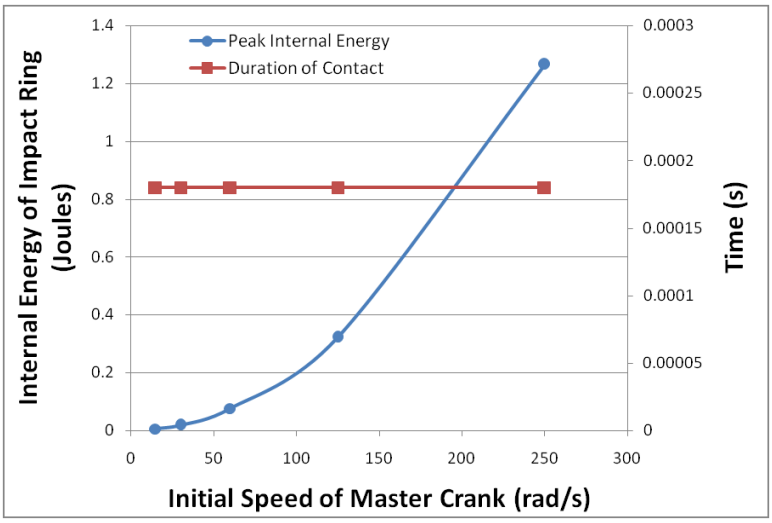

Figure 57 - Internal energy of impact ring and duration of contact as a function of initial velocity with an elastic material model.

It is seen that the internal energy of the impact ring increases as the initial velocity (energy) in the system increases. However, the duration of contact remains the same, independent of the initial velocity of the system. From these results, it is unclear whether this model accurately predicts this relationship, but comparison to the results of the elastic-plastic material model should give more insight to the accuracy of these results.

6.5.1.4 Impact Ring Stress

In order to gain understanding of the accuracy of the elastic model, it is necessary to evaluate the stresses calculated in the impact ring. Figure 58 shows the stress distribution in the impact ring at peak deformation.

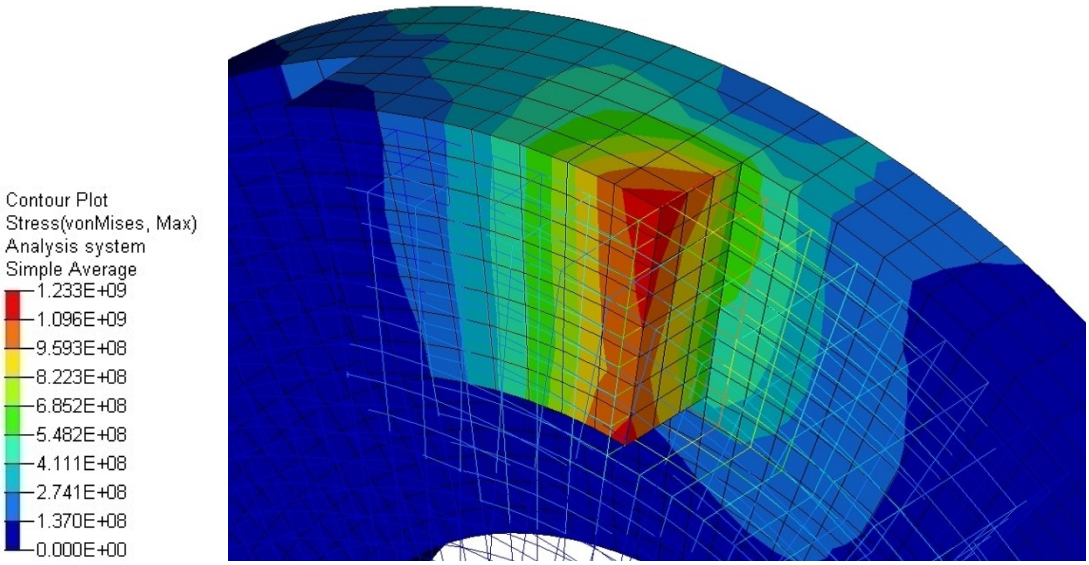

Figure 58 - vonMises stress plot of impact ring at peak deformation in elastic model at 250 rad/s (stresses in Pa).

It is seen that the maximum stresses occur at the outer edges of the pad of the impact ring, and the magnitude of these stresses are approximately 1.2 GPa. Since the yield stress of aluminum is approximately 207 MPa, it is clear that plastic deformation would occur at this velocity. Therefore, an elastic-plastic model is required.

This purely elastic model is an important step to developing a more complex elastic-plastic model. In particular, the pure elastic model is an ideal case of the system. Therefore, it is expected that all the energy in the system is conserved, and this allows the stability of the model to be validated, which is an important observation for developing higher level models.

6.5.2 Elastic-Plastic Material Model

6.5.2.1 Comparison of Pure Elastic and Elastic-Plastic

The following section Illustrates and discusses the differences in results between the pure elastic and elastic-plastic models. Also included, is a comparison of varying the speed of both material models.

6.5.2.2 Model Energy

A major objective of this study is to establish the general effects of more advanced material models in this system. Figure 59 demonstrates the variation of the energies in the material models of the system.

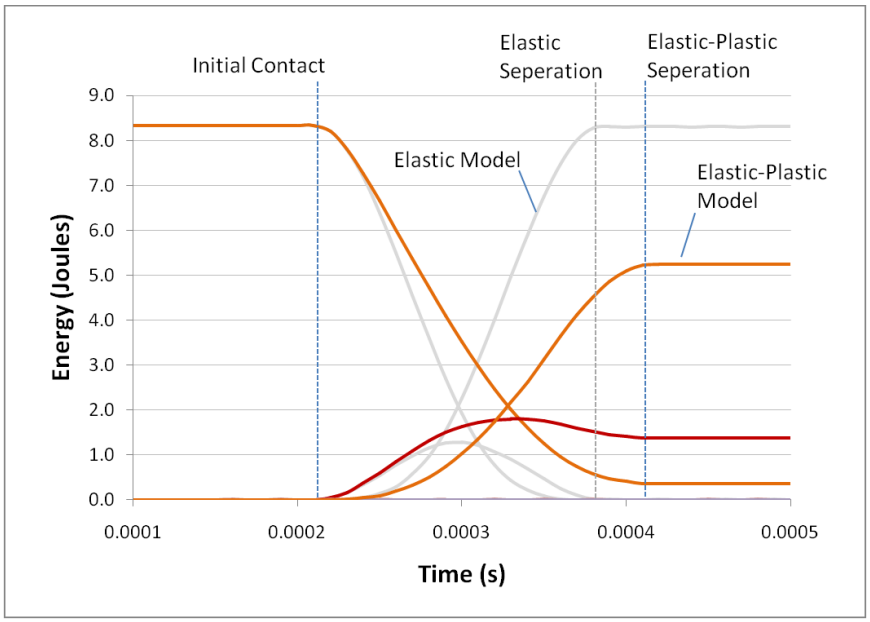

Figure 59 - Comparison of elastic and elastic-plastic system energies at 250 rad/s.

It can be seen that the elastic-plastic material model clearly changes the dynamic results of the simulation. In particular, the duration of contact is increased and energy is permanently absorbed by the impact ring, i.e. plastic deformation. When referring to the discussion in Section 6.5.1.4, plastic deformation is expected at this initial velocity. In addition, the peak internal energy in the impact ring is larger in the elastic-plastic model than the values seen in the elastic model.

6.5.2.3 Varying Speed

As discussed in the elastic model results, varying the initial velocity of the system affects the peak internal energy absorbed by the impact ring. In addition, it was seen that with the elastic model, the duration of contact was independent of the initial velocity of the system. Figure 40 shows the results of varying the speed on the peak internal energy in the system with an elastic-plastic model.

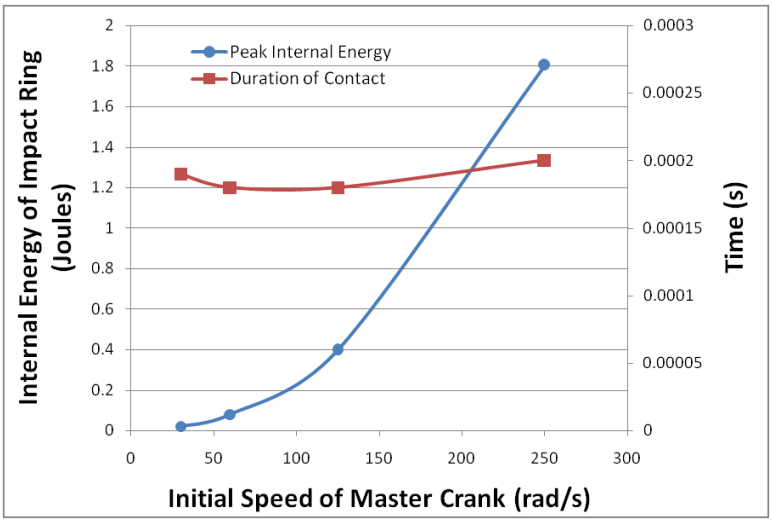

Figure 60 - Internal energy of impact ring and duration of contact as a function of initial velocity with an elastic-plastic material model.

It is seen that the results are similar to the elastic model. However, there is slightly more variation in the contact time of the two bodies. From both sets of results, it can be seen that there is consistency that the duration of contact is independent of the initial velocity of the master rotor. However, this does not verify that there is actual correlation to actual results. Therefore, further investigation is required and the only way to confirm this hypothesis is with experimental validation.

6.5.2.4 Impact Ring Stress

To further study the differences between the elastic and elastic-plastic models, the stress distribution in the impact ring is studied. Figure 61 illustrates the stress distribution of the elastic-plastic model at 250 rad/s.

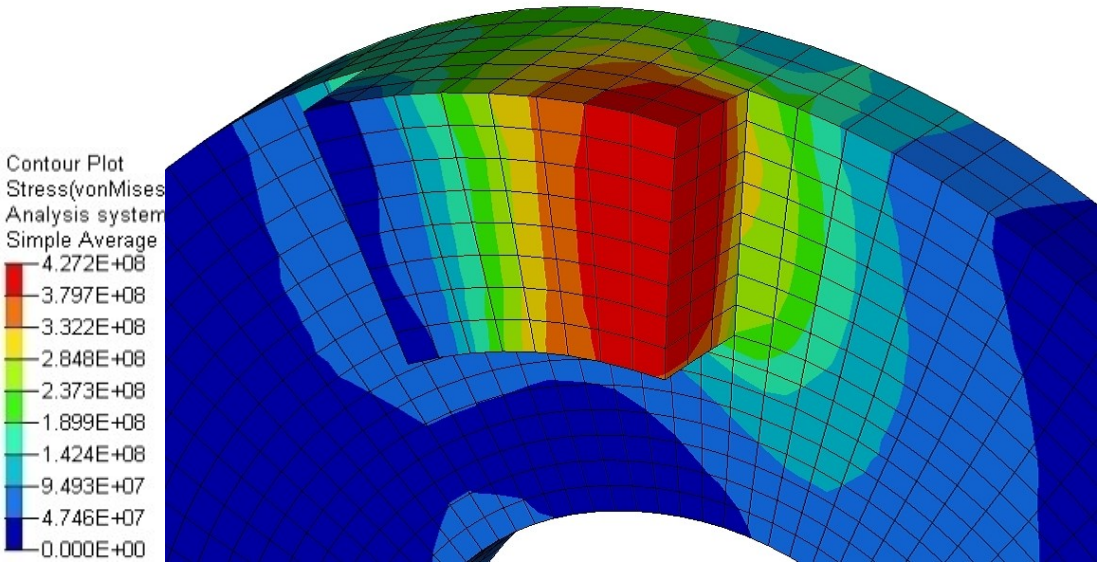

Figure 61 - VonMises stress plot of impact ring at peak deformation in elastic-plastic model at 250 rad/s (stresses in Pa).

It is seen that the maximum stresses calculated in this model are an order of magnitude less than that of the elastic model. In addition, it is seen that the maximum stress is distributed across a larger area in the elastic-plastic model. This is due to the effects of the plastic strain in the model, as the material model limits the stress by permanently deforming the material. Figure 62 illustrates the plastic strain experienced by the impact ring in this model.

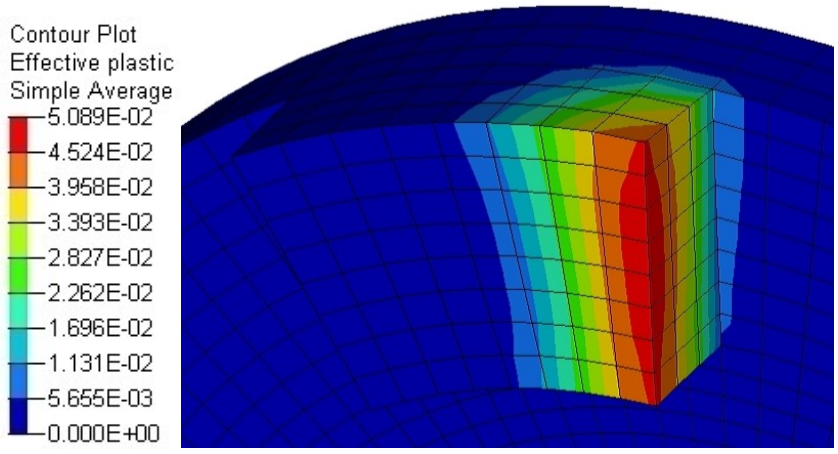

Figure 62 - Effective plastic strain of impact ring after contact in elastic-plastic model at 250 rad/s (strain in mm/mm).

It is seen that the face of the impact ring permanently deforms during the impact collision. The maximum strain is seen at the edge of the pad, and is approximately equal

to 0.0051 mm/mm. This result correlates to the reduced stress (when compared to the elastic model) seen in Figure 61, as the energy absorbed by plastic deformation, reduces the overall stress experienced by the body. However, validation of this result is difficult as an extensive experimental setup would be required.

6.6 Improvements, Failures, Model Adjustments & Further Improvements

The impact rings and rotor assembly are one of the most critical and complex system of components in the motor. There are high impact loadings and stresses, and some of the models indicate contact forces between the rotors in the order of 10^4 to 10^5 N. Figure 63 illustrates the design of the rotor assembly and the main components. The purpose of this design was to improve the torque transfer from the pads of the impact rings to the rotor assembly from the previous design. Exact measurements were not taken of the number of cycles that the impact ring experienced because a higher priority goal of this experimental work was to generate performance data for the toroidal motor. Further, having an impact ring design that would remain consistent throughout multiple tests was the measure of improvements made to the components. The previous design used screws to tighten the face of the impact ring to the face of the rotor to transfer the torque. However, from testing it was found that the screws would fail in shear, due to the high contact forces between the impact rings. It can be seen that the impact rings have two integral square keys that function with keyways in the rotor and sleeve. These keys are intended to transfer the majority of the torque from the pad of the impact ring to the rotor and sleeve, as well as from the rotor to sleeve (and the drive shaft).

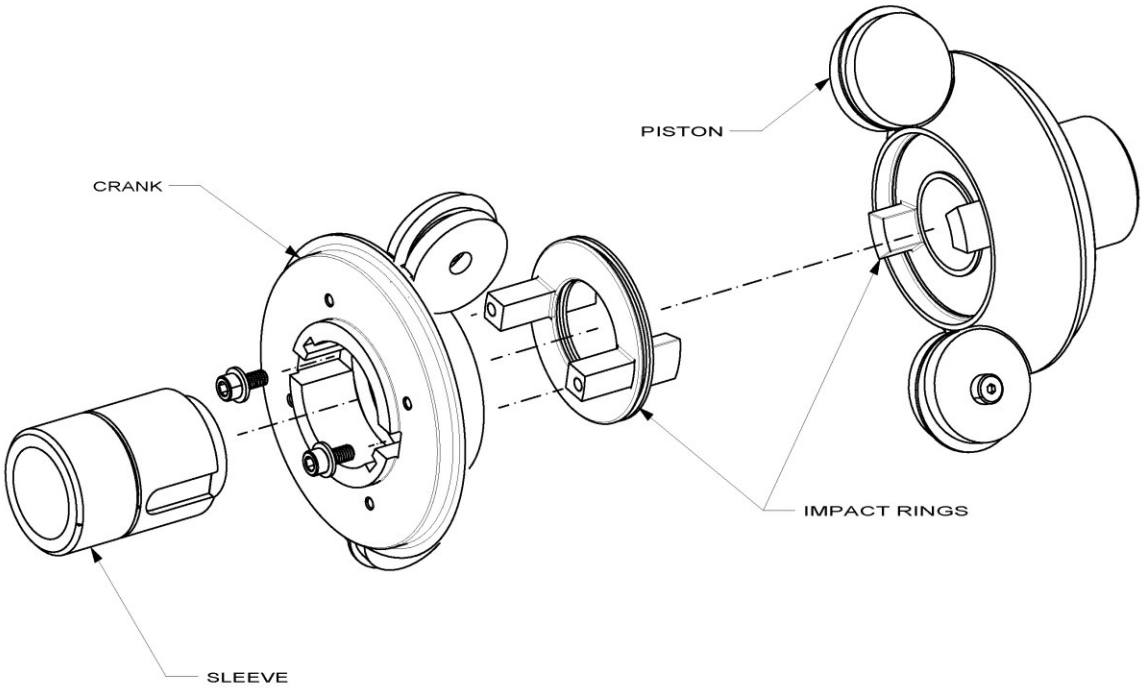

Figure 63 - Improved impact ring and rotor assembly including integral keys in impact ring.

The ring design shown in Figure 63 was built and tested. The rings worked without failure at first, but after multiple tests, various signs of wear were observed, and the rings ultimately failed, as shown in Figure 64. The main sign of wear that was observed with the ring design was with the screws that held the integral keys on the rings in to the back face of the rotors. The screws would tend to loosen due to vibrations and gouge the contacting areas of the rotors. This ultimately led to ring failure as shown. This failure is across the ring, which indicates a fatigue failure from the ring flexing and deforming.

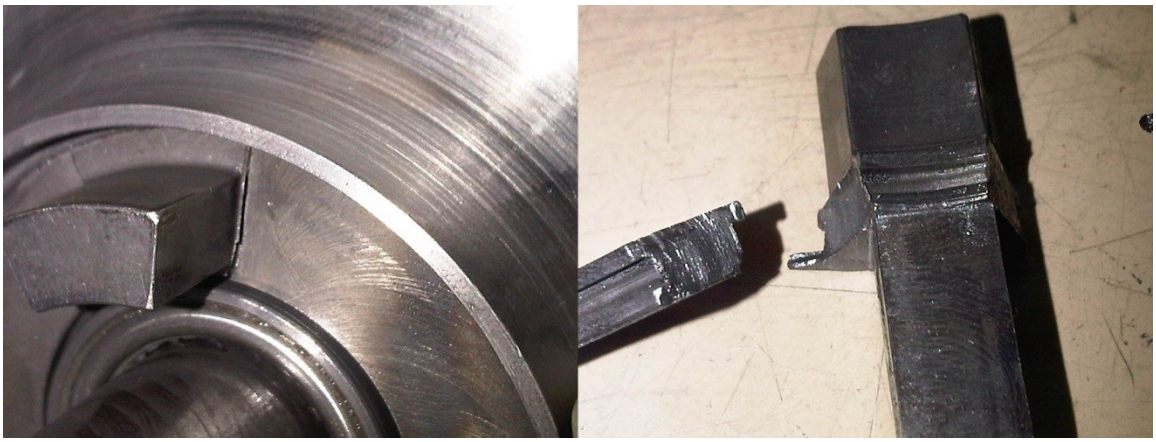

Figure 64 - Failure of impact ring with ends of integral keys fixed in the Y-axis.

A FEM model was tested to observe the tendency of the rings to deform, if the back faces of the keyways were constrained in the y-axis. This constraint is similar to the design shown above, as the screws holding the rings to the back face of the rotors are the only component holding the rings in the y-axis. Figure 65 illustrates the y-axis displacement of the rings at the peak contact stress. Note that the deformations have been scaled on the image 2X for visualization purposes.

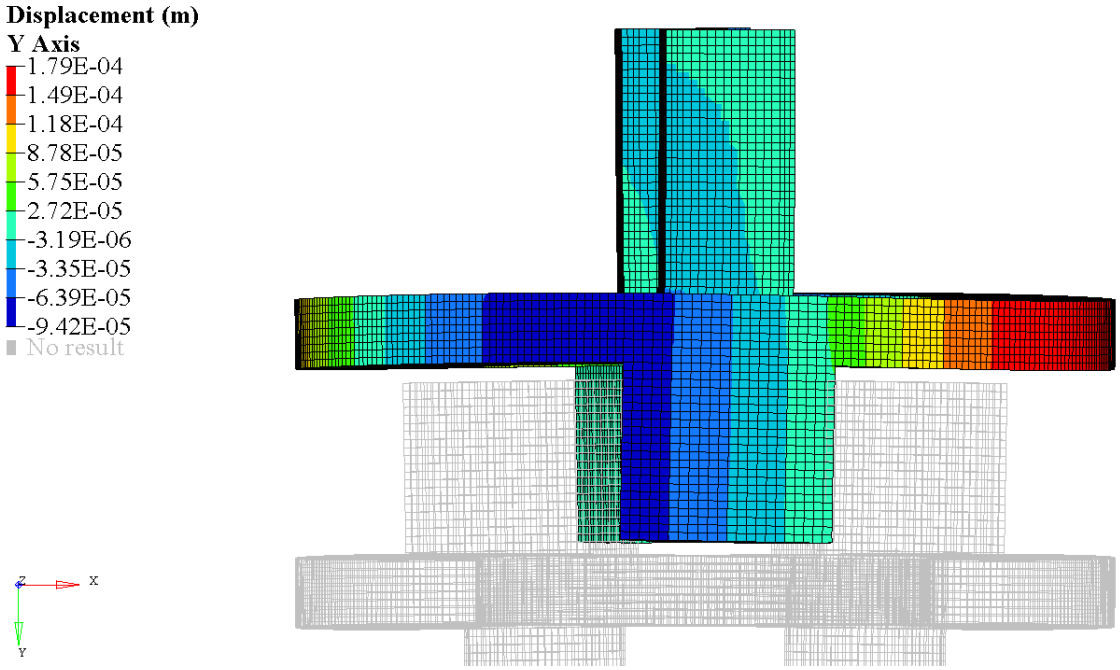

Figure 65 - Y-axis displacement of the impact ring FEM model with the outer most ends of the integral keys constrained in the y-axis. The deformed body is showing a 2X deformation scale.

It is seen from the FEM results that the ring tends to flex by almost 0.2 mm in the y-axis during contact. From observations of the model and the failed ring, it is concluded that this freedom of movement will ultimately lead to further ring failures, and design alterations are required. In particular, it is advantageous to constrain the face of the ring to the face of the rotor to prevent this deformation from occurring. Figure 66 illustrates the improved design of the ring to reduce the fatigue on this area of the ring.

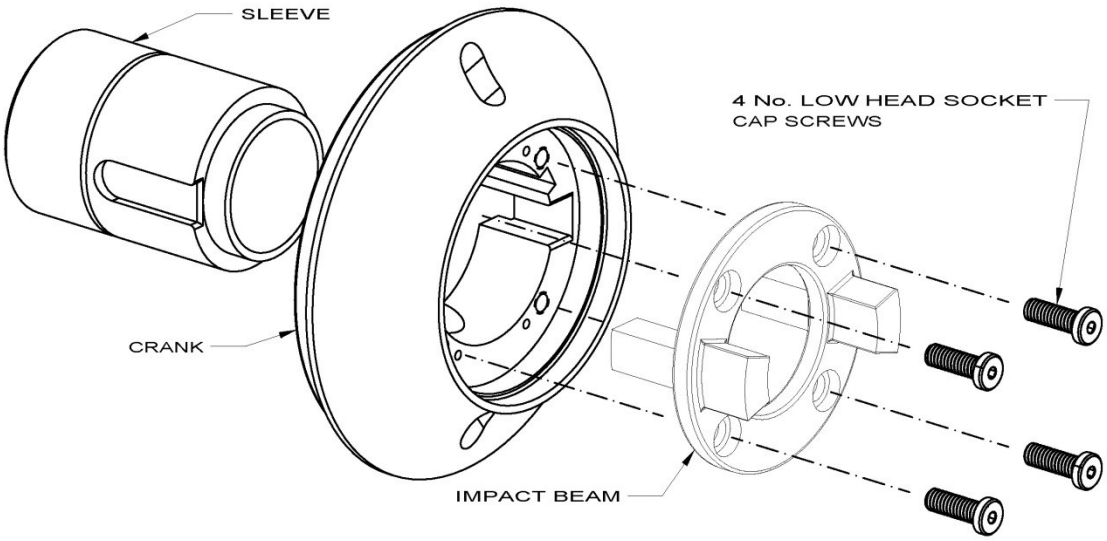

Figure 66 - Impact ring assembly with integral keys and screws to fix the ring to the face of rotor.

The model predicted that this design reduced the stresses experienced in the ring of the part, and it was observed through bench top testing that the design shown in Figure 66 operated without failure for a much longer time than the previous design. However, cracks were noticed that were propagating from the same location as observed previously, as shown in Figure 67 below. In addition, wear was shown on the contact of the faces of the rings. It was thought that this wear was likely due to the stress concentration of the corner between the ring face and the pads. Therefore, to improve this, a FEM study was conducted to determine the best pad length for the current rotor design.

6.6.1 Pad Length Study

Figure 67 illustrates the stresses of the contacting face of the impact ring at peak contact force. It is seen that all the pads have the same general trend of compressive stress on the outer part of the pad, and tension in the corner between the pad and the ring. However, as the pad length decreases, the area of elements in considerable contact stress increases. The goal is to have the contact force spread over the whole face, as evenly as possible. Furthermore, with longer pad lengths, the faces of the pads are less effective, and the contact forces are concentrated to the outer most regions of the pads.

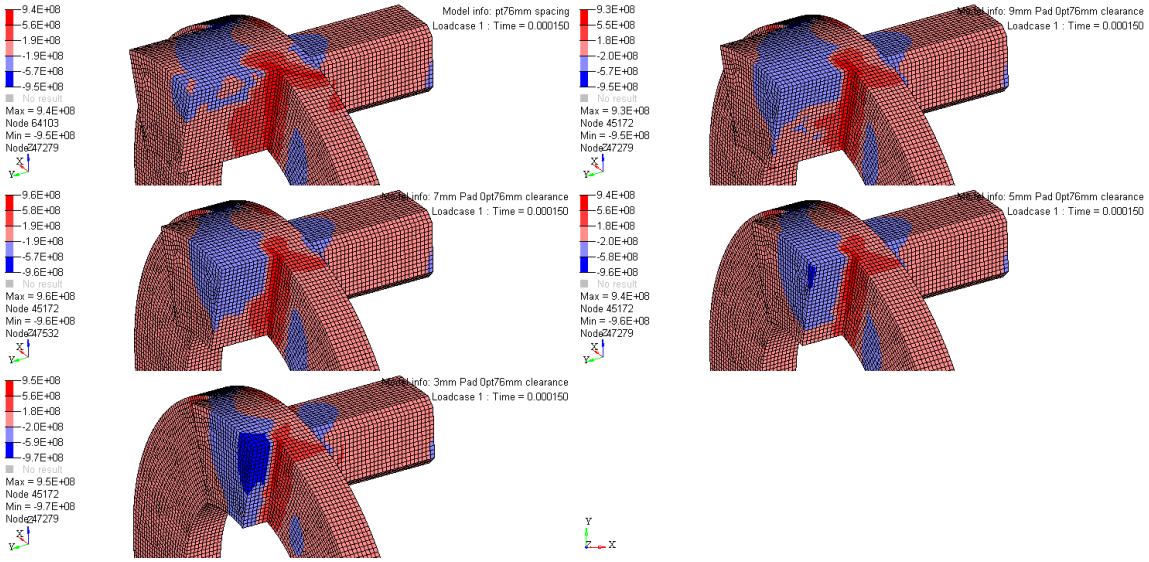

Figure 67 - Illustration of the results of the pad length study for pad lengths of 11mm, 9mm, 7mm, 5mm, and 3mm with a fixed spacing of 0.76mm between the face of the ring and the end of the pad on the opposing rotor assembly. Note that positive stresses are in tension and negative stresses in compression.

The relationship between the amount of contact elements in compression and the pad length can be seen in Figure 68. It can be seen that as the pad length decreases, the percentage of elements in contact increases.

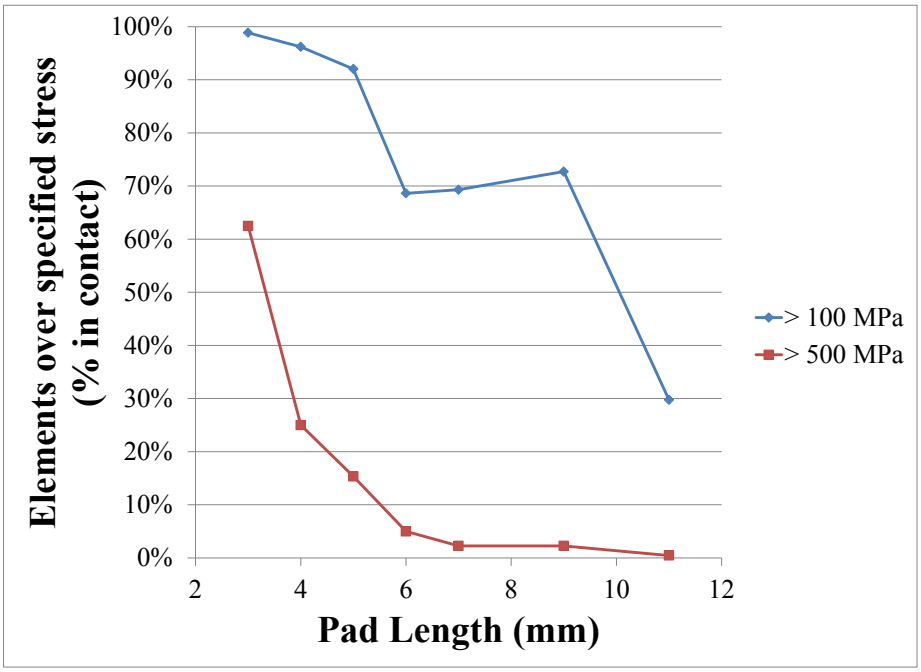

Figure 68 - Relationship of the percentage of contact elements in compression over 100MPa and 500MPa for various pad lengths of 11mm, 9mm, 7mm, 5mm, and 3mm with

a fixed spacing of 0.76mm between the face of the ring and the end of the pad on the opposing rotor assembly.

Figure 68 shows that for pad lengths of 6mm to 9mm, the number of elements in stress over 100MPa is around 70%, while the number of elements in stress over 500MPa remains below 6%. Therefore, if the intent is to have the majority of elements in compression in the range of 100MPa to 500MPa, then this range of pad lengths is the best choice. Furthermore, Figure 69 shows the peak and average tensile and compressive stresses in the corners between the pad and ring. It is seen that, generally, the peak and average tensile stresses and the peak compressive stresses increases with pad length. Therefore, when combined with the observations of the number of contact elements in compression, the best pad length is 6mm. It is also seen that 6mm has the lowest peak tensile stress.

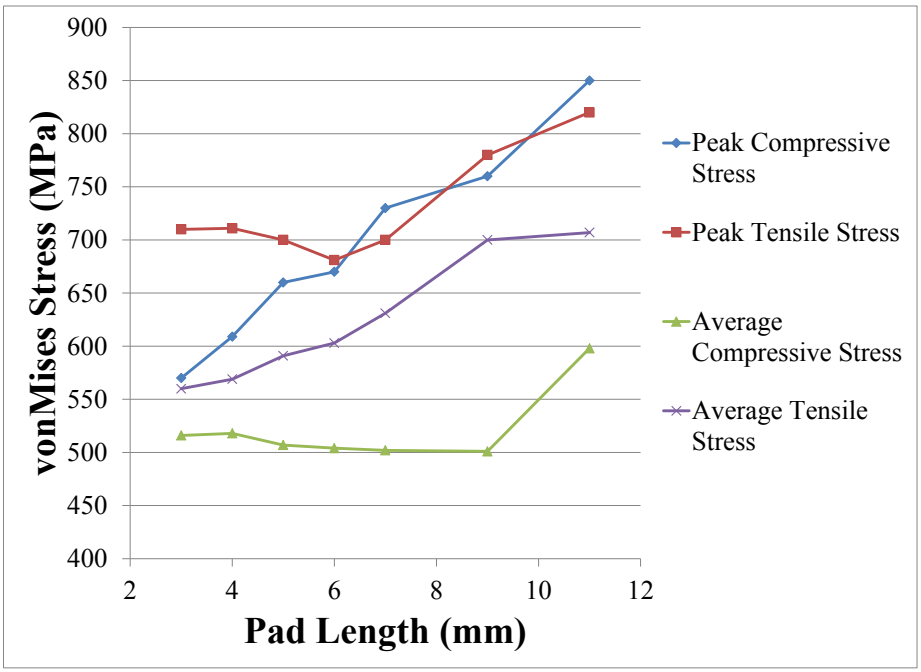

Figure 69 - Relationship of the peak and average vonMises stresses in the corners between the ring and the pad in tension and compression for various pad lengths of 11mm, 9mm, 7mm, 5mm, and 3mm with a fixed spacing of 0.76mm between the face of the ring and the end of the pad on the opposing rotor assembly.

6.6.2 Pad Shape

Further to the pad length study, the geometry of the pad on the impact ring was studied. Three different shapes were studied, as seen in Figure 70. The pad shapes are a straight pad, straight pad with fillets, and an angled pad with fillets.

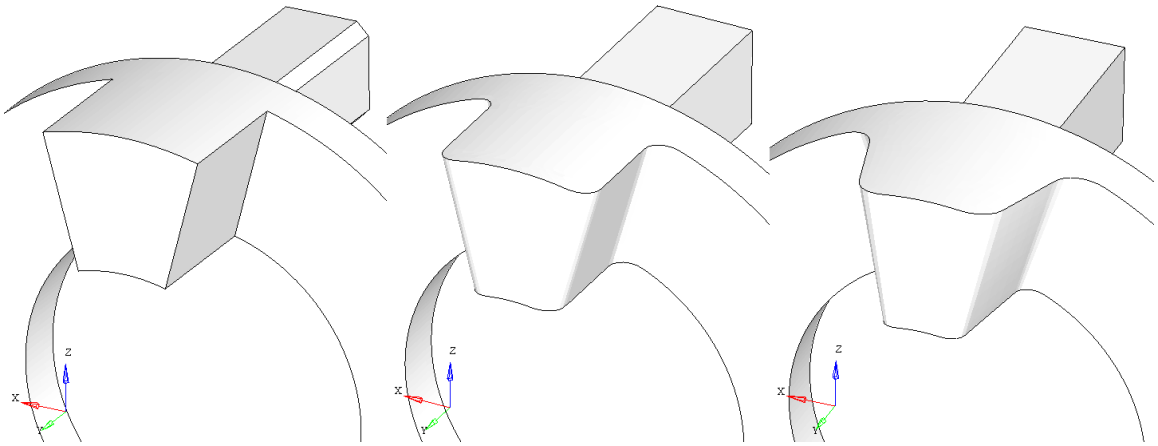

Figure 70 - Illustration of three different pad shapes studied: straight pad, straight pad with fillets, and an angled pad with fillets.

Figure 71 illustrates FEM model results of an 11mm pad with 3.175mm radius fillets, and a 11mm pad with a 40º pad angle. It is seen from the results that the angled pad has an even stress distribution across the contact area of the pad, and reduced stress in the corner between the pad and the ring. These two characteristics are desirable to reduce the fatigue stresses that occur in the part.

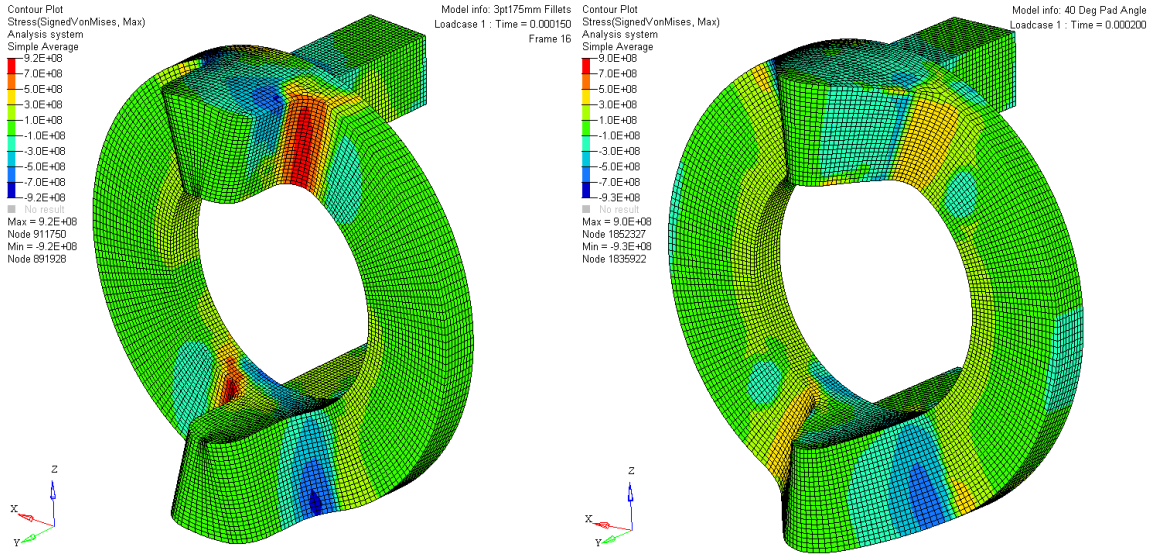

Figure 71 - FEM model results of a filleted pad and angled pad with fillets.

From these modeling and testing results, it can be seen that the model plays a critical role in driving the design of the impact rings. In particular, the model qualitatively predicts the locations of stress concentrations in the model, the shape of the impact pads and the method of securing the rings to the rotors influences the stress and fatigue experienced by the impact ring, and the shape of the pads can be adjusted to greatly reduce the stress concentrations in the corners between the pads and the ring. Therefore, the model was a useful tool for the development of this component, and the stresses experienced by the impact rings were reduced by modifying the geometry.

CHAPTER 7 PISTON DESIGN

7.1 Piston Shape and Assembly

The piston design used in previous development is shown in Figure 72. The pistons are constructed of a 3-piece assembly, with integral cup seals to form the seal between the chamber and each of the pistons (80).

Figure 72– Three-piece piston assembly (80).

This configuration was beneficial to using a toroidal shaped piston, because this method required less complicated manufacturing methods, which is a secondary driver of the development of the motor. However, the pistons had limited performance because of limited sealing and high friction. The seals did not align properly with the chamber to form an effective seal, as gaps were noticed between some locations in the chamber, as highlighted in Figure 73. This indicates that the seal is pressed against other locations of the camber, causing excessive friction. In addition, the seals were unable to compensate for wear; therefore, in order to reduce the friction of the seals, it was determined that the best method was to use pistons configured with conventional compression rings for seals, as these seals provide a low-friction wear compensating seal for circular cross sections (34).

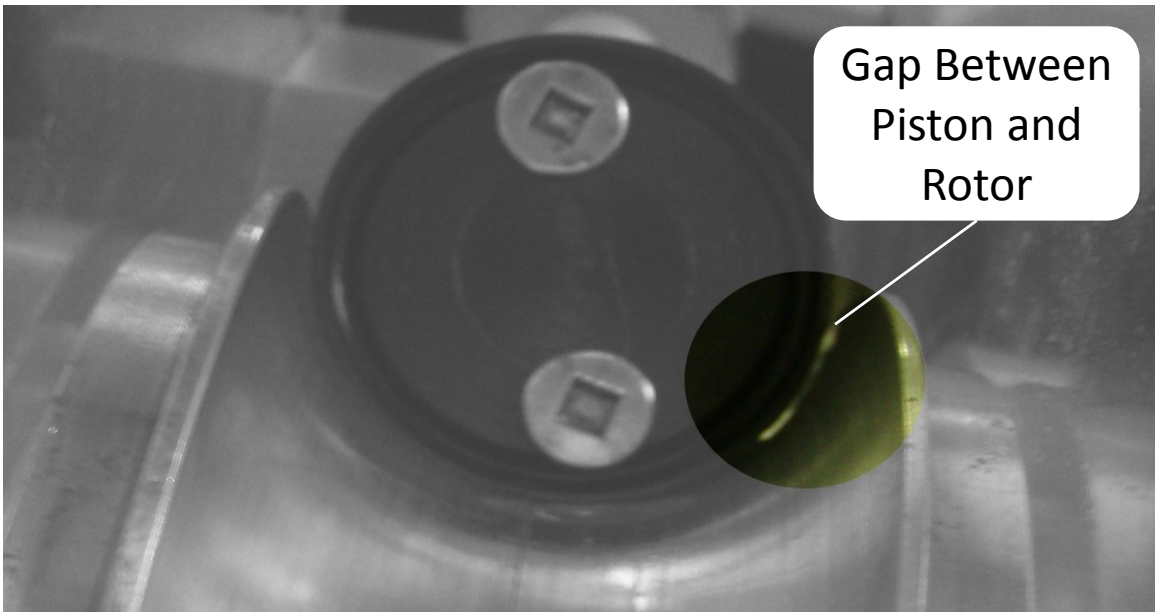

Figure 73 – Picture of the gaps between the rotor and piston seal.

Additionally, the pistons were attached to the rotor with a cap screw. This proved to be ineffective, because the forces acting on the faces of each piston would tend to twist the piston along the axis of the screw, which would cause the screw to loosen, and ultimately lead to thread failure.

The pistons are intended to separate the chambers formed by the toroidal geometry of the engine. Therefore, the seals are subject to sealing pressures from both sides of the piston. This requires the ring to form a seal between the toroidal casing and either of the sealing faces of the groove on the ring land. A solution to this can be seen in Figure 74. The piston is shaped as a toroid to form a static mating seal between the piston and the rotor that it is attached to. This was thought to reduce the loosening of the cap screw, and form a static seal between the piston and rotor. The design of the piston has a reduced diameter toroid to provide clearance between the piston and the opposite rotor (non-attached) and casing.

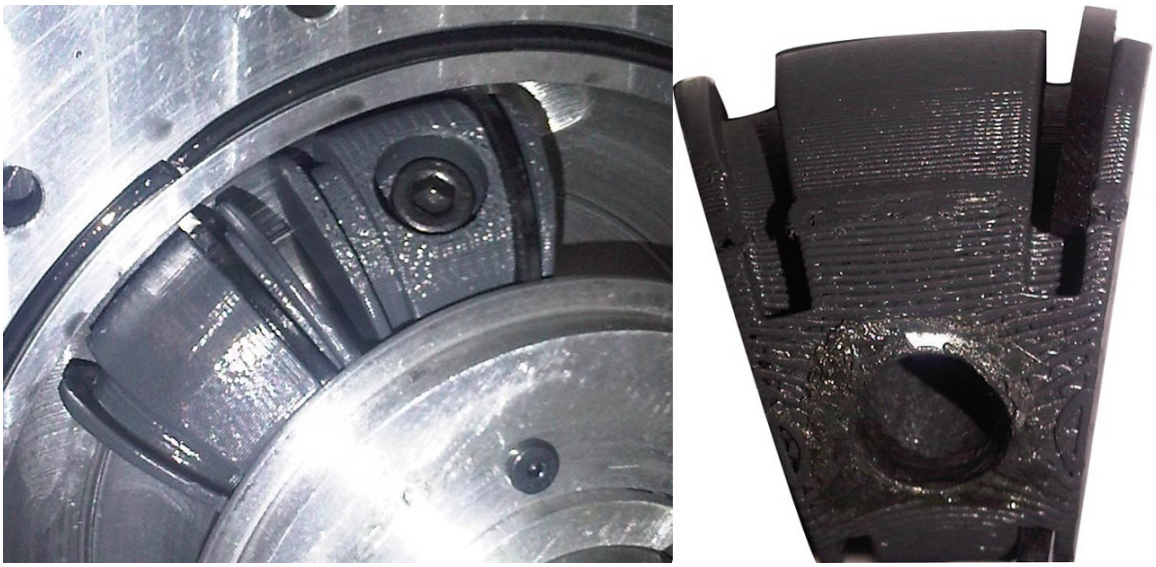

Figure 74 - Toroidal piston with static seal on attached rotor, and piston ring seal on the sliding rotor.

The sealing requirements are similar to that of an un-lubricated (dry) piston compressor. Recommended ring materials for these applications are harder, filled plastics like Acetal Copolymer (60-70 Shore D hardness) with low wear characteristics, and relatively high tensile strength (12-20 MPa). It's also listed that two rings are suitable for pressures up to 290 psi, and three rings are suitable for pressures up to 870 psi (34). Most pneumatic motors operate at pressures up to 100 psi. Therefore, allowing for two rings on the piston, will allow testing with either one or two rings installed.

Piston rings have a gap to allow the rings to energize against the chamber as they wear, and to allow the rings to be installed onto the piston. This gap creates a passage for air in conventional reciprocating engines. The effect of this gap on the overall sealing is minimized by diametrically opposing the gaps of two or three rings. The effect of this gap can be greatly reduced by positioning the gap against the static seal formed between the piston and the rotor. Figure 74 illustrates how the piston forms a static seal with the rotor it is attached to, and also illustrates how the piston ring is aligned to form a continuous seal with the sliding surfaces around the remaining portion of the piston.

As seen in the figure, prototypes of this piston design were tested. Testing with these pistons demonstrated that having one seal rather than two seals were advantageous for reducing friction generated by the seals. This reduces the friction caused by the seals, and allows the piston to act as a vane. The pistons seal from both front and back faces and it

is advantageous to have minimal area of the piston with seals on it. i.e. it is better to have two seals adjacent to each other (for example space 1.5º apart) than two seals at opposite ends of the pistons (as shown in Figure 74). This was learned from testing these pistons, because the engine would tend to stall with the piston half way across the transition phase (with the compressed air inlet between the two seals of the piston). Further, it was observed that minimizing the size of the overall piston body would reduce stalling during the transition phase.

The piston shown made from rapid prototyped ABS plastic. The material is effective for illustrative purposes, but the prototyping has limited tolerances and strength. From further investigation to other prototyping methods, manufacturing a piston with this shape is not straightforward, and would require complex CNC tooling. Additionally, manufacturing processes are being investigated with practicality and cost of mass-producing the pistons being taken into consideration. Therefore, the piston design was further developed to simplify the complexity of manufacturing, which was a priority of this experimental development.

A connection was developed between the piston and the rotor that is designed to transfer the forces from the piston to the rotor without loosening. The assembly is illustrated in Figure 75. A piston paddle extends from a slot in the piston to a slot in the rotor. The oval-shaped paddle provides resistance to bending and torsion, which would cause the piston to loosen otherwise. The piston is constructed of a straight cylinder section with an angled groove that is oriented to provide sealing surfaces that are oriented to form circular sections of the toroidal chamber for the compression ring. A static seal (O-ring or gasket) is placed between the toroidal surface of the rotor and the outer surface of the piston. A screw holds the piston on to the paddle through a hole in the center of the piston, and a screw fastens the bottom of the paddle to a shoulder on the inner surface of the rotor.

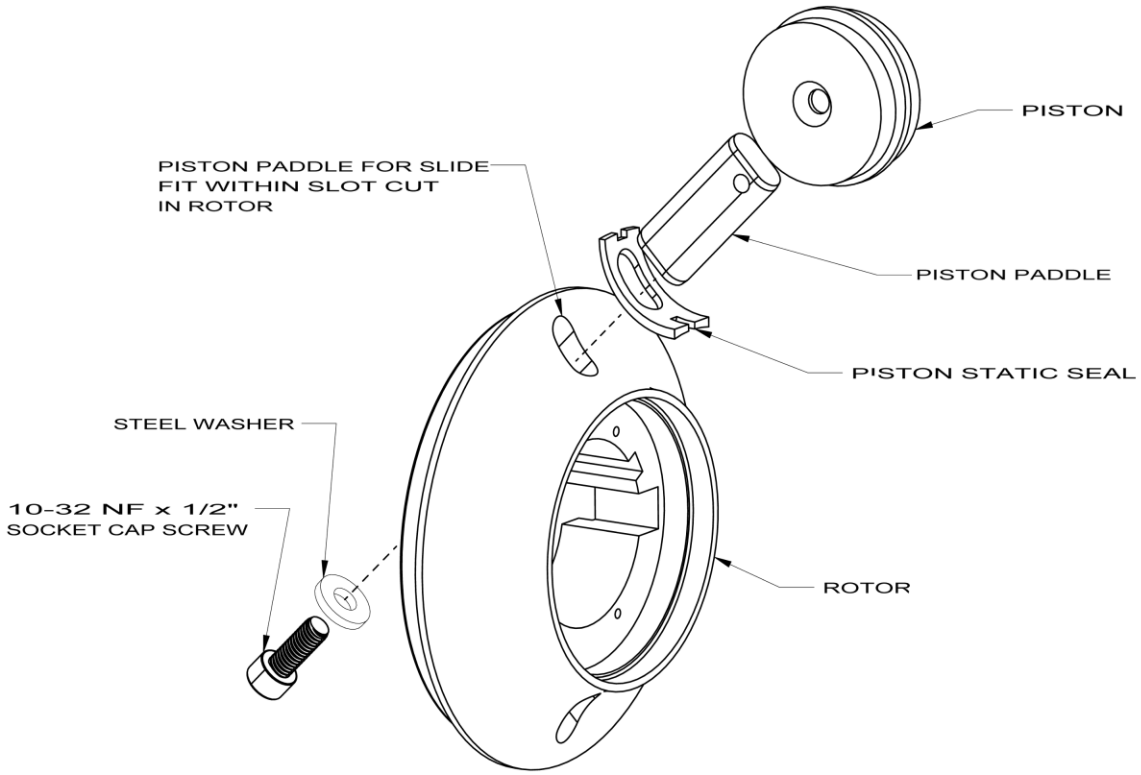

Figure 75 - Illustration of an improved piston connection to the rotor.

Figure 76 illustrates the installed assembly with a rapid prototyped piston. It was found from testing that this assembly worked very well. However, the rapid prototyped pistons were not strong enough, and would tend to fail after a short amount of testing.

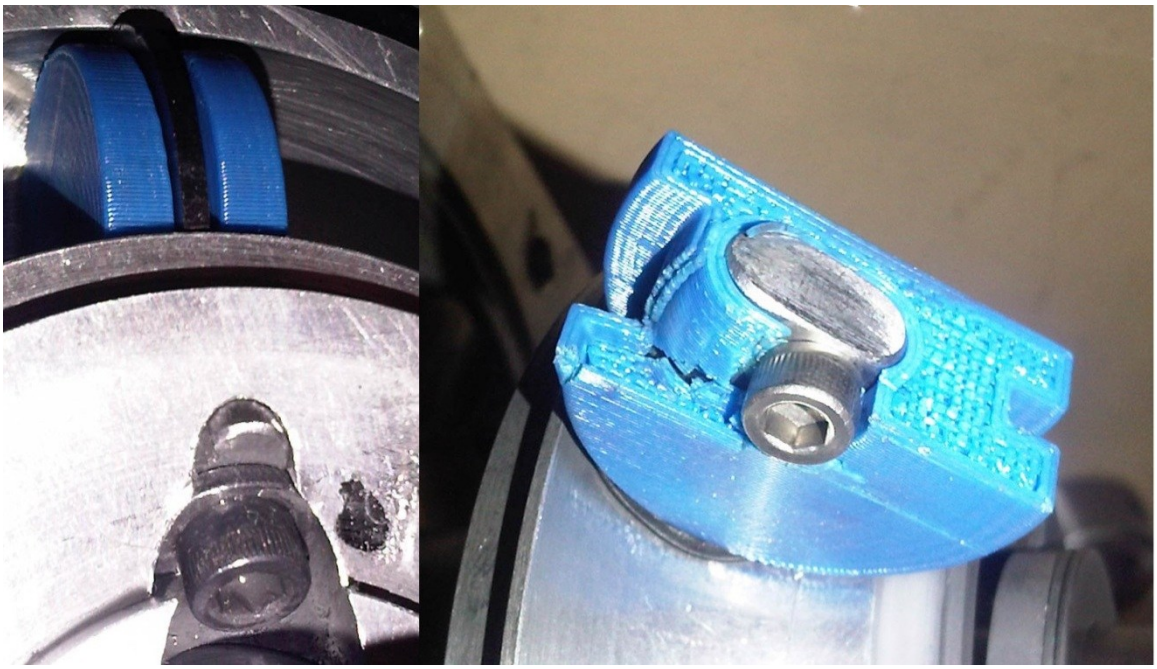

Figure 76 - Installed piston with piston paddle and rapid prototyped piston (left), and failed rapid prototyped piston (right).

As was observed with the rapid prototyped pistons, it was necessary to manufacture a piston out of a stronger material such as aluminum. However, manufacturing an angled groove in a straight cylinder requires a custom jig. The following section describes how the angled groove pistons are manufactured.

7.2 Angled Groove Piston Manufacturing

As illustrated in the previous sections, it is necessary to manufacture an angled groove in the pistons. This specifications of the groove are particularly complex, because the groove has to be the correct width and depth, the faces need to be at the correct angle, and the faces need to be oriented correctly relative to the mounting slot. A method was developed to be able to manufacture this groove in the pistons out of mid strength metals (Ex aluminum and mild steel) with a conventional (non CNC) lathe.

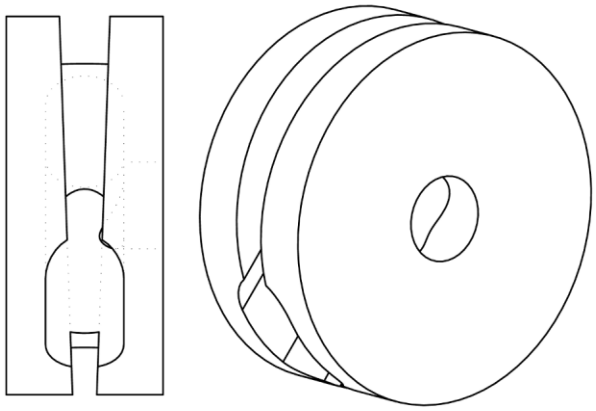

Figure 77 - Illustration of required piston geometry with angled groove and slot for piston paddle.

Figure 77 illustrates the orientation of the groove and slot for the piston paddle on the piston. It is seen that the piston is constructed of a straight cylinder. The groove is oriented such that it is the largest at the outermost location of the piston (from the drive shaft), and the smallest at the innermost location of the piston. The slot is projected 45º from the inner most section of the piston to align with the 45º slot in the rotor. This configuration orients the groove such that the plane formed the faces of the groove cuts a circular section of the toroidal cylinder for the ring to seal against.

To cut the angled groove in the cylinder, a specialized jig is required to hold the cylinder in a lathe. The jig is designed such that the cylinder is held off-axis from the center axis of the lathe. This allows a standard groove cutting tool to cut an angled groove in the cylinder. The cylinder is then rotated and flipped, and another angled groove is cut. These two grooves overlap, and form the surfaces of the angled grove in the piston. Figure 78 illustrates the design of the jig system, and a flow chart detailing the manufacturing process is illustrated in Figure 79.

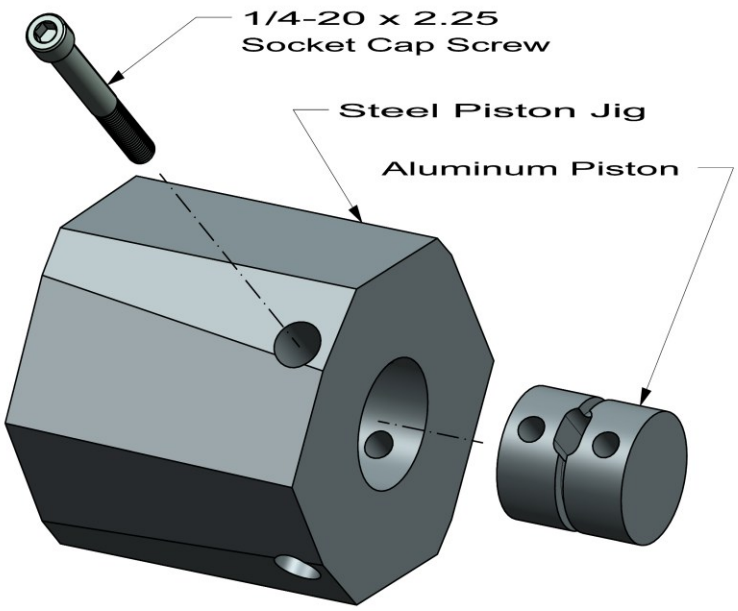

Figure 78 - Angled groove jig setup.

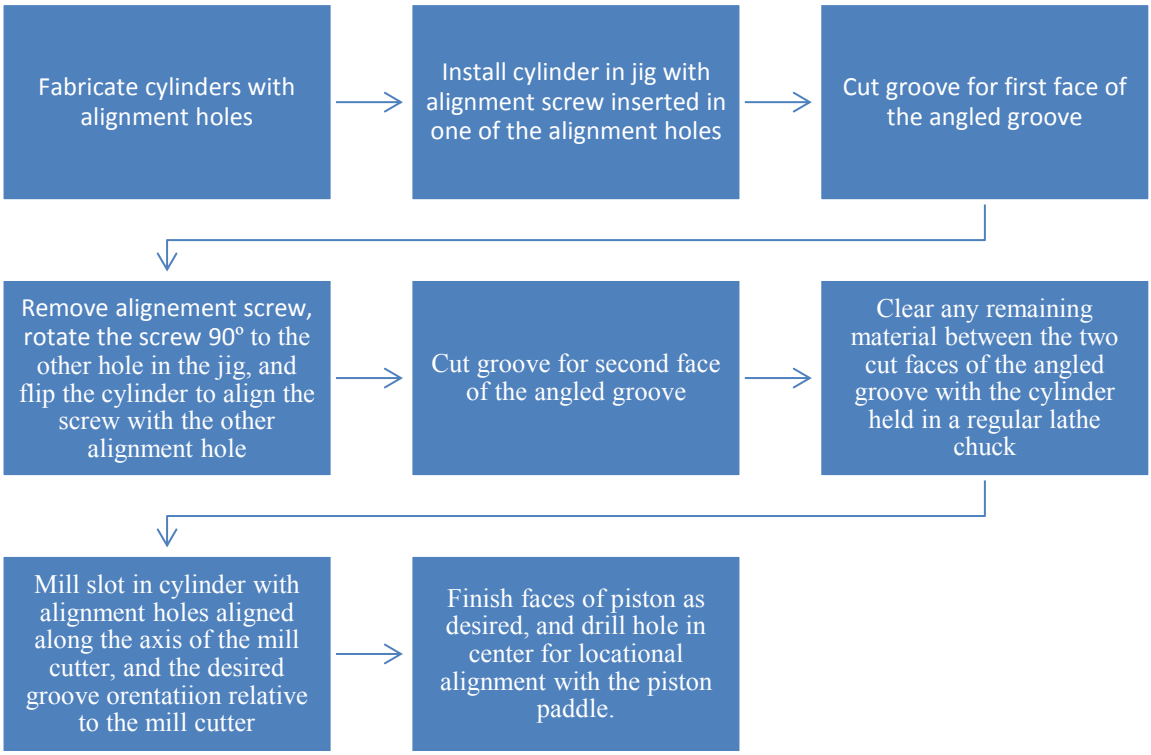

Figure 79 - Flow chart of angled piston groove manufacturing process.

In order to accurately cut the grooves in the cylinder, the accuracy of the jig had to be checked. A Shape Grabber AI310 3-D scanner was used to scan the jig to measure the locations trajectories of the alignment holes and the center hole. It was found that the two

alignment holes furthest from the front face of the jig were 0.951 ± 0.002” from the center of the front face, and the inner two holes were 0.453 ± 0.005” from the center of the front face of the jig, as shown in Figure 80. Therefore, all of the alignment holes are within reasonable locational tolerance, and the alignment holes on the cylinders should be placed 0.951” and 0.453” from the center of the groove, for the outer and inner holes respectively. However, it is more desirable to use the outer most holes, because of the increased accuracy. The center hole was found to be within 0.0016” of the desired location (xyz-magnitude), and the axis of the hole was within 0.108º of the desired 1.5º.

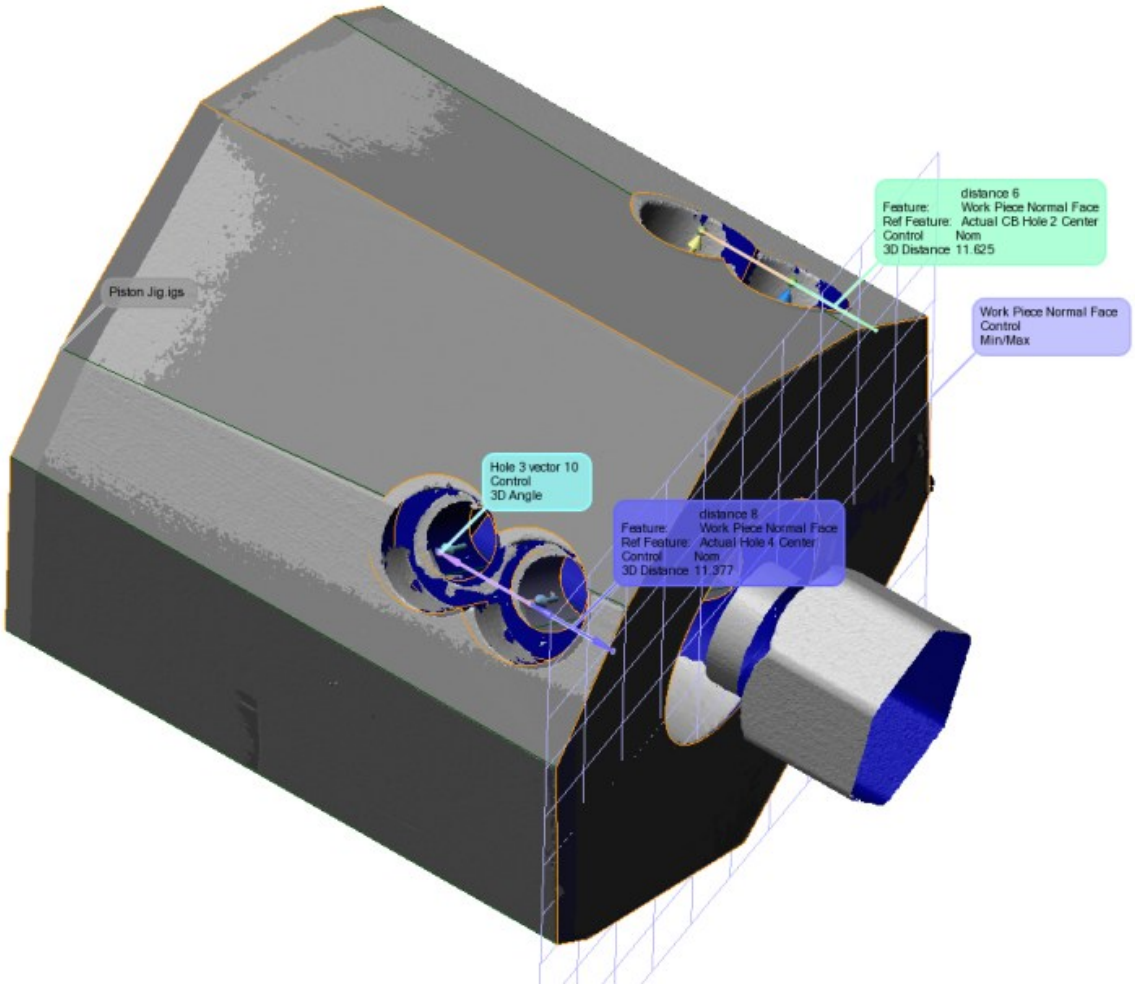

Figure 80 - Scanned model of piston jig for calibrating groove cutting specifications.

After the accuracy of the jig was measured, the front face of the jig needed to be faced to allow for clearance of the grooving tool. The face was reduced by 0.050”; therefore the center of the hole that holds the piston cylinder was now 0.050” from the face of the jig. This is important to positioning the cutting tool for the faces of the grooves to be

accurately placed. Figure 81 and Figure 82 illustrate the jig setup while cutting an angled groove, a close-up of the cutting tool and clearance between the face of the jig,

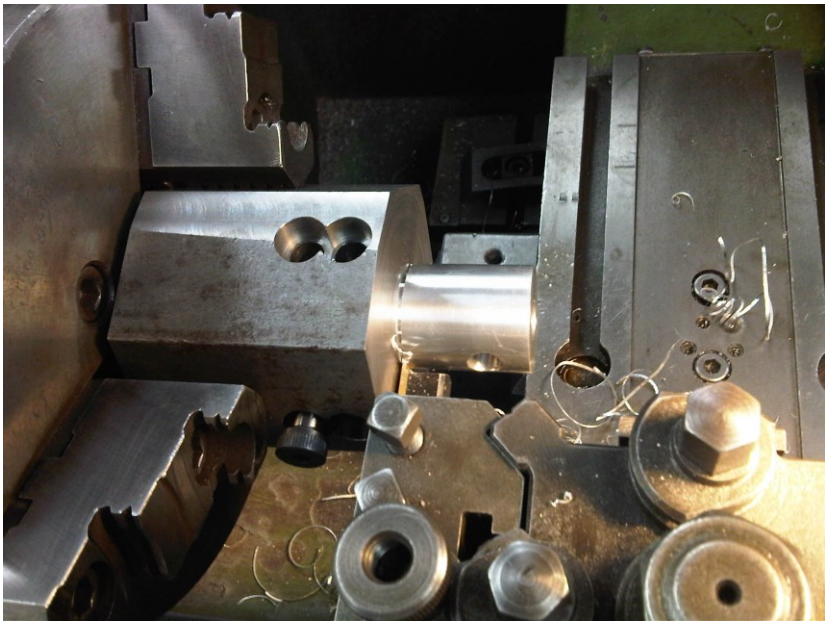

Figure 81 - Picture of angled groove jig while cutting the second face of the angled groove.

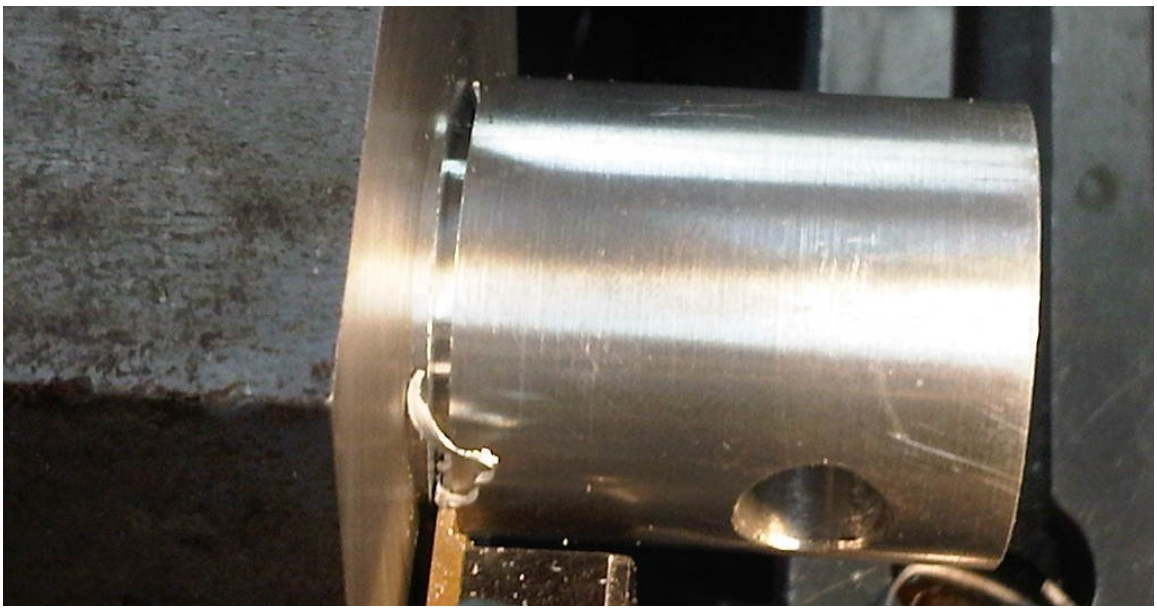

Figure 82 - Close-up of second face of angled groove being cut in cylinder.

Figure 83 illustrates the cylinders before and after the angled grooving process has been completed. Figure 84 illustrates the finished pistons, and a piston installed in the motor. It can be seen that the grooves are aligned with the slot in the piston, and that the largest

part of the groove is located at the outermost point of the piston, and the smallest part of the groove is at the innermost point of the piston.

Figure 83 - Piston cylinders before (left) and after (right) grooves cut with angled groove jig.

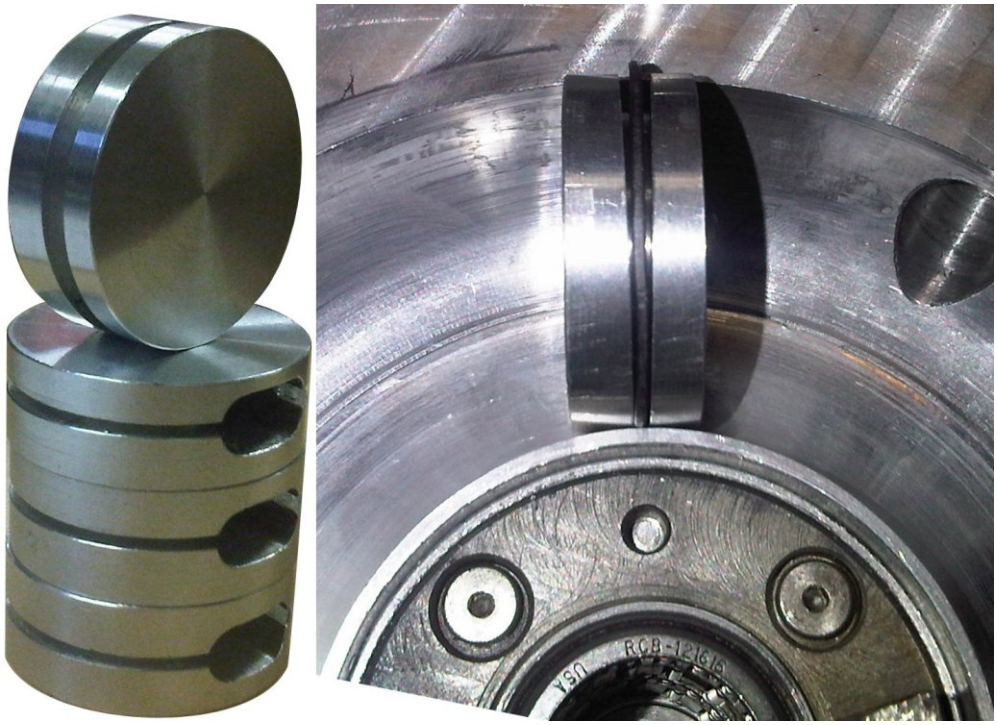

Figure 84 - Final aluminum pistons manufactured (left), and example of piston installed in motor with compression ring seal installed.

CHAPTER 8 EXPERIMENTAL TEST SETUP

The following section describes the test setup to conduct the experimental testing for this thesis. This includes the motor specifications, description of the dynamometer system, compressed air supply system, air flow measurement system, and integration of custom measurements into the dynamometer software.

8.1 Motor Specifications

Figure 85 shows a picture of the toroidal motor developed and tested. It is seen that the motor is constructed of two rotors with two pistons on each rotor, and two sections of a casing. The rotors and casing form the toroidal chamber, and the pistons seal separate cells within the working chamber.

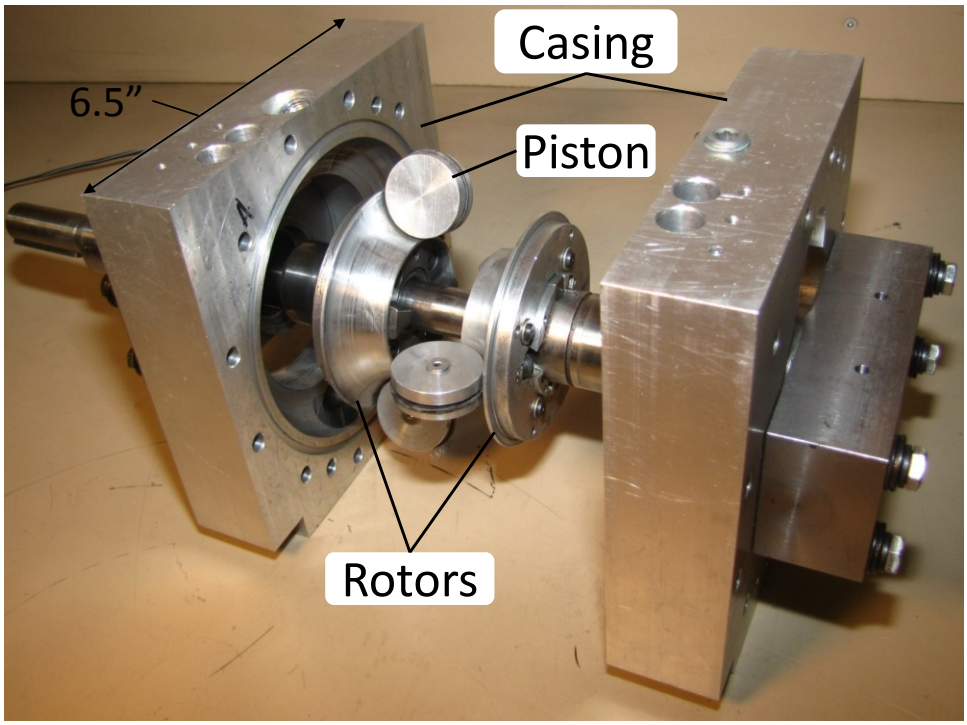

Figure 85 – Picture of the toroidal motor prototype developed and tested.

The rotors rotate intermittently and torque is transferred to a common drive shaft with an arrangement of one-way bearings. The bearings couple each rotor to the drive shaft when rotating forwards, allows the drive shaft to rotate when each rotor is stationary, and prevents each rotor from rotating backwards, as illustrated in Figure 86.

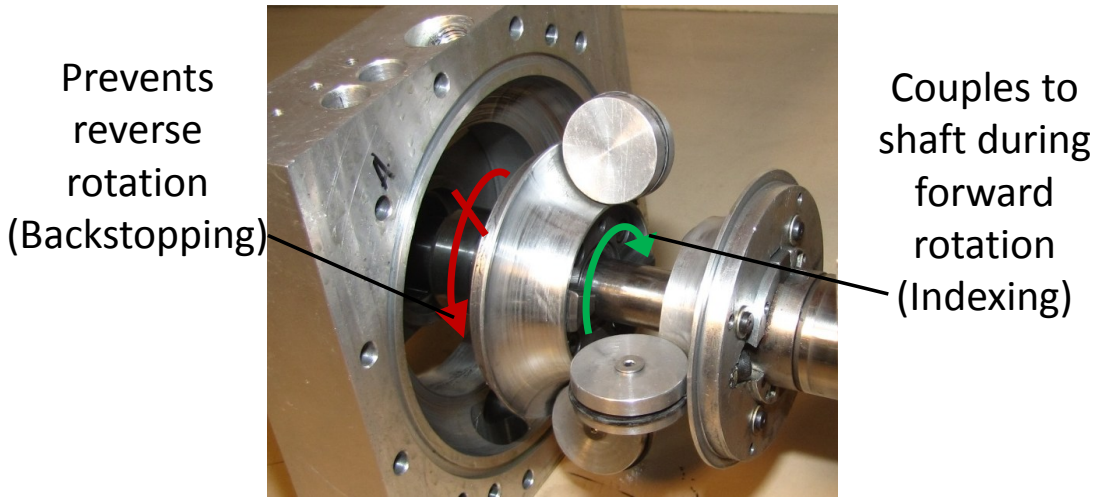

Figure 86 – Schematic of the function of the one-way bearing arrangement on one of the rotors of the toroidal motor.

The overall motor size, piston radius (R_p), and rotor radius (R_c) is shown in Figure 87. The piston radius and rotor radius (or piston offset), are used to calculate the displacement of the motor.

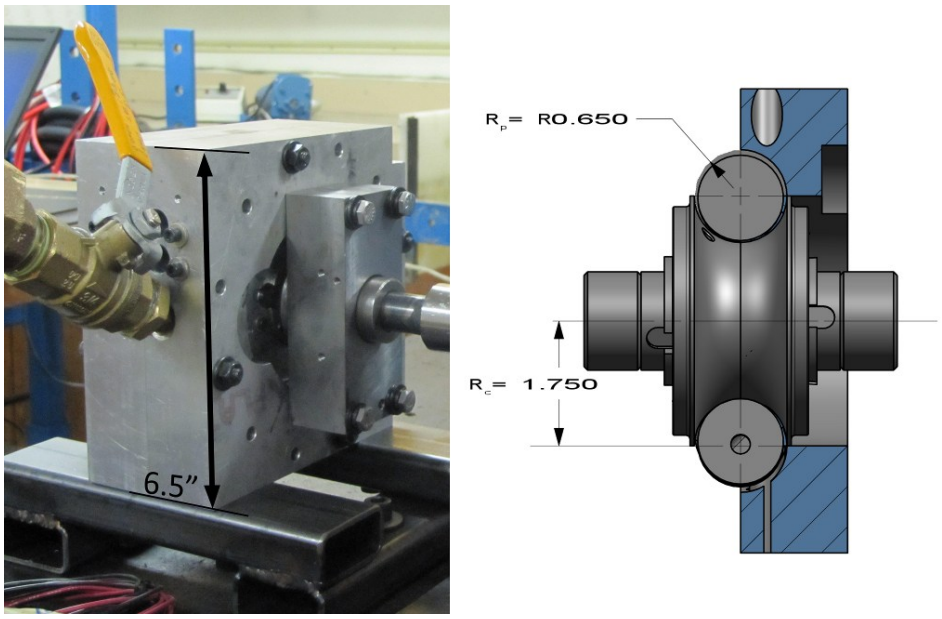

Figure 87 - Motor size, piston radius (R_p), and piston offset (R_c).

Figure 88 illustrates the minimum and maximum angles between the pistons on opposite rotors. These angles are limited by the contacting surfaces of the impact ring, and the difference between the two angles gives the maximum displacement angle θ_{max}.

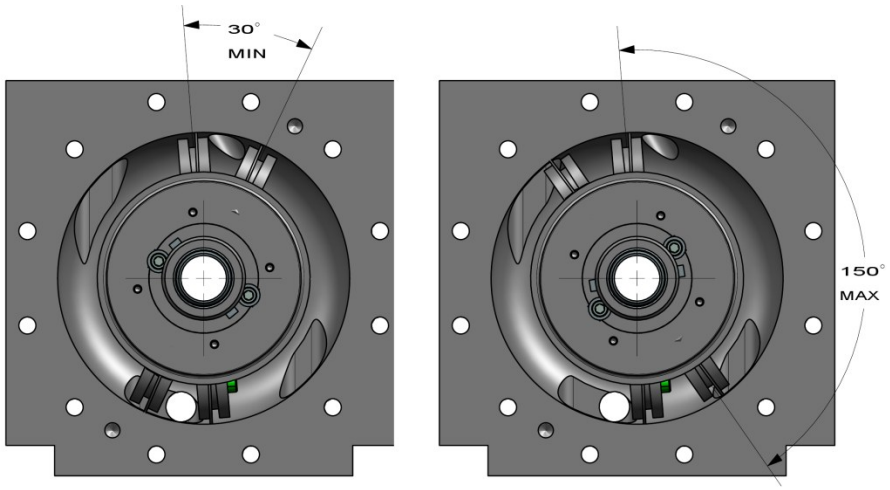

Figure 88 - Motor minimum (left) and maximum (right) displacement angles.

The listed parameters and resulting calculations are summarized in Table 5.

Table 5 - List of motor parameters used for testing.

Parameter	Value
$\boldsymbol{\theta_p}$	30°
$\boldsymbol{\theta_{max}}$	120°
$\boldsymbol{R_p}$	0.650 in. (1.65 cm)
$\boldsymbol{R_c}$	1.75 in. (4.45 cm)
$\boldsymbol{R_s}$	2.4 in. (6.1 cm)
$\boldsymbol{R_p/R_s}$	0.27
$\boldsymbol{n_p}$	4
$\boldsymbol{n_{noz}}$	1
$\boldsymbol{V_{cell}}$	4.86 in.^{3} (79.7 cm^3)
$\boldsymbol{V_{disp}}$	11.7 in.^{3} (191 cm^3)

The casing surrounds the pistons to form a sealed chamber, thus has the same section radius (R_p), and the same revolved radius (R_c). However, since the prototype was initially designed to simulate a four-stroke internal combustion engine, the tested motor has many ports to perform various functions. Various modifications were made to test the prototype as a pneumatic motor. In particular compression relief ports converted the motor from a four-stroke (intake, compression, expansion, exhaust) motor to a two-stroke pneumatic motor (expansion, exhaust). The angular locations of these ports are illustrated in Figure 89.

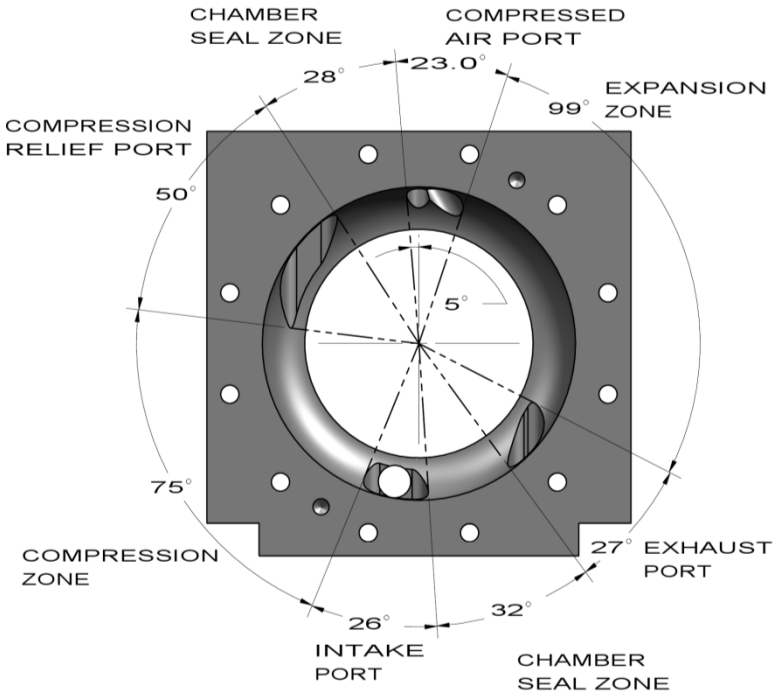

Figure 89 - Illustration of angular port locations in the toroidal pneumatic motor prototype.

The cross sectional port areas of the ports shown are listed in Table 6.

Table 6 - Cross-sectional port areas.

Port	Area (in.^{2} / cm^2)
Compressed Air	0.0490 / 0.317
Exhaust	0.452 / 2.92
Intake	0.889 / 5.73
Compression Relief	0.785 / 5.07

Figure 90 illustrates the modes that a cell experiences as the motor rotates. It is seen that expansion of the compressed gas occurs until the leading vane of the cell reaches the start of the exhaust port. The cell then enters an exhaust transition mode where the air in the cell starts to exhaust as the exhaust port is opened. The cell enters a transition mode, where the leading and trailing vane rotate together, and therefore, the volume of the cell remains constant. The cell is in the transition mode until it reaches 180° of rotation (from the beginning of the last transition mode). Note that Figure 90 demonstrates the first cell positioned at the end of the previous transition zone. Therefore, the leading vane reaches its maximum travel at 150°, and the cell reduces volume, and exhausts the air in the cell. The following phases are a result of modifying the prototype, as described earlier in this

section. The intake mode draws air into the motor from the intake port until the compression relief zone is reached. Once the compression relief zone is reached the cell does not draw air from the intake port, rather air flows from the previous cell, around the leading vane, through the compression relief port. Once the cell reaches the end of the next transition phase, the volume of the cell is reduced, and air is exhausted out the compression relief port. The cell then enters a final transition phase and begins the process again at the expansion phase.

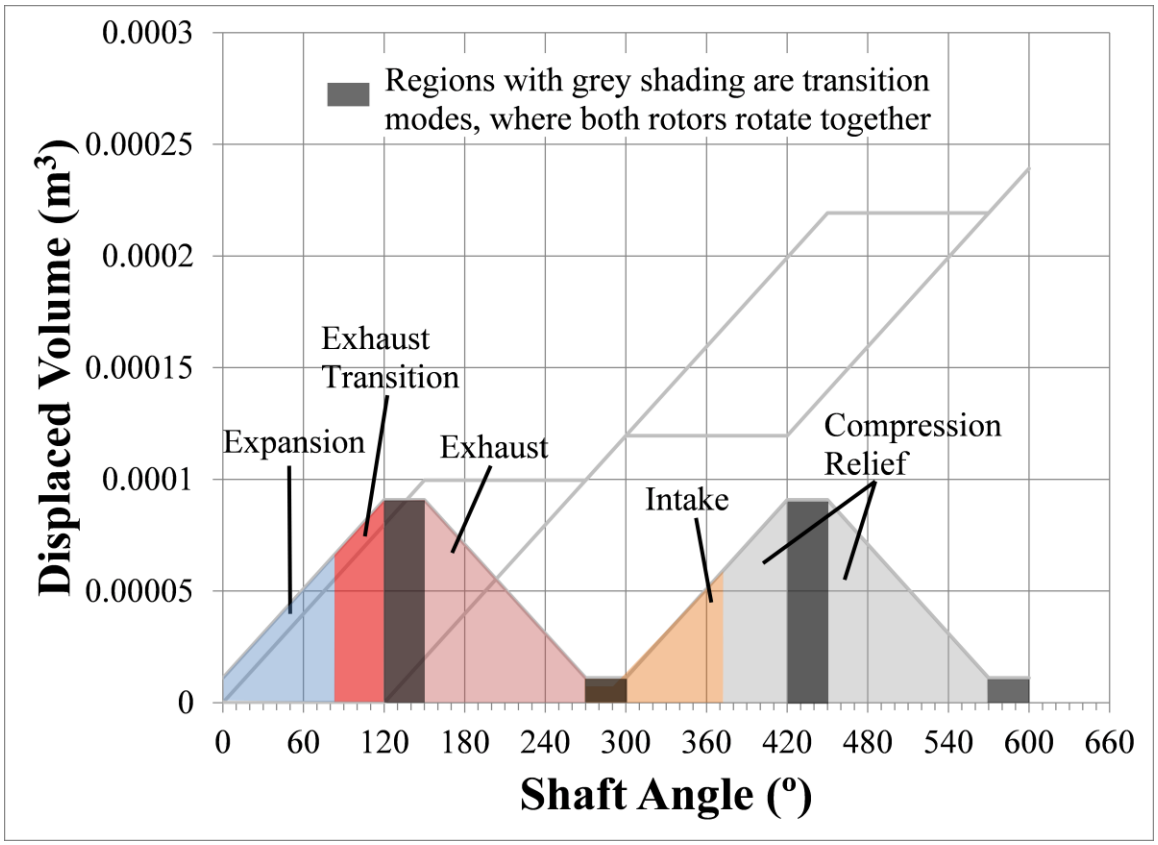

Figure 90 - Illustration of various phases of a cell volume in the toroidal engine prototype.

8.2 Compressed Air Supply & Measurement System Specifications

8.2.1 Dynamometer and Air Flow Measurement Systems

Figure 91 illustrates a schematic of the experimental setup and measurement system used for this study. The energy source is from compressed air tanks with industrial dry air. The air flow and pressure is controlled with a single pressure regulator that reduces the supply pressure from a high pressure line (200 psi) to the engine supply pressure presented for each test. The dynamometer used is a Land & Sea 7" toroidal flow water brake dynamometer. The load on the dynamometer is controlled by load cell that supplies water to the dynamometer from a 5/8" garden hose connection.

Measurements are taken at locations in the system, as illustrated in Figure 91, to calculate the energy going into the motor, and the energy (power) produced by the motor. In particular, the compressed air temperature (ºF), pressure (psi-a) and volumetric flow rate in cubic feet per minute (CFM) is taken before it reaches the pressure regulator. These measurements are used to calculate the air flow through the system in standard cubic feet per minute (SCFM). The air pressure between the pressure regulator and motor is measured so the supply pressure to the motor is known. The motor is connected to a DYNO-mite dynamometer, which applies a controllable load to the motor, and measures the torque and speed. These measurements are used to calculate the power output of the motor in horsepower (hp), as described in Chapter 1. All measurement devices are integrated into the DYNO-mite DAQ system.

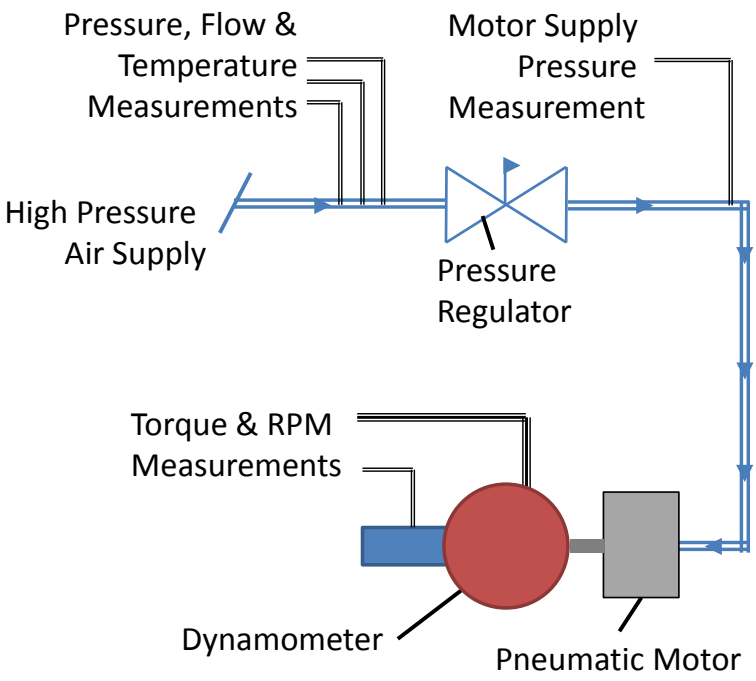

Figure 91 - Schematic showing the experimental setup and measurement system.

A picture of the experimental setup is seen in Figure 92. Detailed compressed air system schematics, measurement system wiring schematics, and calibration reports can be found in Appendix A.

Figure 92 - Engine test setup.

8.2.2 Integration with the Dynamometer Software & DAQ

The dynamometer system uses a custom data acquisition (DAQ) board and integrates with the DYNO-MAX software provided by the dynamometer manufacturer, Land & Sea. The DAQ and software system was used to integrate the custom air flow measurement system with the dynamometer test data. Detailed schematics can be found in Appendix A.

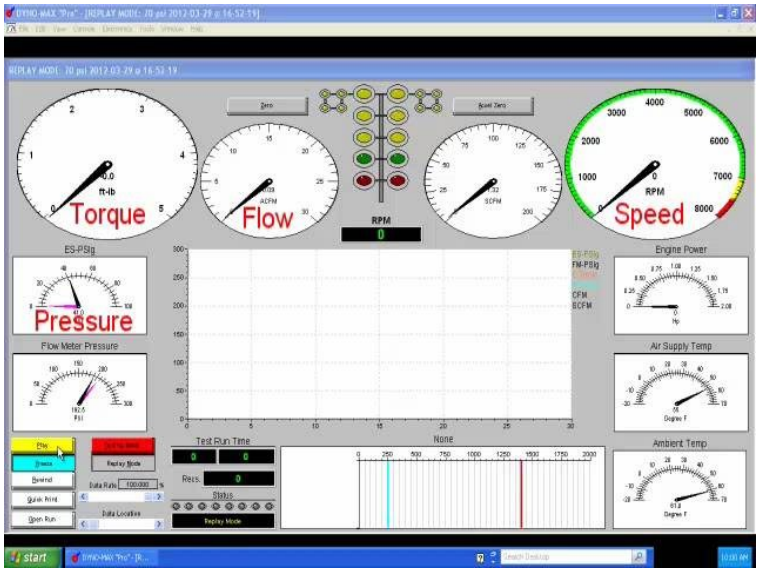

Figure 93 - DYNO-MAX software customized graphical interface highlighting torque, flow, speed, and pressure measurements.

8.3 Test Procedure

Tests were performed for motor supply pressures between 10 and 80 psi at 10 psi increments. An example of a typical time-based torque and speed curve is shown in Figure 94. The motor supply pressure is set after the motor is running by manually adjusting the pressure regulator to the desired pressure, using the digital reading from the dynamometer software. This ensures that the motor supply pressure for each test is within an acceptable range. Once the pressure is set, the startup phase is complete, and the torque and speed data collected is correlated to a specific supply pressure. During this phase, the load on the motor is gradually increased from the minimum load until the motor stalls, or the dynamometer could not output any more torque.

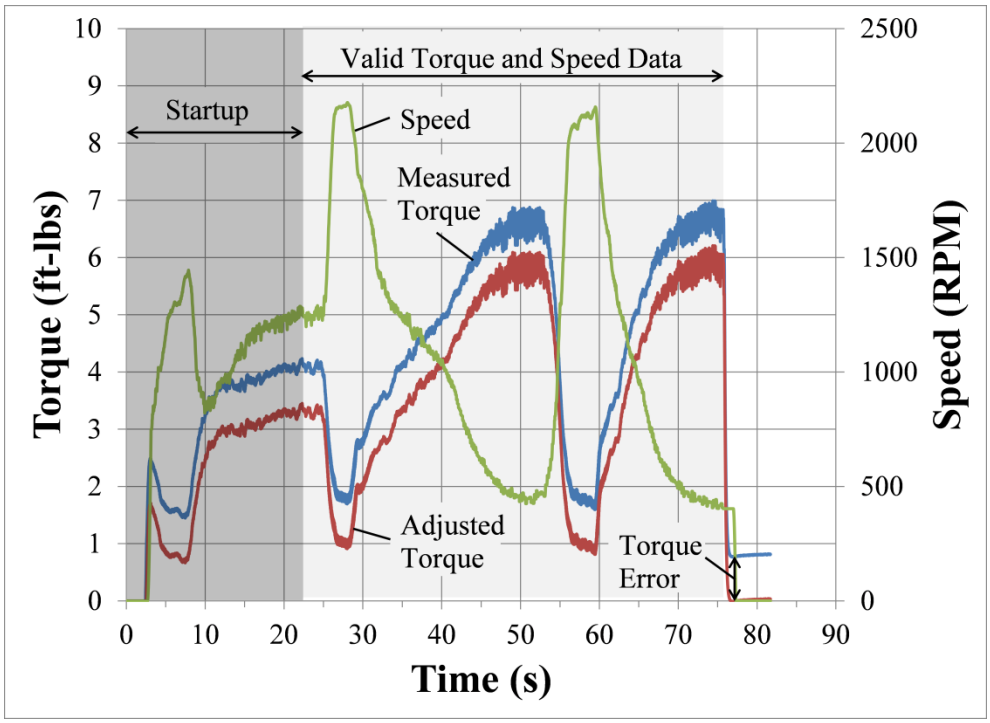

Figure 94 - Illustration of the torque and speed data recorded for a typical motor test, demonstrating the motor speed, measured torque, torque error, adjusted torque, startup phase, and valid data phase.

Figure 94 illustrates the speed and torque data recorded for a typical motor test. It is seen that the test consists of a startup phase, and a usable data phase. The startup phase is from when the test starts to when the motor has reached steady-state after the supply pressure has been set. Once the motor reached a steady-state, the data recorded is valid for the set supply pressure. The data in this range is used to plot the torque versus motor speed.

It is expected that the torque reading return to zero after each test, assuming that there are no external forces on the dynamometer and there are no faults in the torque measurement system. However, as illustrated in Figure 94, the measured torque at the end of the test, after the motor had stopped, did not return to zero. It was found that this is due to the hoses that are connected to the dynamometer, as after the hoses were adjusted to the original state, the torque reading returned to zero. Furthermore, the error in the measured torque reading cannot be neglected in the presented test data. Therefore, for the presented graphs and calculations, adjusted torque measurements are used. In particular, the adjusted torque is calculated as the measured torque, reduced by the static torque measurement after the test had completed (torque error as shown in Figure 94). This

calculation assumes that the torque error is largest at the end of the test. This assumption is justified because the measured torque reading at the beginning of each test is zero, and the error throughout the test is assumed to be somewhere in between the starting torque reading (zero) and the ending torque reading (error). Therefore, given this assumption, the actual torque output from the motor could not be lower than the adjusted value, and a conservative data set is presented.

The valid torque and speed data is processed in order to present the data in a standard method of torque and power versus motor speed. This is done by plotting the torque versus motor speed for each supply pressure, and fitting the data to a linear regression, as shown in Figure 95.

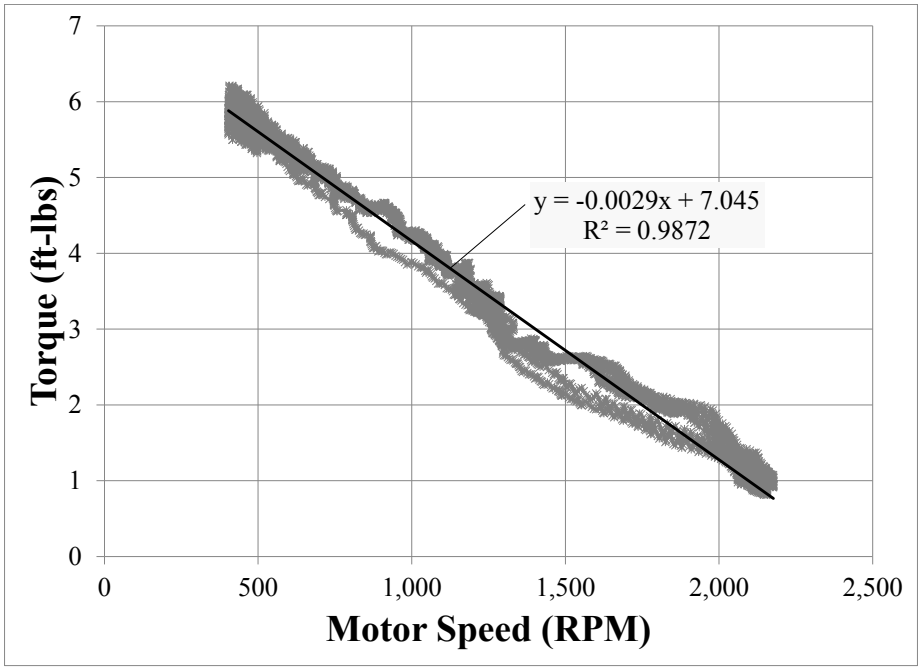

Figure 95 - Typical linear regression of torque versus motor speed showing the equation and R^2 value.

The equations obtained from the linear regression for each supply pressure are used to present the data for the various supply pressures on one chart in the results and discussion. Furthermore, the equations are used to calculate the power from each torque curve. This is the most conservative and certain method of calculating the power, as calculating the power from each data point amplifies the variance from the general trend of the data.

CHAPTER 9 EXPERIMENTAL RESULTS

9.1 Results & Discussion

9.1.1 Measured Pressures and Flow Rates

The average, minimum and maximum measured motor supply pressures are listed below for each nominal supply pressure. There is variance between the nominal pressure and the actual pressure because the system used does not actively control the pressure, rather the pressure is set once with a regulator, and is left for the remainder of the experiment. The nominal supply pressures are listed in the torque and power curves presented.

Table 7 - Measured motor supply pressures and standard deviations for the nominal supply pressures presented.

Nominal Supply Pressure	Average Supply Pressure	Std. Deviation	Minimum Supply Pressure	Maximum Supply Pressure
10	11.1	0.47	10.0	12.3
20	20.4	0.40	19.6	21.7
30	30.4	0.57	28.3	31.5
40	38.9	0.81	37.2	40.7
50	50.5	0.88	48.1	52.5
60	56.9	1.01	54.7	59.7
70	70.2	0.86	67.4	72.7
80	80.5	0.97	77.8	87.6

9.1.2 Torque and Power Curves

The measured torque output of the motor for each supply pressure tested is plotted against motor speed in Figure 96. It is seen that the motor operates at all the tested pressures between 10 and 80 psi, and the torque output increases as the supply pressure increases. This is expected because an increase in pressure in the motor will increase the force acting on the pistons and generate more torque.

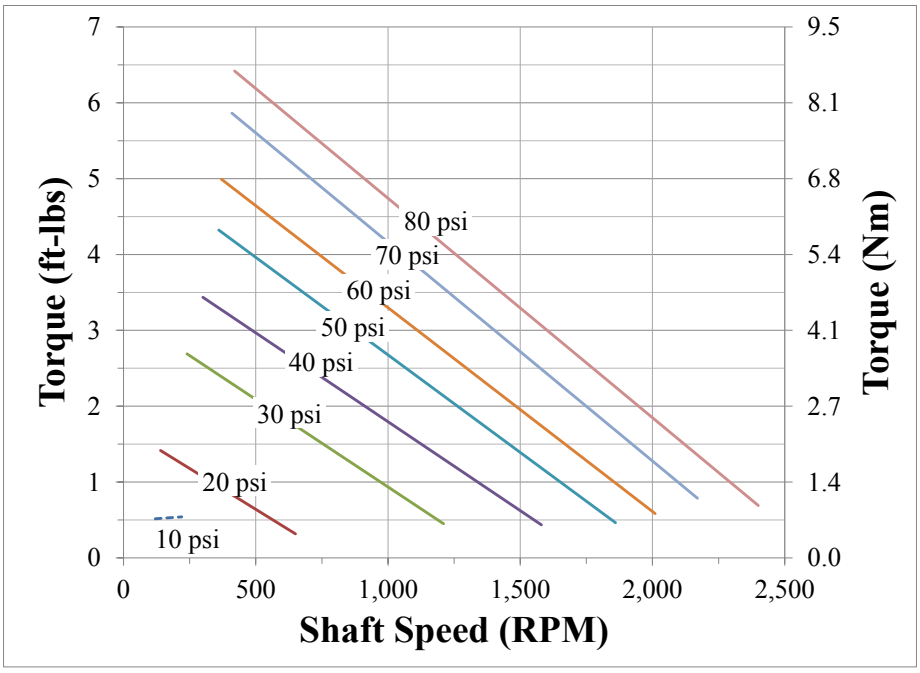

Figure 96 - Measured torque output (ft-lbs left-axis/ Nm right-axis) vs. motor speed (RPM) for supply pressures of 10 to 80 psi in 10 psi increments.

It is seen that the torque data is fit to a linear curve with a relatively high quality fit; with R^2 values above 0.98 for 30 psi and above, and R^2 above 0.90 for 20 psi, as listed in Table 8. This fit is commonly seen in current pneumatic motors, as described in Chapter 1. However, it is seen that the R^2 for 10 psi is well below 0.10, therefore, it cannot be said that the torque data for 10 psi fits a linear trend. Rather, the torque data for 10 psi represents a single operating point at this pressure, thus, this data set is shown with a dashed-line in Figure 96.

It was observed during testing that the dynamometer was unable to stall the motor at pressures of 30 psi and above. Therefore, the stall speeds presented for these data sets are limited by the experimental setup rather than performance of the motor. A further limitation of these experimental results is that the data presented is from a single test series, and not the average of repeated tests. From the methodology, as described in Section 8.3, the torque data presented has been reduced by the torque error at the end of the test. Therefore, the torque and power data presented have been conservatively adjusted by the error in the experimental setup, and it is expected that repeated tests will demonstrate similar or higher torque results with an improved experimental setup. An improved experimental setup should include hoses with minimal stiffness so that the

force imposed on the dynamometer from the hoses is minimized. In addition, the water supply to the dynamometer should be improved to have at least a 0.5 inch unconstructed supply with a ball valve rather than a garden-hose faucet connection, which constricts the flow and was used for the experiments presented in this thesis. Improvement of the water supply is expected to increase the torque load that can be applied by the dynamometer at lower speeds.

Furthermore, it is seen that the range between the minimum and maximum operating speeds increase as the pressure increases. This is generally characteristic of current vane motors. However, the range is not usually as dramatic as seen in the presented data set. This could be advantageous for applications requiring varying torque and speed requirements, where current motors generally have to be sized for a specific range of requirements.

Table 8 - Torque parameters for fit to a linear curve; showing the linear curve parameters a and b for the equation y = ax + b, where y is the torque (ft-lbs) and x is the motor speed (RPM), the R^2 values, minimum and maximum operating speeds, and torque error.

	Pressure							
	10	**20**	**30**	**40**	**50**	**60**	**70**	**80**
a (ft-lbs/rpm)	2.49E-04	-2.15E-03	-2.31E-03	-2.34E-03	-2.57E-03	-2.69E-03	-2.88E-03	-2.89E-03
b (ft-lbs)	0.4859	1.717	3.244	4.139	5.248	5.987	7.045	7.634
r^2	0.0515	0.9047	0.9873	0.9849	0.9805	0.9812	0.9872	0.9881
Min Speed (rpm)	118	135	234	295	351	367	404	420
Max Speed (rpm)	220	657	1218	1585	1862	2017	2177	2400
Torque Error (ft-lbs)	0.583	0.847	0.584	0.619	0.868	1.05	0.783	0.974

The calculated power output of the motor is plotted against motor speed in Figure 97. The power curves are calculated from the linear torque curves shown above. Similar to the torque curves, as the pressure increases, the range of operable speeds broadens and the peak power increases with increased supply pressure.

It is also seen that the peak power occurs at increasing speeds as the motor speed increases. This is generally typical with current vane motors. However, the range is

generally smaller with current vane motors than that presented below. Furthermore, it is seen that the difference between the peak power output and the power output at the minimum and maximum operating speeds increases as the supply pressure increases. This is also generally seen in current vane motors.

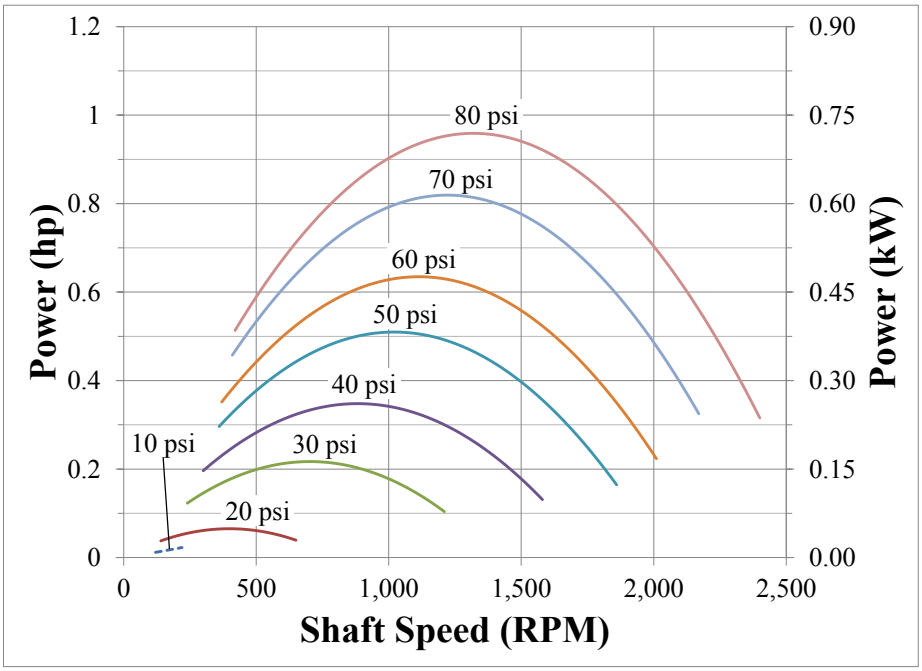

Figure 97 - Calculated power output (hp left-axis / kW right-axis) vs. motor speed (RPM) for supply pressures of 10 to 80 psi in 10 psi increments.

9.1.3 Efficiency

The calculated peak efficiency of the toroidal motor across the tested pressures is seen in Table 9. It is seen that the peak efficiency is generally below 6%, and decreases as the supply pressure decreases. This efficiency is lower than current pneumatic motors, and it is thought that this could be due to the following:

- The port locations and sizes are not optimized. This may restrict the flow of the air through the motor, which could cause power losses. Further the flow of the working fluid within the working chamber is not well understood, and the interaction of the fluid with the pistons may lead to inefficiencies.
- No use of rotor seals causes leakage around the rotors from the working chamber. This loss of fluid flow from the chamber reduces the amount of air that is in the working chamber that can potentially be converted to shaft work. However, rotor

seals will increase the frictional losses of the motor, and there is a tradeoff between the sealing and friction.

- No valves or timing methods control the compressed air input into the motor. Therefore, there is no power produced from the expansion of the air, rather just the flow;
- The aluminum rotors tend to wear and loosen on the sleeves. The internal bore of the rotor is mounted on the mild steel sleeves with a locational tolerance press-fit. It is thought that the cyclic loading and rotation of the rotor causes gradual wear on the surface of the aluminum that is pressed against the steel, and this causes slight misalignment of the rotor. Any slight misalignment of the rotor will generate small gaps around the piston seals, and cause leakages between the cells of the motor.

Table 9 - Motor efficiency (%) and input/ output power vs. supply pressure (psi).

Nominal Supply Pressure	Average Flow Rate (CFM)	Flow Meter Pressure (PSIa)	Average Input Power (hp)	Maximum Output Power (hp)	Peak Efficiency
10	0.93	213	1.9	0.02	1.2%
20	2.00	203	4.7	0.07	1.4%
30	2.86	198	6.4	0.22	3.4%
40	3.62	196	8.0	0.35	4.3%
50	4.56	195	10.0	0.51	5.1%
60	5.03	194	11.0	0.63	5.8%
70	6.39	193	13.8	0.82	5.9%
80	7.42	190	15.8	0.96	6.1%

It is thought that the efficiency decreases with supply pressure because:

- The friction in the rotors may remain relatively constant, independent of the supply pressure, output power, or motor speed (at the tested range);
- Air in the motor has more time to escape out the sides of the chamber for each expansion phase, because the motor is rotating slower at the peak power.

CHAPTER 10 CONCLUSIONS

The primary goal of this thesis and experimentation work was to demonstrate a proof-of-concept of a novel toroidal pneumatic motor. The concept motor has been developed, tested, and proven. However, further development work is required to demonstrate the targeted performance advantages of the motor. Further, secondary goals of this thesis were to demonstrate performance characteristic of the proof-of-concept as a basis for further work. Performance data was presented for the motor, and these results show promising potential for future work on the motor concept. In particular, the motor demonstrates torque output characteristics comparable to current vane motors, and operation at lower than typical-pressures and low shaft speeds. These characteristics present opportunity to improve on systems, such as the rotor seals, to improve the overall performance of the motor.

The development process and work completed demonstrated the complexity of developing and designing a toroidal pneumatic motor. However, it has been found that the critical parts of this type of motor are the impact mechanisms, piston configuration, and the design of the connections between the pistons, impact rings, and rotors. Further, the arrangement of one-way bearings used to transfer torque from the rotors to the drive shaft have been demonstrated to operate as intended for this novel motor application.

The novel motor prototype was designed with minimal custom manufacturing features required. The prototype is constructed with 13 unique components required for the motor, of which 7 are readily available off-the-shelf parts (not including fasteners and screws). Further, these components form an assembly with only 2 rotating parts. However, a retrospective assessment of the cost of manufacturing these motors is difficult at this time, as further design improvements are required, and may be dependent on features required for specific applications.

A FEM model has been developed to optimize the design of the impact rings. The model was qualitatively validated, and used to drive the design of the impact structures. However, further quantitative validation of the model would benefit the ability to use the model as a design tool for future development.

10.1 Design Limitations

A primary limitation of the motor designed and developed are that the motor is unable to expand the working fluid. This greatly limits the potential efficiency of the motor, and it is recommended that future developments include the ability for expansion of the working fluid within the chamber. Further, since the seals between the rotors and the casing have not been included in this design, it is thought that this also limits the efficiency greatly. Therefore, it is recommended that these seals be developed further.

A further limitation, which is a design feature of the prototype tested is that only one compressed air nozzle is used for a four piston motor (where two nozzles could be used). This reduces the amount of working fluid flow that can be introduced to the motor, and limits the power that can potentially be generated at the drive shaft. Further, it is thought that the friction of the rotors is not directly proportional to the supply pressure or flow, as the efficiency increases with increasing pressure and flow. Increasing the number of nozzles in the motor will increase the flow through the motor, and the friction may not increase proportionally. Therefore, the net power that can be converted to shaft work may increase overall.

There are also some operational limitations of the motor, which are inherent to the design. In particular, the motor is non-reversible. The one-way bearings only allow the rotors to rotate in one direction, and reversal of the flow of the working fluid does not reverse the direction of rotation of the drive shaft. Additionally, the rotational speed of the motor is limited by the acceleration of the rotors due to the intermittent rotation and stresses experienced in the impact mechanism. The limits of these are not well known, however it is thought that the motor is best suited for lower speed operation, when compared to turbine and vane motors.

The geometry of the prototype tested has a stator-to-rotor ratio of 0.27. Increasing this ratio will increase the displacement of the motor, which will allow more working fluid to flow through the motor, and potentially allow more power to be generated from the motor. Further, increasing the piston radius increases the displacement of the motor by the square of the piston radius, and increases the circumferential length of the piston seal linearly. Therefore, it is most advantageous to maximize the piston-to-stator radius ratio

in order to maximize displacement, and minimize the length of the seals, which generate friction. However, increasing the piston diameter will increase the force acting on the pistons, and therefore generate more extensive design requirements for the components connecting the piston to the rotor, and the other torque transferring components such as the one-way bearings.

The maximum pressure that was tested on the motor was 80 psi. It was found that pressures above this stressed the components such as the connection between the piston and the rotor beyond the strength of the component. However, it is thought that improved designs and higher strength materials could be used to overcome this limitation to be used with higher pressures.

It is thought that the Aluminum 6061-T6, although lightweight, is not a suitable material for the casing geometry because the material is not very hard or durable, and it was observed that the quality of the surface finish on the toroidal fillets on the chamber and rotors diminished.

10.2 Future Work

It is recommended that future work be focused on improving the efficiency of the motor. A critical part of this work is further characterization and theoretical understanding of the limits of the components of the motor. This will allow design trade-offs that were introduced, such as the piston diameter, and strength of the fastening components between the pistons and the rotors to be better understood.

Improvements to the experimental setup should be made to minimize the influence of the hoses on the dynamometer torque reading, and testing should be done to show the repeatability of the performance of the motor.

Further, development of components such as the rotor seals and timing systems should be focused on to improve the efficiency of the motor. Research should be conducted on finding applications where low pressure motor operation is advantageous, and component development should be focused on improving the performance of the motor for these applications. Studies should be conducted to optimize material selection for the motor components for specific applications.

REFERENCES

1. **Deprag Schulz GmbH.** *Air Motors.* [Online] 2012. [Cited: 04 13, 2012.] http://www.deprag.com/download/prospekt-pdf/D6000en.pdf.

2. **TDI Tech Development.** *TDI Turbo Twin - Air starters for Marine Applications.* [Online] 2012. [Cited: May 29, 2012.] http://www.tdi-turbotwin.com/pdfs/TDI%20Marine%20Cat_7-14-11.pdf.

3. **Taylor, D.A.** *Introduction to Marine Engineering.* 2nd Ed. s.l. : Elsevier, 1996.

4. *New model of a pneumatic dental drill.* **Kostyleva, S., Zhilina, V.** 4, s.l. : Springer New York, 07 1968, Biomedical Engineering, Vol. 2.

5. **Beater, Peter.** Air Motors and Turbines. *Pneumatic Drives - System Design, Modelling and Control.* s.l. : Springer, 2007, pp. 151-152.

6. **Pinches, M.J., Callear, B.J.** *Power Pneumatics.* Hertfordshire : Prentice Hall Europe, 1996.

7. **Beater, Peter.** Vane Motors. *Pneumatic Drives - System Design, Modelling and Control.* s.l. : Springer, 2007, pp. 153-155.

8. **Apex Tool Group, LLC.** *Cleco Pneumatic Power Motors.* [Online] 2010. [Cited: Sep 17, 2012.] http://www.apexpowertools.com/catalog/pdffiles/SP-104_EN.pdf.

9. **Basshuysen R., Schafer F.** *Modern Engine Technology, from A to Z.* Warrendale : SAE International, 2007.

10. **Akers A., Grassman M., Smith R.** *Hydraulic Power Systems Analysis.* s.l. : CRC Press, 2006.

11. **Beater, Peter.** Air Turbines. *Pneumatic Drives - System Design, Modelling and Control.* London : Springer, 2007, pp. 168-170.

12. **Dixon, S.L.** *Fluid Mechanics, Thermodynamics of Turbomachinery.* [ed.] J. Stein. 5th. Burlington : Elsevier Butterworth-Heinemann, 1998.

13. *An analytical and experimental study of rotary vane turbomachinery: single-phase working fluids.* **Mahdizadeh A., Mahmoud A.M., Sherif S.A., Lear W.E.** Jacksonville, FL : s.n., 2008. 2008 ASME Fluids Engineering Conference. pp. 235-242.

14. *Power Assessment of Flowing Compressed Air.* **Cai, M., Kawashima, K., Toshiharu K.** 402, March 2006, Journal of Fluids Engineering, Vol. 128.

15. *Design Optimization and Efficiency Modeling of a Hot Gas Vane Motor.* **Bommarito G. E., Fales R.** Seattle, Washington : s.n., 2007. ASME International Mechanical Engineering Congress and Exposition. pp. 59-68.

16. *A Model of Contact Forces in Pneumatic Motor Vanes.* **Bertetto A. M., Mazza L., Pastorelli S., Raparelli T.** 36, 2001, Meccanica, pp. 691-700.

17. **Beater, Peter.** Matematical Model. *Pneumatic Drives.* New York : Springer, 2007, pp. 156-157.

18. *A new pneumatic vanes motor.* **Naranjo J. Kussul E., Ascanio G.** 20, 2010, Mechatronics.

19. **Dubois, Virgil L.** *Fluid Pump or Motor. 2,311,162* US, May 20, 1940.

20. *Multi-Vane Expanders: Vane Dynamics and Friction Losses.* **Badr, O., Probert, S.D., O'Callaghan, P.** 20, 1985, Applied Energy.

21. **Parr, Andrew.** Rotary Actuators. *Hydraulics and Pneumatics - A Technicician's and Engineers Guide.* s.l. : Elsevier, 2011, pp. 1330-134.

22. *Multi-Vane Expanders: Internal-Leakage Losses.* **Badr, O., Probert, S.D., O'Callaghan, P.W.** 20, 1985, Applied Energy.

23. *Multi-vane expanders: Geometry and Vane Kinematics.* **Badr, O., O'Callaghan, P.W., Probert. S.D.** 19, 1985, Applied Energy, pp. 159-182.

24. *Cepstral Analysis for the Recovery of Apex Seal Interaction Forces in Rotary Engines.* **Britton, J. D.** Detroit, Michigan : SAE, 1991. SAE International Congress and Exposition. SAE Technical Paper 910705.

25. *Force Analysis of the Apex Seals in the Wankel Rotary Compressor Including the Influence of Fluctuations in the Crankshaft Speed.* **Pennock, G. R. and Beard, J. E.** 3, 1997, Mechanism and Machine Theory, Vol. 32. doi:10.1016/S0094-114X(96)00051-1.

26. **Hehn, A.H.** *Fluid power troubleshooting.* 2nd. New York : Marcel Dekker, Inc., 1995.

27. **Barrera, R. M. and Barrera, R. A.** *Rotary Engine. 6341590* January 29, 2002. U.S. Patent.

28. **Farb, N.E.** *Internal Combustion Engine. 3251347* May 17, 1966. U.S. Patent.

29. **Bergen, H.** *Toroidal Cylinder Orbiting Piston Engine. 3 937 187* February 10, 1976. U.S. Patent.

30. **Cronen, P.J.** *Toroidal Rotary Engine. 4 035 111* July 12, 1977. U.S. Patent.

31. **Buchstaber V.M., Panov T.E.** *Torus actions and their applications in topology and combinatorics.* Providence : American Mathematical Society, 2002.

32. **Morgado, R. G.** *Internal Combustion Engine and Method. 6 739 307 B2* May 25, 2004. U.S. Patent.

33. **Jones, Barry M.** *Granville Bradshaw: A flawed genious?* Buckinghamshire : Panther Publishing Ltd., 2008. 978-0-9556595-4-6.

34. **Flitney, R.** *Seals and Sealing Handbook.* s.l. : Elsevier, 2007. pp. 105-357. ISBN 978-0-08-054926-2.

35. **Boljanovic, Vukota.** Geometry. *Applied Mathematical and Physical Formulas - Pocket Reference.* New York : Industrial Press, 2007, pp. 111-112.

36. **Free, P.D.** *Rotary Engine. 6 289 867 B1* September 18, 2001. U.S. Patent.

37. *Variable inertia effects of an engine including piston friction and a crank or gudgeon pin offset.* **Guzzomi, A. L., Hesterman, D. C. and Stone, B. J.** 3, 2008, Journal of Automobile Engineering, Vol. 222. doi:10.1243/09544070JAUTO590.

38. *Model for simulating the instantaneous crank kinematics and total mechanical losses in a multicyliner in-line engine.* **Potenza, R., et al., et al.** 4, 2007, International Journal of Engine Research, Vol. 8. doi:10.1243/14680874JER00507.

39. *Analysis of piston secondary motion considering the variation in the system inertia.* **Zhang, Z., et al., et al.** 4, 2009, Journal of Automobile Engineering, Vol. 223. doi:10.1243/09544070JAUTO1078.

40. *Rotary Engines.* **Chinitz, Wallace.** 2, s.l. : Scientific American, 1969, Vol. 220, pp. 90-99. ISSN 0036-8733.

41. *Rotary engines – a concept review.* **Thompson, G. J., Wowczuk, Z. S. and Smith, J. E.** 2003, SAE Technical Paper, Vol. 01. 2003-01-3206.

42. **Kuchnicki, T. A.** *Gas Rotary Engine Technology Development.* San Antonio, TX : Southwest Research Institute, 1990. SwRI-3458.

43. **Krikorian, M.A.** *Rotary Engine. 1 212 649* January 16, 1917. U.S. Patent.

44. **Farrel, M.** *Oscillating Piston Engine. 5 222 463* CA, June 29, 1993.

45. **Pekau, R.R.** *Toroidal Engine with Variable Displacement Volume. 7 341 041 B2* March 11, 2008. U.S. Patent.

46. **Wright, M.D.** *Orbital Engine. 7 059 294 B2* June 13, 2006. U.S. Patent.

47. **Kypreos-Pantazis, G.** *Internal Combustion Engine Having Rotating Pistons. 4 683 852* August 4, 1987. U.S. Patent.

48. **Adamovski, V.I.** *Toroidal Internal Combustion Engine. 5 737 366* August 25, 1998. U.S. Patent.

49. **Yi, C.S.** *Rotary Internal Combustion Engine. 5046465* September 10, 1991. U.S. Patent.

50. **Wohl, S.M.** *Toroidal Sweep Engine. 4 137 890* February 6, 1979. U.S. Patent.

51. *Scuderi split-cycle engine prototype debuts.* **SCUDERI Group LLC.** 11, Detroit : Machine Design, 4 6, 2009, Vol. 81. 42204399.

52. **Vincent, O.W.** *Rotary Engine with a Round Toroidal Cylinder and Pistons. 5 242 288* September 7, 1993. U.S. Patent.

53. **Sabin, D.B.** *Rotary Toroidal Machine with Piston Connecting Mechanism. 7 305 937* December 11, 2007. U.S. Patent.

54. **Barrera, R. M. and Barrera, R. A.** *Rotary Engine. 6 341 590 B1* January 29, 2002. U.S. Patent.

55. **Hoose, K. V.** *Toroidal Internal Combustion Engine. 6 880 494 B2* United States of America, April 19, 2005. U.S. Patent.

56. **Hoyt, S. W.** *Combustion Engine. 6 386 838 B2* United States of America, May 14, 2002. U.S. Patent.

57. **McMaster, H. A.** *Rotary Engines. 3 595 014* United States of America, July 27, 1971. U.S. Patent.

58. **Nutku, A.** *Toroidal Chamber Rotating Piston Engine. 3 909 162* September 30, 1975. U.S. Patent.

59. **Rigternick, D.L.** *Radial Torque Internal Combustion Engine. 4 212 271* July 15, 1980. U.S. Patent.

60. **Farb, N.E.** *Internal Combustion Engine. 3 251 347* May 17, 1966. U.S. Patent.

61. **Chevalllier, M. and Poulain, G.** *Valveless Internal Combustion Engine. 1 790 534* January 27, 1931. U.S. Patent.

62. **Potter, M.C.** *Internal Combustion Engines. 3 186 383* June 1, 1965. U.S. Patent.

63. **Rubinshtein, B.** *Rotary Internal Combustion Engine. 4 319 551* March 16, 1982. U.S. Patent.

64. **Kovalenko, G.E.** *Toroidal Internal Combustion Engine. 5 199 391* April 6, 1993. U.S. Patent.

65. **Sakita, M.** *Rotary Piston Engine. 5 381 766* January 17, 1995. U.S. Patent.

66. —. *Rotary Piston Engine. 6 457 451 B1* October 1, 2002. U.S. Patent.

67. —. *Rotary Piston Engine. 7 814 882 B2* Oct. 19, 2010.

68. **Arov, A.** *Orbital Engine/ Pump With Multiple Toroidal Cylinders. 7 631 632* Dec 15, 2009.

69. **Ball, W. and Rõnnberg, P.** *Rotary Piston Internal Combustion Engine. 5 740 765* April 21, 1998. U.S. Patent.

70. **Kovalenko, V. I.** *Rotary Internal Combustion Engine. 7 255 086 B2* August 14, 2007. U.S. Patent.

71. **Silvoza, E.P.** *Rotary Engine Having Controller and Transfer Gears. 4 738 235* April 19, 1988. U.S. Patent.

72. **Stoughton, D.R.** *Rotary Opposed Piston Engine. 6 895 922 B1* May 24, 2005. U.S. Patent.

73. **Kurisu, M.** *Cat and Mouse Type Rotary DEvice Utilizing Grooves and Rods for Power Converyance. 6 422 841 B2* July 23, 2002. U.S. Patent.

74. **Richards, R.L.** *Rotary Internal Combustion Engine. 6 371 743 B1* April 16, 2002. U.S. Patent.

75. **Larrea, C.A.** *Rotary Cycloidal Continuous Toroidal Chamber Internal Combustion Engine. 4 026 249* May 31, 1977. U.S. Patent.

76. **Stromberg, O.E.E.** *Rotary Engine. 1 973 397* September 11, 1929. U.S. Patent.

77. **Larrea, C.A.** *Rotary Cycloidal Continuous Toroidal Chamber Internal Combustion Engine. 4026249* May 31, 1977. U.S. Patent.

78. **Bergen, H.** *Toroidal Cylinder Orbiting Piston Engine. 3937187* February 10, 1976. U.S. Patent.

79. **Stromberg, O.E.E.** *Rotary Engine. 1973397* September 11, 1929. U.S. Patent.

80. **Dickey, B., Krajewski, A., Martakoush, A., Murphy, B., Pelletier, J. F.** *Group 10: Rotational Impact Internal Combustion Engine, Winterl Term Final Report.* Mechanical Engineering, Dalhousie University. Halifax. NS : s.n., April 2010.

81. **Livermore Software Technology Corporation.** LS-DYNA Keyword User's Manual Version 971. Livermore : Livermore Software Technology Corporation, 2007.

82. *A Constitutive model and data for metals subjected to large strains, high strain rates and high temperatures.* **Johnson, G.R., Cook, W.H.** 1983. Preceedings of the 7th International Symposium.

APPENDIX A - TESTING SCHEMATICS & EQUIPMENT SPECIFICATIONS

Compressed Air Supply System and Air Flow Measurement System Schematics

DWG #	Description
MEP 101	High Pressure Cylinder Bank Pipework and Manifold Schematic
MEP 102	High Pressure Regulator Pipework Schematic
MEP 103	Air Flow Measurement System and Dynamometer Wiring System Schemaitc

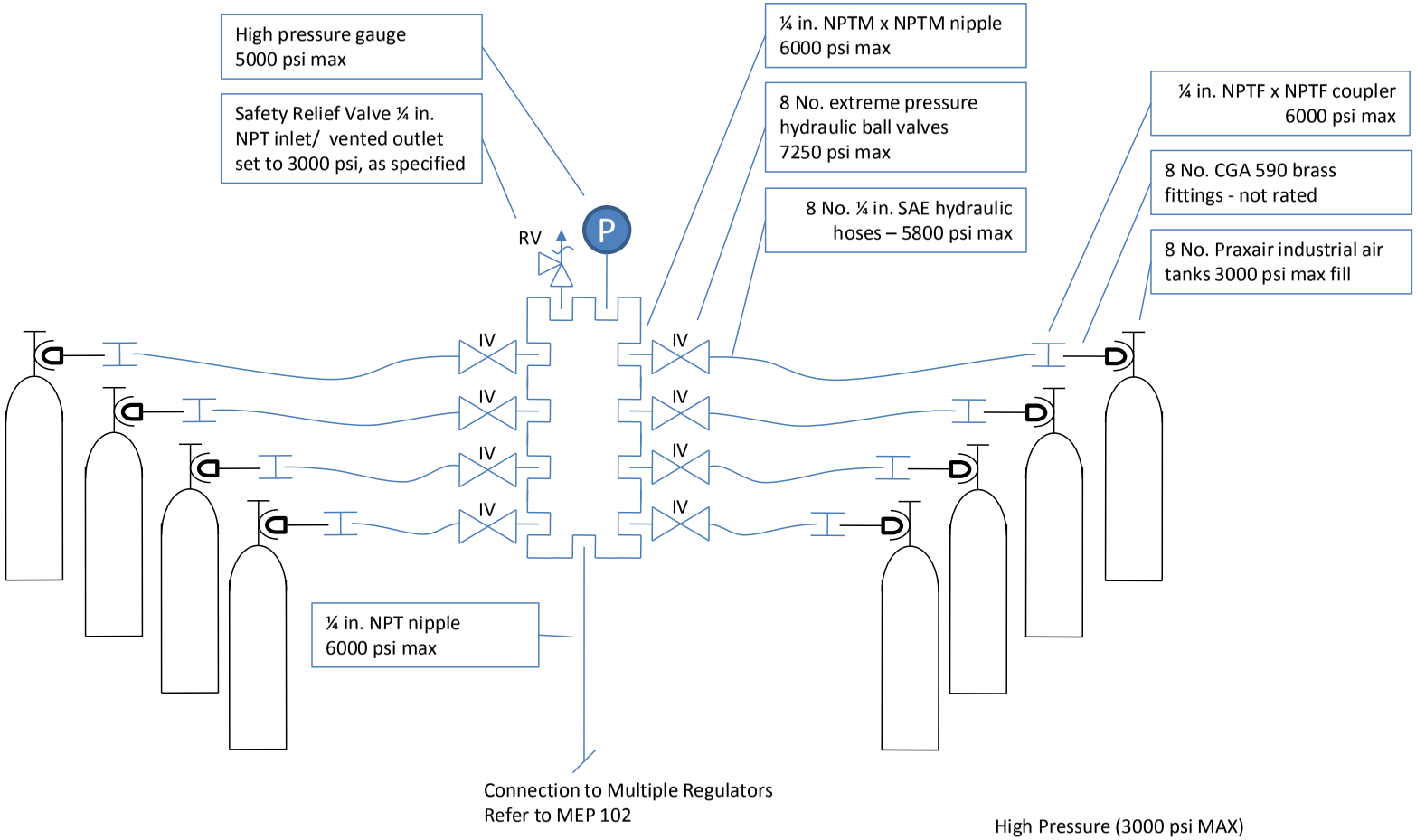

MEP 101
High Pressure Cylinder Bank
Pipework & Manifold Schematic
B Murphy
Aug 10 20101

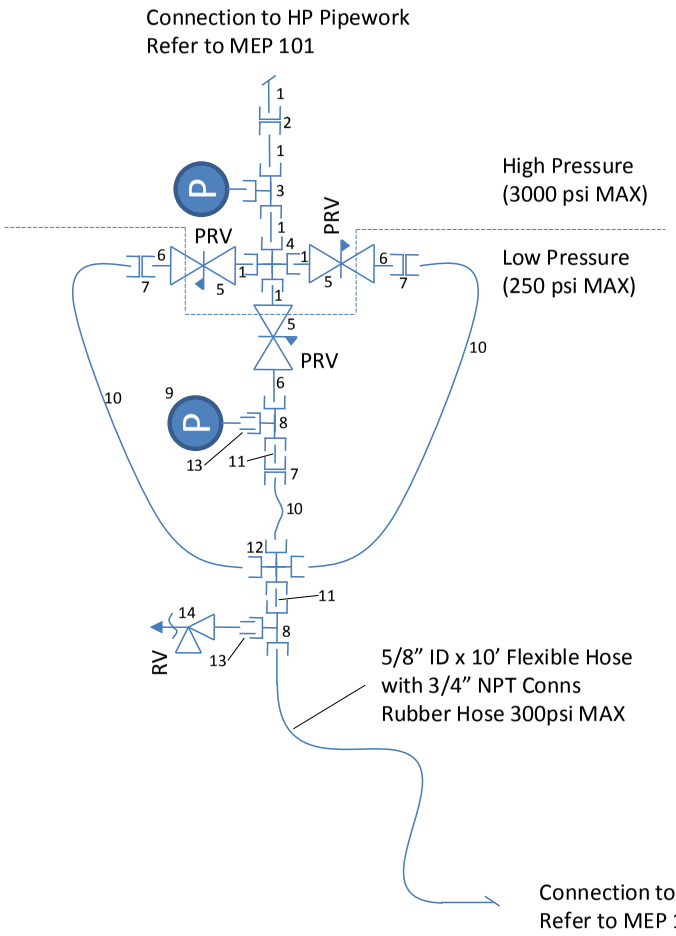

Bill of Materials for Multiple Regulator Pipework Modifications

	Item No.	Quantity	Description
High Pressure (3000 psi)	**1**	6	1/4 in. NPT Nipple
	2	1	1/4 in. NPT-F Union
	3	1	1/4 in. NPT-M Tee
	4	1	1/4 in. NPT-M Cross
	5	3	1/4 in. NPT-M High Pressure Regulator (250 psi max output)
Low Pressure (250 psi)	**6**	3	1/4 in. x 3/4 in. NPT Reducing Nipple
	7	3	3/4 in. NPT-F Union
	8	2	3/4 in. NPT-F Tee
	9	1	1/4 in. Low Pressure Gauge
	10	3	3/4 in. NPT-M x 2.5 ft. Hose
	11	2	3/4 in. NPT Nipple
	12	1	3/4 in. NPT-F Cross
	13	2	1/4 x 3/4 in. NPT Bushing
	14	1	¼ in. NPT-M Pressure Relief Valve Set to 250 psi

MEP 102
High Pressure Regulator
Pipework Schematic
B Murphy
May 18, 2011

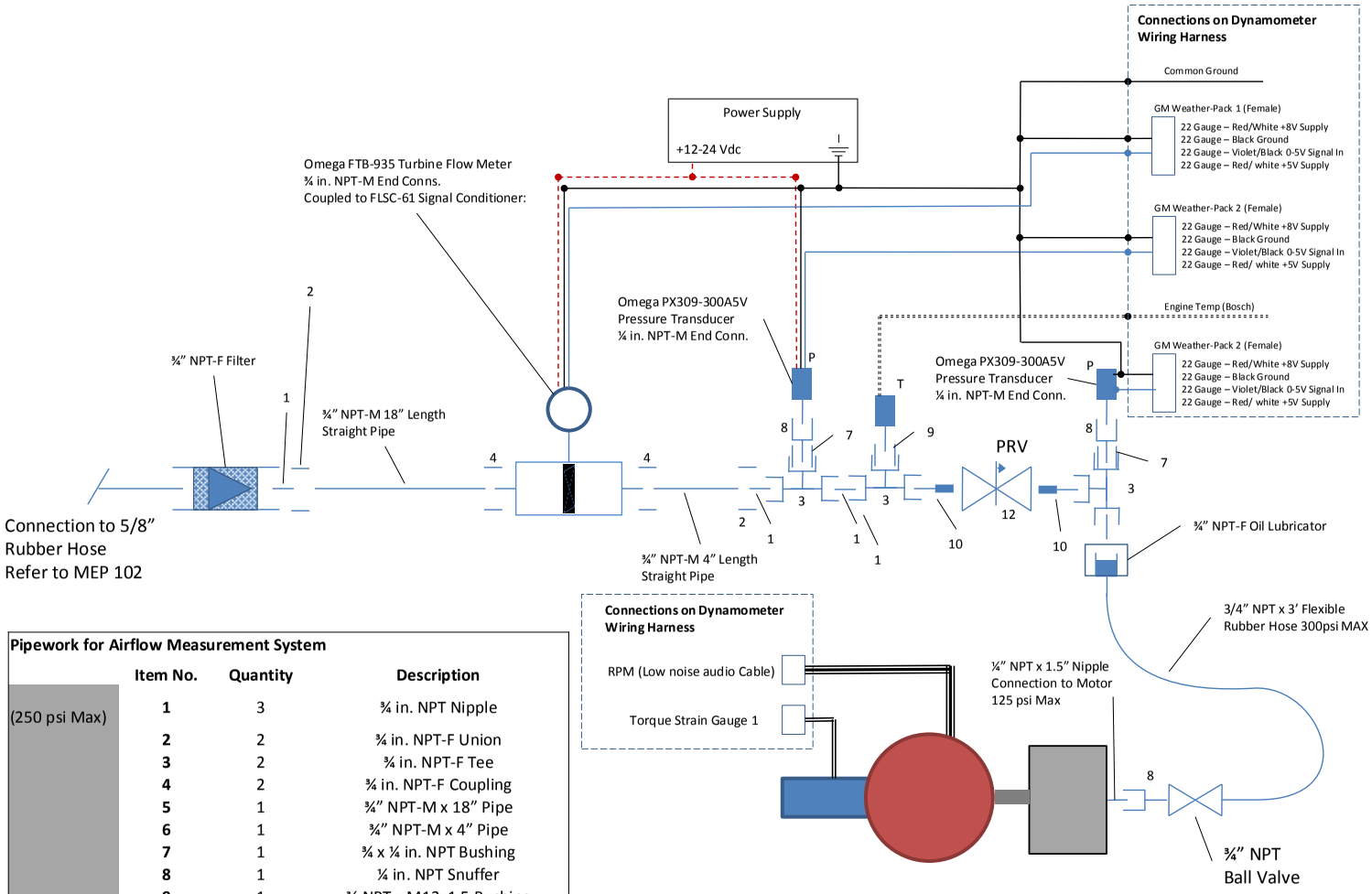

Pipework for Airflow Measurement System

	Item No.	Quantity	Description
(250 psi Max)	**1**	3	¾ in. NPT Nipple
	2	2	¾ in. NPT-F Union
	3	2	¾ in. NPT-F Tee
	4	2	¾ in. NPT-F Coupling
	5	1	¾" NPT-M x 18" Pipe
	6	1	¾" NPT-M x 4" Pipe
	7	1	¾ x ¼ in. NPT Bushing
	8	1	¼ in. NPT Snuffer
	9	1	¾ NPT x M12x1.5 Bushing
	10	2	¾ x 1 in. NPT Nipple
	11	1	Omega FTB-935 Flowmeter & FLSC-61 Signal Conditioner
	12	1	1 in. NPT-F Wilkerson Regulator

MEP 103
Air Flow Measurement System and Dynamometer Wiring Schematic
B Murphy
May 18, 2011

Measurement Equipment Calibration Reports

Omega FTB-935 Flow Meter Calibration Report

WORK ORDER # 458726

Calibration Report
Omega Engineering
One Omega Drive
Stamford, CT 06907-0047
USA

TF0029

Calibration :	1	Weight(Lbs):	35.0	Serial # :	280206
Fluid :	WATER	Volume Sp. Gr. 1.000		Housing Material :	SS-304
Test Stand # :	IE1004	(Gallons Water):	4.19870680	Rotor Material :	17-4
Calib. By :	MH	Model #		Bearings :	METAL
Calib. Date :	03/07/11	FTB-935		Coil # : SC24-45G	(1EA.)

PT.	(TRUE) SP.GR.	TEMP. DEG.FAR.	TRUE VOL. ACF	RATE ACFM	TIME SECONDS	TOTAL PULSES	APPROX. FREQ.HZ.	"K" ACF	
1	0.9977	72.6	0.562563	28.825573	1.171	1956	1670.4159	3476.9458	
2	0.9977	72.6	0.562560	22.359936	1.510	1956	1295.7446	3476.9632	
3	0.9977	72.6	0.562557	15.790726	2.138	1955	914.5996	3475.2030	
4	0.9977	72.5	0.562554	9.143870	3.691	1955	529.6166	3475.2239	
5	0.9977	72.5	0.562555	2.553609	13.218	1914	144.8039	3402.3352	X

MEAN TOTAL PULSES (PER WEIGHT USED):	1955.50
SENSING ELEMENT CONSTANT (MEAN "K"):	3476.0840

Remarks:

Range Bars: +/-1.00%

Conversion Details: ACF (Volumetric Air Equiv)
Air

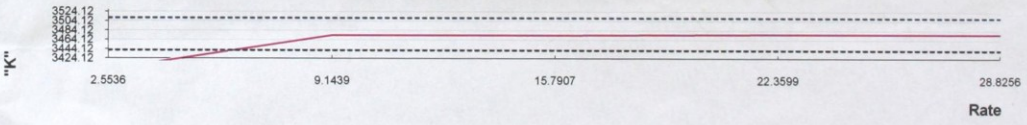

The above mentioned item has ben calibrated with measurement and test equipment traceable to NIST. Uncertainties are available upon request

NIST Traceable Standards

Test Stand Number IE1004 Cal Due Date: 3-2011 Scale Serial Number 101658 Cal Due Date: 6-2011

n outside meter accuracy, not included in mean pulses or sensing element constant.

CALIBRATED BY: [redacted]

CERTIFIED BY:

DATE: 03/07/11 Form Rev: 1.5.1

Omega FLSC-61 Signal Conditioner Calibration Report

Braden A. Murphy
FLSC-61 Signal Conditioner Calibration Report

Power Supply Voltage: 11.95 V VDC (12-35V)

Select Full Scale Frequency Range:

JU1 @ 1.875-10 kHz
JU2 @ 350-1950 Hz x
JU3 @ 75-375 Hz

Input signal
Waveform: SINE
Amplitude: 100mV
0% FS output: 0 V DC

Turbine Calibration

Flow	Freq. Output (Hz)
2.553609	144.8039
9.14387	529.6166
15.790726	914.5996
22.359936	1295.7446
28.825573	1670.4159

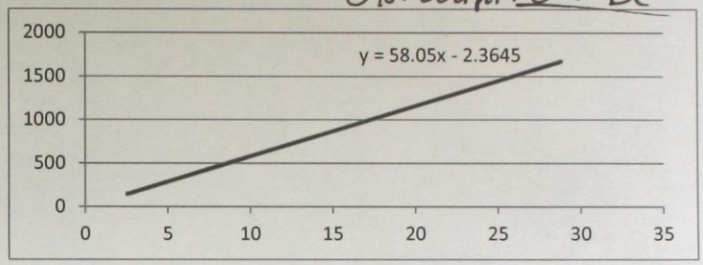

% of FS Input Freq.	Flow Rate (CFM)	Input Freq. (Hz)	Required Output (VDC)	Actual Imput Freq. (Hz)	Output - Computer (VDC)	Output - Multimeter (VDC)
0%	0.0	0.0	0	0.000	0.016	0.000
25%	7.0	404.0	1.25	403.5	1.240	1.21
50%	14.0	810.3	2.5	819.1	2.581	2.50
75%	21.0	1216.7	3.75	1205	3.814	3.78
100%	28.0	1623.0	5	1620	4.999V	5.05V

Name: [redacted]

Date: Jan 31, 2012.

Pre-Test Calibration Check Data

Test	Date	Torque Computer Readout (ft-lbs)	Flow Meter Pressure (psi-g)		Engine Supply Pressure (psi-g)		Ambient Air Temperature		Flow Meter Temperature (°F)
			Computer	Gauge	Computer	Gauge	Computer (°F)	Gauge (°C)	Computer
Sensor Check	Mar 29, 2012	0	0	0	0	0	62	15	58
40 psi Supply	Mar 29, 2012	0	196	200	21.5	22	62	15	58
60 psi supply	Mar 29, 2012	0	198	210	38.7	38	62	15	56
50 psi supply	Mar 29, 2012	0	194	200	53.6	52	61	15	48
30 psi supply	Mar 29, 2012	0	201	205	43.4	42	61	15	45
20 psi supply	Mar 29, 2012	0	203	205	37.5	38	62	15	44
10 psi supply	Mar 29, 2012	0	206	210	27.4	28	63	15	44
70 psi supply	Mar 29, 2012	0	196	200	40.9	40	61	14	55
80 psi supply	Mar 29, 2012	0	201	205	48.1	47	62	14	49

APPENDIX B - AIR MOTOR PERFORMANCE DATA

The figures presented in Section 2.1 of Chapter 1 were synthesized from the data collected from manufacturer's product literature. Manufacturers were selected based on the level of detail presented in the literature, and in-order to be included in the review, must have presented standard torque and power curves, mass, supplied air pressure, and air flow rate. Further, at least two (2) different manufactures products were used for each motor type (vane, turbine, etc.). The manufacturers, models, and summery data are listed below. Calculated available power (power in the compressed air supplied to the motor) is calculated using the methods described as described in Section 2.1. The sources below refer to the manufactures catalogues for the references listed in the table below.

[1] Cleco. Apex Power Tools. [Online]. 2010 cited 2012 Sep 17. Available from: http://www.apexpowertools.com/catalog/pdffiles/SP-104_EN.pdf.

[2] Parker Hannifin. Pneumatic Rotary Actuators & Airmotors. [Online].; 2011 cited Apr 18, 2012. Available from: http://www.parker.com/portal/site/PARKER/menuitem.223a4a3cce02eb6315731910237ad1ca/?vgnextoid=062eeea74775e210VgnVCM10000048021dacRCRD&vgnextfmt=EN

[3] Austart Air Starters. ATS63 and ATS 103 Series. [Online]. 2003 cited 2012 May 29. Available from: http://austartairstarters.com/ATS63 Data.pdf and http://austartairstarters.com/ATS103 Data.pdf

[4] TDI Tech Development. TDI Turbo Twin - Air starters for Marine Applications. [Online].; 2012 cited 2012 May 29. Available from: http://www.tdi-turbotwin.com/pdfs/TDI%20Marine%20Cat_7-14-11.pdf.

[5] Atlas Copco. Atlas Copco Air Motors. [Online]. 2010 cited 2012 Apr 18. Available from: http://194.132.104.143/websites/tools/Publications/acc11.nsf/va_TechLang/54C82BC5A9038B0DC1256BA6004FA1FB/$File/Atlas_Copco_Air_Motors_UK.pdf?OpenElement

[6] Gast (Idex Corp). Air Motors/ Gear Motors. [Online]. 2012 cited 2012 Apr 20. Available from: http://www.gastmfg.com/catalogs/Airmotor_D-10_Catalog_Final_Feb09-2012_lo-res.pdf

Motor Type	Make and Model	Mass (kgs)	Rated Power (kW)	Speed at Rated Power (rpm)	Torque at Rated Power (Nm)	Air Consumption (l/s)	Tested Supply Pressure (psi)	Tested Supply Pressure (kPa)	Calculated Available Power (kW)	Calculated Efficiency	Reference
Piston - Axial	Cleco A8R309M	17.2	2.01	1300	14.8	53	100	690	11.0	18.2%	[1]
Piston - Radial	Cleco MA3S358M	22.2	2.24	1300	16.5	42.5	90	621	8.4	26.5%	[1]
Piston - Radial	Cleco MMS396M	95.3	11.19	1070	99.9	164.3	90	621	32.6	34.3%	[1]
Piston - Radial	Parker P1V-P007A02200	1.5	0.07	1100	0.6	3.3	74	507	0.6	12.1%	[2]
Piston - Radial	Parker P1V-P023A01500	4.6	0.23	750	2.9	6.67	74	507	1.2	18.9%	[2]
Turbine - Geared	Austart Turbine Starters ATS63	7.5	7.46	4500	68.0	132	100	690	27.5	27.2%	[3]
Turbine - Geared	Austart Turbine Starters ATS103	20.0	44.76	4600	361	519	100	690	107.8	41.5%	[3]
Turbine - Geared	TDI Marine T20 13:1 Gear Reducer	8.2	4.50	2500	40.7	96	90	621	19.1	23.5%	[4]
Turbine - Geared	TDI Marine T112-V 9.25:1 Gear Reducer	23.0	47.00	2000	224.0	758	90	621	150.5	31.2%	[4]
Vane	Atlas Copco LZL 03 S	2.9	1.05	5300	1.9	29.0	90	621	5.8	18.2%	[5]
Vane	Atlas Copco LZL 35 8411 1005 74	20.0	5.20	2500	20.0	130	90	621	25.8	20.1%	[5]
Vane	GAST 1AM	0.9	0.45	8000	0.3	9.8	100	690	2.0	22.2%	[6]
Vane	GAST 16 AM	32.4	7.00	2000	34.0	131.9	100	690	27.4	25.5%	[6]
Vane - Geared	GAST 1AM-NRV	2.3	0.26	350	7.1	10.0	100	690	2.1	12.5%	[6]
Vane - Geared	GAST 16AM-13	73.4	4.85	100	478.1	130	100	690	27.0	18.0%	[6]

APPENDIX C – IMPACT RING FEM MODEL CODE

```
*KEYWORD_ID 80000000 NCPU=4
$---+----1----+----2----+----3----+----4----+----5----+----6----+----7----+----8
$ PROJECT           NUM
zresultz 4mm Pad 0pt76mm spacing
*TITLE
4mm Pad 0pt76mm clearance
$
$
$---+----1----+----2----+----3----+----4----+----5----+----6----+----7----+----8
$                                                                               $
$                                  CONTROL CARD                                 $
$                                                                               $
$---+----1----+----2----+----3----+----4----+----5----+----6----+----7----+----8
*CONTROL_TIMESTEP
$---+----1----+----2----+----3----+----4----+----5----+----6----+----7----+----8
$   DTINIT    TSSFAC      ISDO    TSLIMT     DT2MS      LCTM     ERODE     MS1ST
       0.0      0.75
$---+----1----+----2----+----3
$   DT2MSF   DT2MSLC     IMSCL

$
$
*CONTROL_TERMINATION
$---+----1----+----2----+----3----+----4----+----5
$   ENDTIM    ENDCYC     DTMIN    ENDENG    ENDMAS
    0.0004         0       0.0       0.0       0.0
$
$
*CONTROL_ENERGY
$---+----1----+----2----+----3----+----4
$     HGEN      RWEN    SLNTEN     RYLEN
         1         1         1         1
$
$
$*CONTROL_HOURGLASS
$---+----1----+----2
$      IHQ        QH
$        1     0.100
$
$
$---+----1----+----2----+----3----+----4----+----5----+----6----+----7----+----8
$                                                                               $
$                           DATABASE CONTROL FOR BINARY                         $
$                                                                               $
$---+----1----+----2----+----3----+----4----+----5----+----6----+----7----+----8
*DATABASE_BINARY_D3PLOT
$---+----1----+----2----+----3----+----4
$  DT/CYCL      LCDT      BEAM     NPLTC
  0.000001         0         0         0
$---+----1
$    IOOPT
         0
$
$
*DATABASE_GLSTAT
$---+----1----+----2
$       DT    BINARY
  0.000001         1
$
$
*DATABASE_MATSUM
$---+----1----+----2
$       DT    BINARY
  0.000001         1
$
*DATABASE_RBDOUT
$---+----1----+----2
$       DT    BINARY
   0.00001         1
$
*DATABASE_RCFORC
$---+----1----+----2
$       DT    BINARY
  0.000001         1
$
```

```
*DATABASE_NODFOR
$---+----1----+----2
$       DT    BINARY
  0.000001         1
$
*DEFINE_COORDINATE_NODES
$---+----1----+----2----+----3----+----4----+----5----+----6
$      CID        N1        N2        N3      FLAG       DIR
         1    420192    422921    445926                   Z
$
*DATABASE_NODAL_FORCE_GROUP
$ Master Ring Contact
$---+----1----+----2
$     NSID       CID
         7         1
$
*DATABASE_NODAL_FORCE_GROUP
$ Slave Ring Contact
$---+----1----+----2
$     NSID       CID
         8         1
$
$
$---+----1----+----2----+----3----+----4----+----5----+----6----+----7----+----8
$                                                                              $
$                                  PART CARDS                                  $
$                                                                              $
$---+----1----+----2----+----3----+----4----+----5----+----6----+----7----+----8
*INCLUDE
Assembly_1.mesh
$
*INCLUDE
Assembly_1.part
$
*INCLUDE
Assembly_2.part
$
*INCLUDE
matdef.k
$
$
$
$---+----1----+----2----+----3----+----4----+----5----+----6----+----7----+----8
$                                                                              $
$                           PART and NODE SET ID Info                          $
$                                                                              $
$---+----1----+----2----+----3----+----4----+----5----+----6----+----7----+----8
$  PART ID        DESCRIPTION
$         1         Master Impact Ring
$         2         Master Crank
$         4         Slave Impact Ring
$         5         Slave Crank
$
$
$ NODE SET ID     DESCRIPTION
$         1         Master Impact Ring Axial BC Nodes on Face in Contact w Crank
$         2         Master Crank Inner Cylindrical Face
$         3         All Master Crank and Impact Ring Nodes
$         4         Slave Impact Ring Axial BC Nodes on Face in Contact w Crank
$         5         Slave Crank Inner Cylindrical Face
$         6         All Master Impact Ring Nodes
$        7         Surface contact force tracking nodes - Master
$        8         Surface contact force tracking nodes - Slave
$
$
$---+----1----+----2----+----3----+----4----+----5----+----6----+----7----+----8
$                                                                              $
$                               BOUNDARY SPC CARDS                             $
$                                                                              $
$---+----1----+----2----+----3----+----4----+----5----+----6----+----7----+----8
*BOUNDARY_SPC_SET
$ Axial/ Rotational Constraint - Master Impact Ring
$---+----1----+----2----+----3----+----4----+----5----+----6----+----7----+----8
$     NSID       CID      DOFX      DOFY      DOFZ     DOFRX     DOFRY     DOFRZ
         1         0         0         1         0         1         0         1
$
$
```

```
*BOUNDARY_SPC_SET
$ Axial/ Rotational Constraint - Master Crank
$---+----1----+----2----+----3----+----4----+----5----+----6----+----7----+----8
$     NSID       CID      DOFX      DOFY      DOFZ     DOFRX     DOFRY     DOFRZ
         2         0         0         1         0         1         0         1
$
$
*BOUNDARY_SPC_SET
$ Axial Constraint - Slave Impact Ring
$---+----1----+----2----+----3----+----4----+----5----+----6----+----7----+----8
$     NSID       CID      DOFX      DOFY      DOFZ     DOFRX     DOFRY     DOFRZ
         4         0         0         1         0         1         0         1
$
$
*BOUNDARY_SPC_SET
$ Axial Constraint - Slave Crank
$---+----1----+----2----+----3----+----4----+----5----+----6----+----7----+----8
$     NSID       CID      DOFX      DOFY      DOFZ     DOFRX     DOFRY     DOFRZ
         5         0         0         1         0         1         0         1
$
$
$
$---+----1----+----2----+----3----+----4----+----5----+----6----+----7----+----8
$                                                                              $
$                                 CONTACT CARDS                                $
$                                                                              $
$---+----1----+----2----+----3----+----4----+----5----+----6----+----7----+----8
$
*CONTACT_AUTOMATIC_SURFACE_TO_SURFACE_ID
$---+----1----+----2----+----3----+----4----+----5----+----6----+----7----+----8
$      CID-----------------------------HEADING-----------------------------------
         1 Ring_Ring Contact
$
$---+----1----+----2----+----3----+----4----+----5----+----6----+----7----+----8
$     SSID      MSID     SSTYP     MSTYP    SBOXID    MBOXID       SPR       MPR
         4         1         3         3
$
$
$---+----1----+----2----+----3----+----4----+----5----+----6----+----7----+----8
$       FS        FD        DC        VC       VDC    PENCHK        BT        DT

$
$
$---+----1----+----2----+----3----+----4----+----5----+----6----+----7----+----8
$      SFS       SFM       SST       MST      SFST      SFMT       FSF       VSF

$
*CONTACT_AUTOMATIC_SURFACE_TO_SURFACE_ID
$---+----1----+----2----+----3----+----4----+----5----+----6----+----7----+----8
$      CID-----------------------------HEADING-----------------------------------
         2 M Crank_Ring
$
$---+----1----+----2----+----3----+----4----+----5----+----6----+----7----+----8
$     SSID      MSID     SSTYP     MSTYP    SBOXID    MBOXID       SPR       MPR
         2         1         3         3
$
$
$---+----1----+----2----+----3----+----4----+----5----+----6----+----7----+----8
$       FS        FD        DC        VC       VDC    PENCHK        BT        DT

$
$
$---+----1----+----2----+----3----+----4----+----5----+----6----+----7----+----8
$      SFS       SFM       SST       MST      SFST      SFMT       FSF       VSF

$
*CONTACT_AUTOMATIC_SURFACE_TO_SURFACE_ID
$---+----1----+----2----+----3----+----4----+----5----+----6----+----7----+----8
$      CID-----------------------------HEADING-----------------------------------
         3 S Crank_Ring
$
$---+----1----+----2----+----3----+----4----+----5----+----6----+----7----+----8
$     SSID      MSID     SSTYP     MSTYP    SBOXID    MBOXID       SPR       MPR
         5         4         3         3
$
$
$---+----1----+----2----+----3----+----4----+----5----+----6----+----7----+----8
$       FS        FD        DC        VC       VDC    PENCHK        BT        DT

$
$
```

```
$---+----1----+----2----+----3----+----4----+----5----+----6----+----7----+----8
$      SFS        SFM        SST        MST       SFST       SFMT        FSF        VSF

$
$
$---+----1----+----2----+----3----+----4----+----5----+----6----+----7----+----8
$                                                                               $
$                              MOTION/DYNAMICS CARDS                            $
$                                                                               $
$---+----1----+----2----+----3----+----4----+----5----+----6----+----7----+----8
$
*BOUNDARY_PRESCRIBED_MOTION_SET_ROT
$ Initial Rotational Velocity
$---+----1----+----2----+----3----+----4----+----5----+----6----+----7----+----8
$     NSID       DOF       VAD      LCID        SF       VID     DEATH     BIRTH
         3       -10         0         1    -250.0             4.0E-05       0.0
$
$---+----1----+----2----+----3----+----4----+----5----+----6----+----7----+----8
$  OFFSET1   OFFSET2       MRB     NODE1     NODE2
       0.0        0.0
$
$
$---+----1----+----2----+----3----+----4----+----5----+----6----+----7----+----8
$                                                                               $
$                                 LOAD CURVE CARDS                              $
$                                                                               $
$---+----1----+----2----+----3----+----4----+----5----+----6----+----7----+----8
$
*DEFINE_CURVE
$---+----1----+----2----+----3----+----4----+----5----+----6----+----7
$     LCID      SIDR       SFA        SFO      OFFA       OFFO    DATTYP
         1         0      +1.0       +1.0       0.0        0.0         0
$---+----1----+----2----+----3----+----4
$            XVALUES            YVALUES
          +0.000E+00          +1.000E+00
          +1.000E-03          +1.000E+00
          +1.000E-00          +1.000E+00
*END
$
$

$$$$$$$$$$$$$$$$$$$$$$$$$$$$$$$$$$$$$$$$$$$$$$$$$$$$$$$$$$$$$$$$$$$$$$$$$$$$$$$
$                                                                               $
$ LS-DYNA Deck produced by Notarius - Contents copyrighted 2008-2010            $
$        Version:  2                                                            $
$          Build:  1                                                            $
$        Release:  2                                                            $
$   Manufacturer:  Doman Design & Engineering  | Halifax  | Nova Scotia         $
$     Print Date:  June 13, 2008 [10:25 AM]                                     $
$                                                                               $
$$$$$$$$$$$$$$$$$$$$$$$$$$$$$$$$$$$$$$$$$$$$$$$$$$$$$$$$$$$$$$$$$$$$$$$$$$$$$$$
$
$
*KEYWORD
$
*MAT_SIMPLIFIED_JOHNSON_COOK
$ Master Impact Ring - 4340 Steel
$---+----1----+----2----+----3----+----4----+----5
$      MID        RO         E        PR        VP
         1  7830e+00    200e09     0.290
$
$
$---+----1----+----2----+----3----+----4----+----5----+----6----+----7----+----8
$        A         B         N         C    PSFAIL    SIGMAX    SIGSAT      EPSO
    792e06    510e06      0.26     0.014
$
$
*MAT_ELASTIC_TITLE
$---+----1
$  HEADING
Mas Crank Aluminum
$---+----1----+----2----+----3----+----4----+----5----+----6----+----7
$      MID        RO         E        PR        DA        DB         K
         2  2680e+00     71e09     0.334
$
$
$
```

```
*MAT_SIMPLIFIED_JOHNSON_COOK
$ Slave Impact Ring - 4340 Steel
$---+----1----+----2----+----3----+----4----+----5
$       MID         RO          E         PR         VP
          3  7830e+00    200e09     0.290
$
$
$---+----1----+----2----+----3----+----4----+----5----+----6----+----7----+----8
$         A          B          N          C     PSFAIL     SIGMAX     SIGSAT       EPSO
    792e06     510e06       0.26     0.014
$
$
*MAT_ELASTIC_TITLE
$---+----1
$  HEADING
Slave Crank Aluminum
$---+----1----+----2----+----3----+----4----+----5----+----6----+----7
$       MID         RO          E         PR         DA         DB          K
          4  2680e+00     71e09     0.334
$
$
$
$
*END

$$ HM_OUTPUT_DECK created 10:43:30 06-25-2009 by HyperMesh Version 10.0build6
$$ Ls-dyna Input Deck Generated by HyperMesh Version  : 10.0build60
$$ Generated using HyperMesh-Ls-dyna 971 Template Version : 10.0build60
*KEYWORD
$
$---+----1----+----2----+----3----+----4----+----5----+----6----+----7----+----8
$                                                                             $
$                                 PART KEYWORDS                               $
$                                                                             $
$---+----1----+----2----+----3----+----4----+----5----+----6----+----7----+----8
$
*PART
$---+----1
$  HEADING
IMPACT RING, REG, ML1
$---+----1----+----2----+----3----+----4----+----5----+----6----+----7----+----8
$       PID      SECID        MID      EOSID       HGID       GRAV     ADPOPT       TMID
          1          1          1
$
$
*PART
$---+----1
$  HEADING
CRANK, REG, ML1
$---+----1----+----2----+----3----+----4----+----5----+----6----+----7----+----8
$       PID      SECID        MID      EOSID       HGID       GRAV     ADPOPT       TMID
          2          2          2
$
$
$
$
$---+----1----+----2----+----3----+----4----+----5----+----6----+----7----+----8
$                                                                             $
$                               SECTION KEYWORDS                              $$
$                                                                             $
$---+----1----+----2----+----3----+----4----+----5----+----6----+----7----+----8
$
*SECTION_SOLID_TITLE
$---+----1
$  HEADING
M_Ring, SOLID, FULL
$---+----1----+----2
$     SECID     ELFORM
          1          3
$
$
*SECTION_SOLID_TITLE
$---+----1
$  HEADING
M_Crank, SOLID, FULL
$---+----1----+----2
$     SECID     ELFORM
          2          1
$
$
*END
```

```
$$ HM_OUTPUT_DECK created 10:43:30 06-25-2009 by HyperMesh Version 10.0build6
$$ Ls-dyna Input Deck Generated by HyperMesh Version  : 10.0build60
$$ Generated using HyperMesh-Ls-dyna 971 Template Version : 10.0build60
*KEYWORD
$
$---+----1----+----2----+----3----+----4----+----5----+----6----+----7----+----8
$                                                                               $
$                                PART KEYWORDS                                  $
$                                                                               $
$---+----1----+----2----+----3----+----4----+----5----+----6----+----7----+----8
$
*PART
$---+----1
$  HEADING
SlaveIMPACT RING, REG, ML1
$---+----1----+----2----+----3----+----4----+----5----+----6----+----7----+----8
$       PID     SECID       MID     EOSID      HGID       GRAV    ADPOPT       TMID
          4         3         3
$
$
$
*PART
$---+----1
$  HEADING
SlaveCrank, REG, ML1
$---+----1----+----2----+----3----+----4----+----5----+----6----+----7----+----8
$       PID     SECID       MID     EOSID      HGID       GRAV    ADPOPT       TMID
          5         4         4
$
$
$---+----1----+----2----+----3----+----4----+----5----+----6----+----7----+----8
$                                                                               $
$                              SECTION KEYWORDS                                 $
$                                                                               $
$---+----1----+----2----+----3----+----4----+----5----+----6----+----7----+----8
$
*SECTION_SOLID_TITLE
$---+----1
$  HEADING
S_Ring, SOLID, FULL
$---+----1----+----2
$    SECID    ELFORM
          3         3
$
$
*SECTION_SOLID_TITLE
$---+----1
$  HEADING
S_Crank, SOLID, FULL
$---+----1----+----2
$    SECID    ELFORM
          4         1
$
*END
```